

HIGH ENERGY PHOTOPRODUCTION
OF NEUTRAL MESONS

Thesis by
David Louis Kreinick

In Partial Fulfillment of the Requirements
For the Degree of
Doctor of Philosophy

California Institute of Technology
Pasadena, California
1970
(Submitted September 22, 1969)

ACKNOWLEDGMENTS

This experiment was performed by a large collaboration: R. Anderson, D. Gustavson, J. Johnson, D. Ritson and B. Wiik of SLAC, F. Murphy of the University of California at Santa Barbara, R. Weinstein from Northeastern University, and W. G. Jones and I from Caltech. R. Prepost and M. Gettner participated in the early stages of the experiment. I would particularly like to thank Drs. W. Gareth Jones, Robert Anderson, Roy Weinstein, and David Ritson, all of whom found themselves adopted as foster advisors at various times during the data taking period. My advisor, Dr. Charles Peck is always willing to give patient and systematic explanations, and was very helpful during the data analysis phase of the experiment. Working closely with Dr. David Gustavson on the computer was both enjoyable and instructive. Mr. James Johnson and Drs. W. Gareth Jones, Bjorn Wiik, and David Ritson were important contributors to the data analysis.

A large crew contributed to this experiment. SLAC technicians J. Grant, A. Fillipi, D. McShurley, J. Escalera, and J. Schroeder helped design, build and set up equipment. W. Friedler of Caltech helped design and build the Cerenkov counter. Special crews for running the accelerator and preparing the experimental floor were indispensable. A. Golde and his crew were especially helpful and efficient. Dr. G. Fischer loaned us the Cerenkov beam monitor and the calorimeter as well as the technicians to set them up, and helped with the photon beam.

I would like to thank SLAC for making office space and equipment available. The A. E. C. funded the experiment. Finally, thanks are due the N. S. F. and Caltech for financial support.

ABSTRACT

Cross sections for the photoproduction of neutral pi, eta, rho and phi mesons on hydrogen have been measured at the Stanford Linear Accelerator Center using a missing mass spectrometer technique. The data cover photon energies between 5.0 and 17.8 GeV and four momentum transfer squared t between $-.12$ and -1.38 $(\text{GeV}/c)^2$.

Pion differential cross sections at lower energies show a peak at low momentum transfers, a distinctive dip and secondary maximum for t in the region $-.4$ to $-.9$ $(\text{GeV}/c)^2$, and a smooth decrease at higher momentum transfers. As photon energy increases, the dip becomes less pronounced, in contradiction to the expectations of simple Regge theories based on the exchange of omega and B trajectories only.

Eta photoproduction was measured only below 10 GeV. The cross section has about the same magnitude as the pion production cross section, but decreases exponentially with t , showing no dip.

Rho mesons appear to be diffractively produced. The differential cross section varies approximately as $\exp(8.5t + 2t^2)$. It falls slowly with energy, decreasing about 35 percent from 6 GeV to 17.8 GeV. A simple quark model relation appears to describe the data well.

Phi meson cross sections are also consistent with diffraction production. The differential cross section varies approximately as $\exp(4t)$. The cross section tends to decrease slightly with photon energy.

Production of particles with masses between 1100 and 2000 MeV was sought. A broad resonance with mass 1240 ± 20 MeV was observed. It is tentatively identified with the B meson. No particle of mass between 1300 and 2000 MeV and width less than 200 MeV was produced with a cross section larger than about 10 percent of the rho's.

v

to my parents

TABLE OF CONTENTS

<u>PART</u>	<u>TITLE</u>	<u>PAGE</u>
I	INTRODUCTION	1
	A. Objectives	1
	B. Scope and Organization of this Thesis	4
II	METHOD AND APPARATUS	6
III	YIELD CURVES	12
	A. Kinematics	12
	B. Yield Curves	15
	C. Background	18
	D. Sample Data	30
IV	DATA ANALYSIS	58
	A. Data Consolidation	58
	B. Fitting Procedure	59
	C. Calculation of Cross Sections	62
V	RESULTS AND DISCUSSION	66
	A. Pion	66
	B. Eta	74
	C. Rho	77
	D. Phi	90
	E. X^0 (958)	97
	F. "B"	97
	G. Mass Search	100
	APPENDICES	106
	REFERENCES	163

APPENDICES

<u>PART</u>	<u>TITLE</u>	<u>PAGE</u>
A	1. The SLAC Accelerator	106
	2. The Photon Beam	108
	3. Beam Monitors	112
	4. Hydrogen Target	114
	5. The Spectrometer	116
	6. Counters	119
	7. Electronics	124
	8. The Computer	128
	9. Resolution	130
B	1. Data Consolidation	133
	2. Fitting Procedure	141
	a) Background	142
	b) Eta and Phi	142
	c) Pion	146
	d) Rho	151
	3. Corrections	158

FIGURES

<u>NUMBER</u>	<u>CAPTION</u>	<u>PAGE</u>
1	The 1.6 GeV/c Spectrometer	9
2	θ vs. p for Various Masses	11
3	Yield Curve	17
4	Two Yield Curves	19
5	Subtracted Yield Curve	20
6	Comparison of Yield Curve, Subtracted Curve and First Difference Curve	21
7	Ghost Proton Yield vs. Photon Energy for Various t	23
8	Ghost Proton Yield vs. t for Various Photon Energies	25
9	Sample Yield Curves	31
10	Pion Cross Section vs. $s-M^2$	67
11	Pion Production Effective Regge Trajectory	69
12	Pion Cross Section vs. t	70
13	Pion Cross Section vs. t	71
14	Eta Cross Section vs. t	75
15	Eta Cross Section vs. t	76
16	Rho Cross Section vs. t	81
17	Rho Cross Section vs. t	83
18	Rho Cross Section vs. s	84
19	Rho Production Effective Regge Trajectory	85
20	Feynman Graph for Rho Photoproduction	88
21	Phi Cross Section vs. t	92
22	Phi Cross Section vs. s	94
23	Phi Production Effective Regge Trajectory	95

<u>NUMBER</u>	<u>CAPTION</u>	<u>PAGE</u>
24	Subtracted Yield Curve Showing "B" Production	98
25	Mass Search Yield, $t = -.2 \text{ (GeV/c)}^2$	101
26	Mass Search Yield, $t = -.3 \text{ (GeV/c)}^2$	102
A-1	Photon Beam	109
A-2	Reduced Bremsstrahlung Spectrum	111
A-3	Hydrogen Target	115
A-4	1.6 GeV/c Spectrometer	117
A-5	Counter Telescope	120
A-6	Proton and Pion Trigger Logic	125
A-7	Hodoscope Trigger Logic	126
B-1	Data Matrix	135
B-2	Eta Step	144
B-3	Phi Step	145
B-4	Pion Step Showing Energy Resolution Problem	149
B-5	Feynman Graphs	153

TABLES

<u>NUMBER</u>	<u>TITLE</u>	<u>PAGE</u>
1	Parameters for Computing Cross Sections	64
2	Corrections to the Cross Section	65
3	Rho Production Differential Cross Section	78
4	Rho Production Forward and Total Cross Sections	86
5	Phi Production Differential Cross Section	91
6	"B" Production Differential Cross Section	99
7	Mass Search Upper Limits	104
A-1	Cerenkov Counter Efficiency for Protons	122
A-2	Contributions to Mass Uncertainty	131
B-1	Hodoscope Efficiency at $t = -.7 \text{ (GeV/c)}^2$	136
B-2	Hodoscope Efficiency vs. t	138

I. INTRODUCTION

A. Objectives

This experiment has extended data on neutral meson photoproduction to 17.8 GeV incident energy and a broad range of four-momentum transfers. It was made possible by the new high-energy, high-current electron accelerator at the Stanford Linear Accelerator Center (SLAC). Use of the SLAC 1.6 GeV/c spectrometer with a missing mass spectrometer technique permitted taking data on production of many different mesons with high statistical precision.

When this experiment began, photoproduction data existed for photon energies up to 6 GeV. The data and theoretical predictions for each particle we studied will be briefly described now. (For completeness experiments done since this experiment was begun will be mentioned parenthetically.)

Forward neutral pion photoproduction has been studied between photon energies of 2 and 5.8 GeV by groups at the Deutsches Elektronen-Synchrotron (DESY)⁽¹⁾ and at the Cambridge Electron Accelerator (CEA)⁽²⁾. The differential cross sections they obtain show a "dip" at a four-momentum transfer squared t of about $-.5(\text{GeV}/c)^2$, which appears to become more pronounced as photon energy increases. A reasonable explanation of this effect resulted from assuming that omega Regge trajectory exchange dominates the amplitude^(3, 4). At $t = -.5 (\text{GeV}/c)^2$ the contribution of this trajectory vanishes, leaving the dip. The cross section does not fall to zero completely because resonances⁽³⁾ or B exchange⁽⁴⁾ still contribute. However, these mechanisms become relatively less important at higher energies, and therefore the dip should deepen with increasing

photon energy. The theory also predicts the usual Regge shrinkage of the forward peak at high energies. Neither of these predictions is borne out by our data.

Very few data on eta photoproduction at high energies were available at the start of this experiment. Bubble chamber experiments at DESY⁽⁵⁾ and CEA⁽⁶⁾ which observed only a few events were the only source of data above 2 GeV. (At the same time this experiment was run data at 4 GeV incident energy were being taken by Bellenger et al.⁽⁷⁾ at CEA.) Predictions were, however, made by Dar and Weisskopf⁽⁸⁾ using vector dominance and SU₃ symmetry to relate eta photoproduction to the process $\pi^- + p \rightarrow \omega + n$. This theory predicted a smooth dependence of the cross section on t . On the other hand, one might expect simple Regge trajectory exchange theory⁽⁹⁾ to predict a dip analogous to the pion dip at $t = -.5 (\text{GeV}/c)^2$, where the contribution of the rho trajectory vanishes. Our data agree qualitatively with the Dar and Weisskopf model, and show no dip.

Data on rho meson production at energies up to 6 GeV were rather plentiful^(5, 6, 10, 11). (Several experiments were measuring rho production at higher energies while this experiment was being run^(12, 13, 14).) The differential cross section falls rapidly with momentum transfer, approximately as $\exp(8t)$. The cross sections appear roughly independent of photon energy. This behavior was understood using the vector meson dominance model.⁽¹⁵⁾ According to this model, the cross sections for photoproduction of vector mesons are proportional to the elastic scattering cross sections for transversely polarized vector mesons on protons. A simple quark model⁽¹⁶⁾ can be used to obtain the cross section for vector meson-proton elastic scattering in terms of measurable meson-proton cross

sections. The theory predicts approximate constancy of the cross section with photon energy. The predictions are consistent with our data.

Omega and phi cross section measurements were somewhat less plentiful^(5, 6, 10). (There are several recent higher energy experiments^(12, 5, 17).) These data, while statistically poorer than the rho data, seemed to show similar characteristics of diffraction production. The vector dominance model and quark model were also applicable here, and fit the data reasonably well. The SU_3 prediction of a ratio of 9:1:2 for rho:omega:phi photoproduction appeared to work well for the rho:omega ratio, but predicted a factor 20 too much phi production.⁽¹⁸⁾ Several SU_3 breaking theories were advanced which modify this ratio^(18, 19). The energy and t dependence of our phi production data are in qualitative agreement with these models, although the production rate still appears lower than anticipated.

A search for other particles was desirable for several reasons. Many resonances excited in pion-proton interactions had not been conclusively observed in photoproduction, e.g., B , f^0 , A_1 and A_2 .⁽¹¹⁾ It is also possible that a resonance only weakly coupled to the pion-nucleon system could be visible in photoproduction. Finally, a particle on the first "daughter" trajectory to the rho meson trajectory should have been visible in photoproduction. The missing mass spectrometer technique is ideal for seeking these kinds of particles, since great amounts of data can be taken quickly and since the details of the particles' decay process are immaterial. We have tentatively identified a broad peak at 1240 MeV with the B meson. No mesons with mass between 1300 and 2000 MeV, width less than

200 MeV, and production cross sections more than 15 percent of the rho's were seen.

B. Scope and Organization of this Thesis

The data on pion and eta production are not as yet complete. Two experiments at SLAC, one already run⁽²⁰⁾ and one shortly to be run⁽²¹⁾ should help complete the picture. The pion and eta data of this experiment and the one yet to be done⁽²¹⁾ (if successful) will constitute the Ph.D. thesis of Mr. J. Johnson of Stanford University. Nevertheless, the partial pion and eta data are reported in this thesis for logical consistency and completeness.

The prime focus of this thesis is on the remainder of the data. Differential cross sections for the production of rho and phi mesons are obtained and their energy and momentum transfer dependence investigated. Little can be said about their widths and shapes, and nothing about their decays. Cross sections for the particle tentatively identified as a B meson are given where possible. An upper limit is given for the photoproduction of particles with masses up to 2 GeV.

In chapter II, the experimental technique and apparatus are sketched. Only a general description of the apparatus is attempted; details of design and performance are presented in appendix A.

Chapter III describes the yield curves which constitute the data of this experiment. Section A is devoted to kinematics; section B describes the yields expected from each particle; backgrounds are discussed in section C; section D presents a representative sample of the data.

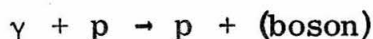
In chapter IV the process of obtaining cross sections from the data is summarized. Section A describes how the data from many short runs were assembled into yield curves. In section B the program for fitting the yield curves is described. Section C presents a summary of factors and corrections used in obtaining cross sections. Each of these sections is a summary of a corresponding section of appendix B, in which the procedures are described in detail.

In chapter V the cross sections obtained for each particle are presented, compared to the results of other experiments, and discussed in the light of theoretical predictions.

Appendices A and B elaborate on the apparatus and data analysis, respectively, as already mentioned.

II. METHOD AND APPARATUS

In this experiment the reaction



was investigated using a missing mass spectrometer technique. Before the apparatus is described, the basic features of the technique will be sketched.

If in a two-body reaction



one measures the four-momenta p_A , p_B and p_C of the A, B and C particles, he can identify the D particle by its mass

$$m_D^2 = p_D^2 = (p_A + p_B - p_C)^2 \quad (\text{II-1})$$

without ever actually observing D. This technique both avoids the complexities of detecting a rapidly decaying D particle and permits surveying the production of all possible D particles with one experimental arrangement. At an accelerator, the experimenter can usually measure p_A and p_B easily, and the difficulty comes in determining p_C and the flux of A's precisely enough. When analysing the data, one assumes the C particle was formed in a two-body reaction; multi-body final states can produce a range of apparent missing masses, and constitute an unavoidable source of background.

For this experiment A was a bremsstrahlung photon, B a target proton and C the recoil proton. A broad spectrum of photons struck the target. Fortunately a good knowledge of the maximum ("endpoint") photon energy and an approximate knowledge of the energy spectrum provide enough information about the photon momentum. A spectrometer analysed the recoil proton momentum and angle. Missing mass was varied by changing the angle of observation of the spectrometer for a fixed endpoint energy and recoil proton momentum. The proton yield as a function of angle shows unique structure when the threshold for production of a boson is reached, which allows the experimenter to measure cross sections.

The experiment was performed at the SLAC accelerator. Momentum-analysed electrons struck a .03 radiation length aluminum radiator 50 m. upstream of the target and were then swept from the beam. The resulting bremsstrahlung beam, after collimation and more sweeping, traversed the hydrogen target and finally stopped in the secondary emission quantameter (SEQ) about 30 m. beyond the target. The SEQ was the main beam monitor, but two other monitors operated continuously to verify SEQ stability. Absolute normalization and long term stability were measured by periodically calibrating the SEQ against a calorimeter. Short term monitor stability was about .2 percent and long term reproducibility better than 3 percent. The energy spectrum of photons in the beam was estimated theoretically.

The liquid hydrogen target cell was a 12 inch long mylar cylinder with its axis along the beam line. Variable slits in front of the spectrometer limited the viewed length of the target to about 6.5 inches. In particular, the aluminum beam entrance and exit windows were masked out. The target cell was made only 2 inches in diameter to reduce the amount of material protons had to go

through before being detected, since multiple scattering of protons was the chief restriction on mass resolution. An unfilled duplicate of the target cell could be inserted into the beam for empty target runs.

The SLAC 1.6 GeV/c spectrometer measured the angle and momentum of the recoil protons. Figure 1 shows the spectrometer schematically. The entire spectrometer rotates about the hydrogen target under remote control. The magnet bends particles upwards 90 degrees on a 100 inch radius. Second order optics corrections insure that momentum and angle are focused in a single plane, and that this plane is perpendicular to the direction of analysed particles. The usable magnet acceptance $\frac{\Delta p}{p} \Delta \Omega$ is 6.8×10^{-5} sterad. Resolution of the spectrometer, .08 percent in momentum and .4 mrad. in angle, contributes a negligible amount to mass uncertainty.

The counter telescope is at the top of the spectrometer, shielded from room background by a concrete cave. The telescope is depicted in the inset to figure 1. The 7- by 11-inch scintillation counters S9 and S10 sandwich an eight-counter hodoscope S1 - S8, which lies in the focal plane of the magnet. A Lucite threshold Cerenkov counter C and scintillation counters S11, S12 and S13 are further back in the telescope. The entire counter assembly can be rotated remotely about an axis parallel to the path of incoming particles, for reasons discussed below.

The large counters S9, S10, S11 and C are used to identify protons. A background of pions, roughly equal in flux to the protons, is rejected using a combination of energy loss and Cerenkov requirements. Pion contamination is less than 2 percent. Pions are counted employing Cerenkov and range requirements with counters C, S12 and S13.

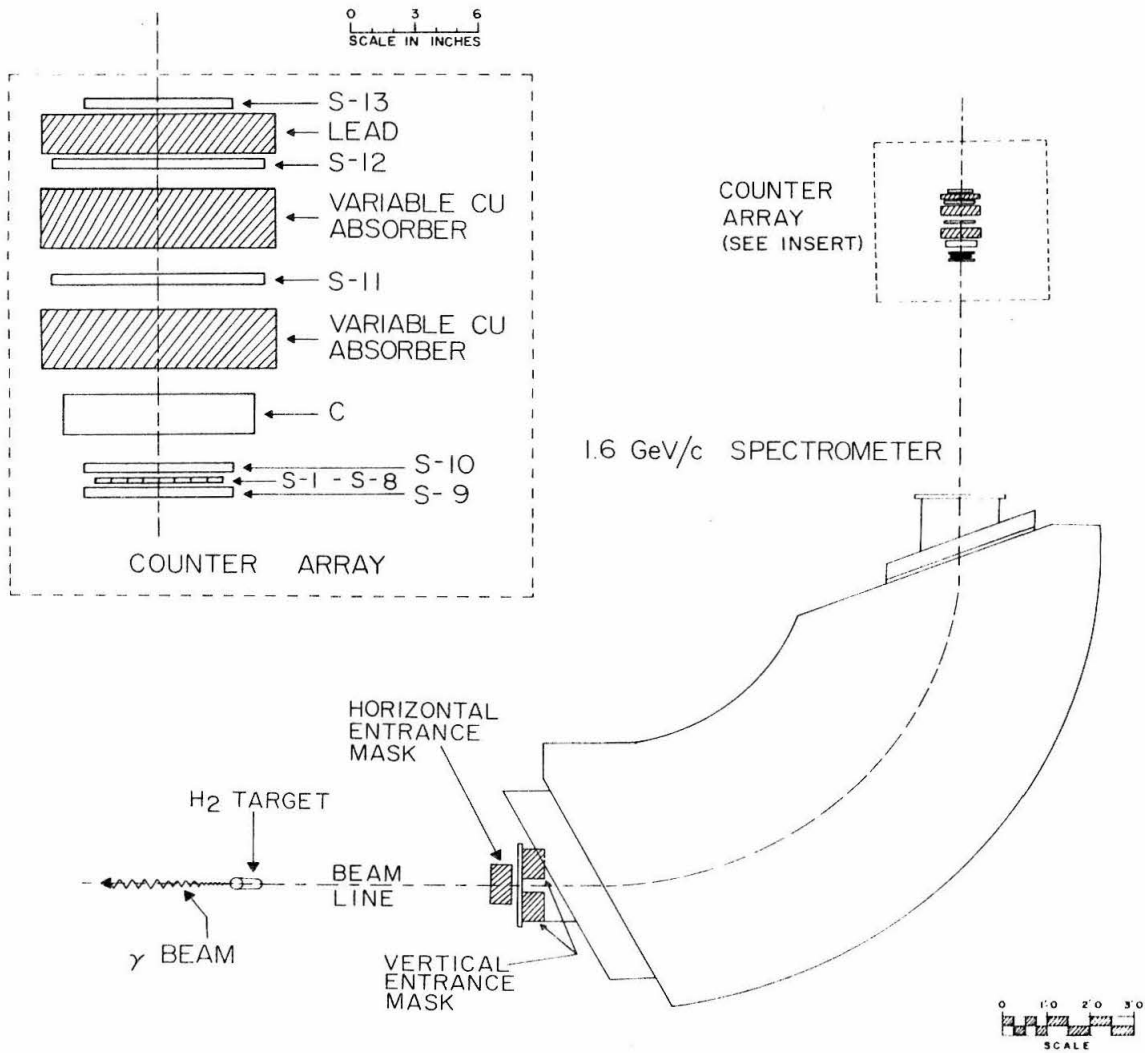


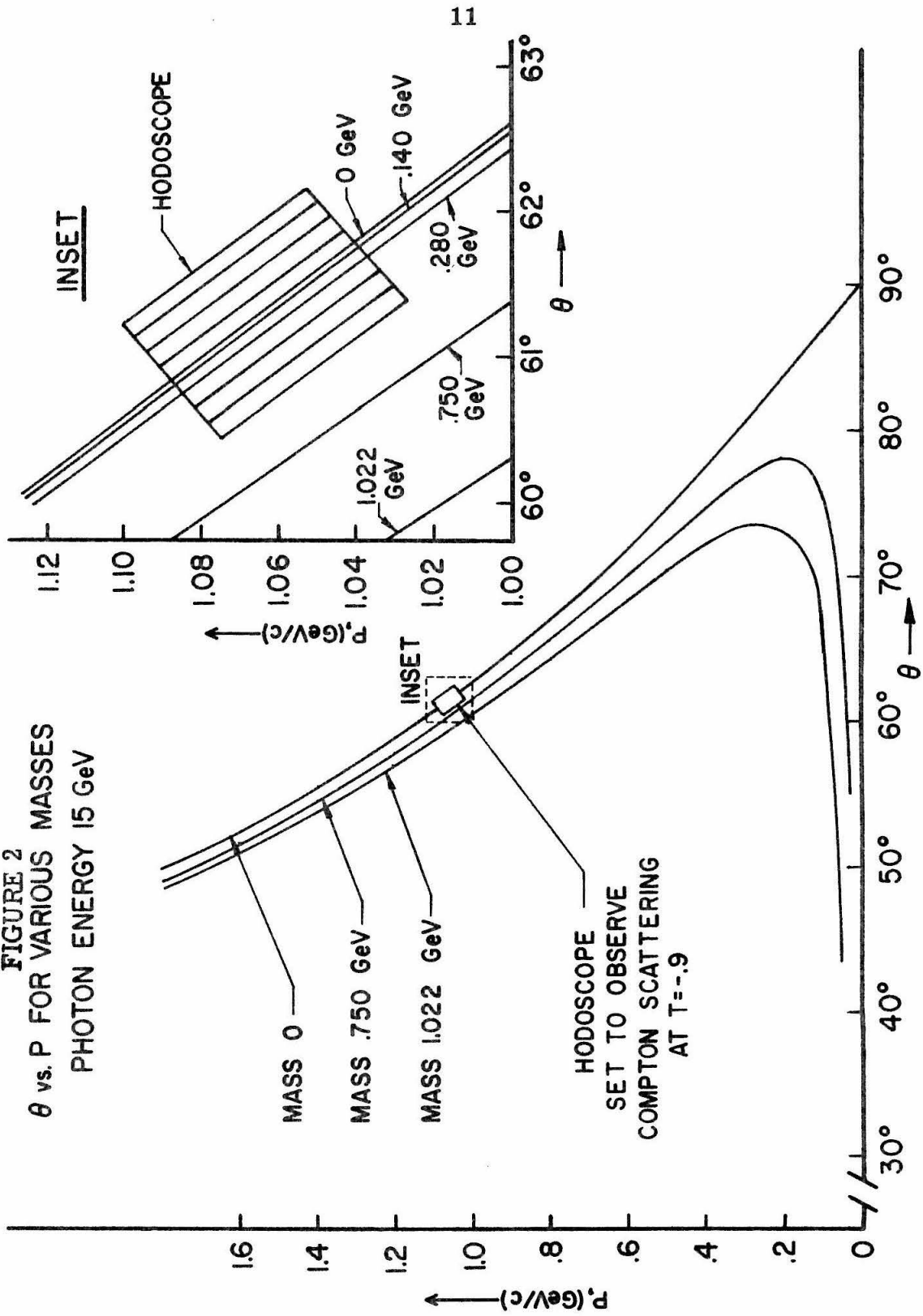
FIGURE 1 The 1.6 GeV/c Spectrometer

Eight scalers count coincidences between the proton logic and hodoscope counter pulses. These counting rates are the basic data of the experiment. Each hodoscope counter defines a small range of missing mass, as can be seen with the aid of figure 2. This graph shows the relation between the momentum and the angle of a recoil proton for a fixed photon energy and chosen missing mass. Over the small acceptance of the hodoscope, this relation is approximately linear. By rotating the telescope to align the hodoscope counters with lines of constant missing mass, the experimenter makes a missing-mass hodoscope. For convenience, the hodoscope is not rotated to the proper angle for each spectrometer angle setting; rather, a compromise hodoscope angle is used for each value of t .

Because data rates were high, typically several events per 1.6-microsecond long beam pulse, it was necessary to keep track of accidental coincidences and dead time. This was accomplished by counting deliberately mistimed coincidences between various key counters. The beam intensity was lowered occasionally to calibrate accidental rate and dead time against these monitors. Corrections for these effects were less than 5 percent. Empty target rates were measured occasionally, always indicating a negligible effect.

SLAC's on-line SDS 9300 computer was used as a secretary. It recorded all useful data, issued warning messages, plotted the incoming data, so that physicists could compute cross sections and check for trouble, and made diagnostic calculations to monitor the performance of the apparatus.

FIGURE 2
 θ vs. P FOR VARIOUS MASSES
PHOTON ENERGY 15 GeV



III. YIELD CURVES

A. Kinematics

A relation between cross sections and experimental proton yields is necessary for understanding the data, and will be presented here.

Applying the missing mass relation (II-1) to meson photo-production, one finds

$$m_x^2 = 2pk \cos \theta - 2T(M + k) = 2pk \cos \theta - |t| \left(1 + \frac{k}{M}\right) \quad (\text{III-1})$$

where

m_x is the meson mass,

p is the magnitude of the recoil proton three-momentum,

k is the photon energy,

θ is the angle between the recoil proton and incident photon,

T is recoil proton kinetic energy,

M is the mass of a proton,

and $t = -2MT$ is the square of the four-momentum transfer to the proton. All variables are evaluated in the laboratory system.

The incident bremsstrahlung beam has a known distribution of photon energies:

$$N(k)dk = N_\gamma \alpha(k, E_0) \frac{dk}{k} \quad (\text{III-2})$$

where

$N_\gamma = W/E_0$ is the number of equivalent quanta,

W is the total energy in the beam,

E_0 is the electron energy, the endpoint energy,

and $\alpha(k, E_0)$ is the reduced bremsstrahlung spectrum factor, approximately 1.0 for k less than E_0 and zero for k greater than E_0 . The function is normalized so that the total beam energy is W . Its precise form is discussed in appendix A.

Using these two equations and assuming the photoproduced meson has negligible width, one calculates the proton yield at angle θ and momentum p :

$$\text{Yield} = \eta N_p N_\gamma \alpha(k, E_0) \frac{dk}{k} \frac{d\sigma}{dt} dt \quad (\text{III-3a})$$

$$= \eta N_p N_\gamma \alpha(k, E_0) \frac{d\sigma}{dt} J \frac{\Delta p}{p} \Delta\Omega \quad (\text{III-3b})$$

where

η is an overall detection efficiency factor,

$N_p = \left(\frac{\rho N_0}{A}\right) \left(\frac{L}{\sin \theta}\right)$ is the number of viewed target protons per unit area,

ρ is the density of liquid hydrogen in the target,

N_0 is Avogadro's number,

A is the atomic weight of hydrogen,

$\frac{L}{\sin \theta}$ is the effective length of the target as viewed through slits of width L ,

$\frac{d\sigma}{dt}$ is the differential cross section,

$$J = \frac{\partial(k, t)}{\partial(p, \Omega)} = \frac{M p^3}{\pi(T + M)(p \cos \theta - T)} = \frac{p E_0 |t| (|t| + 4M^2)}{\pi(|t| + 2M^2)(|t| + m_x^2)}$$

is the Jacobian for transforming from variables k and t to the measured variables p and θ , and is derived from equation (III-1),

$\Delta\Omega$ is the solid angle acceptance of the spectrometer,

$\frac{\Delta p}{p}$ is the fractional momentum acceptance of the spectrometer,

and other variables are as defined above. Equation (III-3b) has three independent variables p , θ and m_x , the mass of the meson whose cross section is being measured. In particular, the photon energy k is determined by these variables.

For particles like the rho, with width greater than experimental resolution, one must explicitly introduce the mass aperture of the apparatus, dm , into equation (III-3) by replacing $\frac{d\sigma}{dt} dt$ with $\frac{d^2\sigma}{dt dm} dt dm$. The mass dependence of the cross section will be assumed separable from the energy and t dependence, i. e.,

$$\frac{d^2\sigma}{dt dm} = \frac{d\sigma}{dt} P(m) .$$

The particle shape function $P(m)$ might be, for example, the familiar Breit-Wigner resonance form. With this generalization equation (III-3) becomes

$$\text{Yield} = \eta N_p N_Y J \left[\int_0^\infty \alpha(k', E_0) \frac{d\sigma}{dt}(k', t) P(m') dm' \right] \frac{\Delta p}{p} \Delta\Omega . \quad (\text{III-3c})$$

α and $\frac{d\sigma}{dt}$ are inside the integral over missing mass because the effective photon energy k' is determined by m' and the measured p and θ . The upper limit to the integral is reached when k' equals E_0 , after which $\alpha(k, E_0)$ is zero.

B. Yield Curves

The expected proton yield will now be described. In the discussion, as in the experiment, the bremsstrahlung endpoint is fixed at E_0 , and the magnet is set to observe protons of momentum p . Proton yield will be described as a function of θ as θ decreases from ninety degrees.

From equation (III-1)

$$m_x^2 = 2k(p \cos \theta - T) - 2MT$$

it is clear that for angles larger than ninety degrees no protons from two-body processes can be observed, since the right side of the equation is negative, implying imaginary missing mass. As θ decreases, the term in parentheses becomes larger and eventually recoil protons from elastic scattering of endpoint energy photons are observable. If θ becomes still smaller recoil protons are still observed from elastic scattering, but are produced by lower energy components of the bremsstrahlung beam.

Thus in a plot of proton yield against angle, Compton scattering gives rise to a step. The leading edge of the step is located at an angle θ which can be calculated from equation (III-1) substituting $m_x = 0$ and $k = E_0$. The shape of the leading edge is determined in this experiment almost entirely by the angular

resolution of the apparatus. The shape of the curve beyond threshold angle depends on the bremsstrahlung spectrum, the energy dependence of the cross section and on kinematic factors, as can be seen from equation (III-3b).

As angle decreases further, steps from production of higher mass particles appear. The proton yield curve thus is a sum of steps from production of various particles and a smooth background (to be discussed in the next section). Figure 3 shows the experimental proton yield obtained at endpoint energy 11.5 GeV and momentum transfer $t = -.7 (\text{GeV}/c)^2$. Angle is plotted increasing to the left on the x axis in units of hodoscope counter widths (about 2.6 milliradian). Proton counts per 10^{11} equivalent quanta are plotted vertically. Smooth curves represent the calculated step shapes for the pi, rho and phi mesons, the background, and the total of these, a fit to the data. There is no step for eta production because its cross section is too small for a signal to be seen. Elastic scattering is not resolved from pion production and its cross section is small, so no step is shown for it either.

At any angle recoil protons from several different processes are being seen simultaneously. For example, in figure 3, at the angle where phis are being produced by 11.5 GeV photons, rhos are produced by 8.3 GeV photons, pions by 4.8 GeV photons, and background by the full photon spectrum. The interesting signal, the phi step, accounts for only about 3 percent of the total proton yield.

The classical "subtraction" technique effectively gives the yield of a nearly monochromatic photon beam and helps verify that production by low energy photons is causing no difficulty in interpretation. The method exploits the weak dependence on E_0 of the reduced bremsstrahlung factor $\alpha(k, E_0)$. Data are taken at two nearby end-

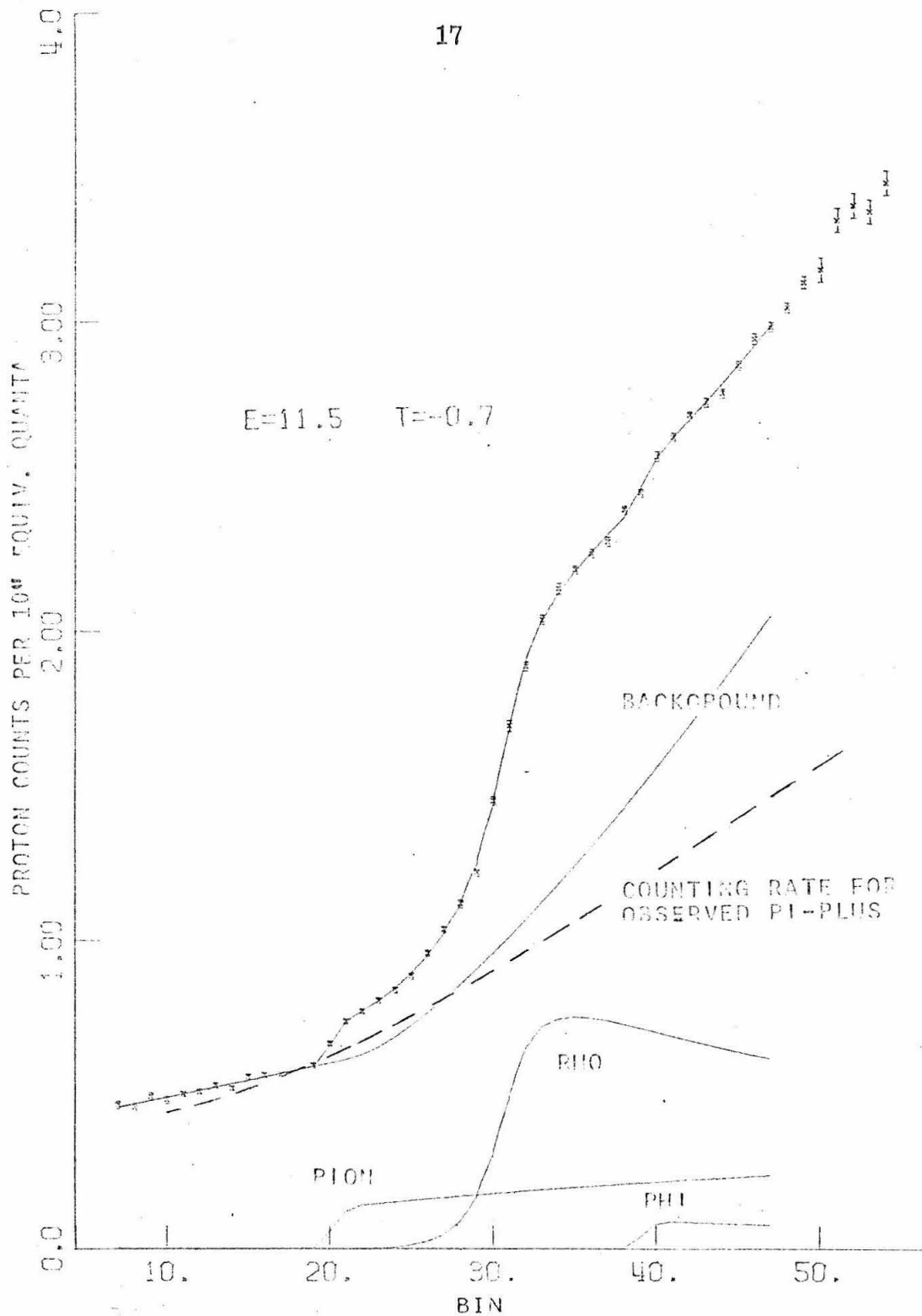


FIGURE 3 Yield Curve

point energies. Subtracting the two sets of data with proper normalization approximately cancels the effect of photons below the lower energy. Figure 4 shows data at two different endpoint energies on the same angle scale. In figure 5 the resulting subtracted yield curve is plotted. The subtraction technique sacrifices statistical precision and also relies more critically on the beam monitor stability than direct analysis of the yield curves. Thus although it was used as a check throughout the experiment, it was only required in rare cases when production of direct channel resonances like the $N^*(1920)$ by low energy photons obscured the step of an interesting particle.

Curves looking very similar to subtractions can be obtained by numerically differentiating the curve obtained at a single endpoint energy. In figure 6c the successive first differences of a yield curve are plotted. The original yield curve is at the top of the figure and a subtracted yield curve is in the middle. The similarity of the bottom two curves demonstrates that the original yield curve contains all information needed to extract cross sections.

C. Background

As is obvious from the yield curves in figures 4 and 5, not all protons observed come from meson production. Background typically accounts for 50 percent of the observed counting rates, and therefore is a serious problem.

It can have two different harmful effects. A smoothly varying background reduces the signal to noise ratio. Since a particle appears as a step on an otherwise smooth curve, additional smooth background will increase the size of statistical errors and make the separation between step and smooth background statistically less significant, but

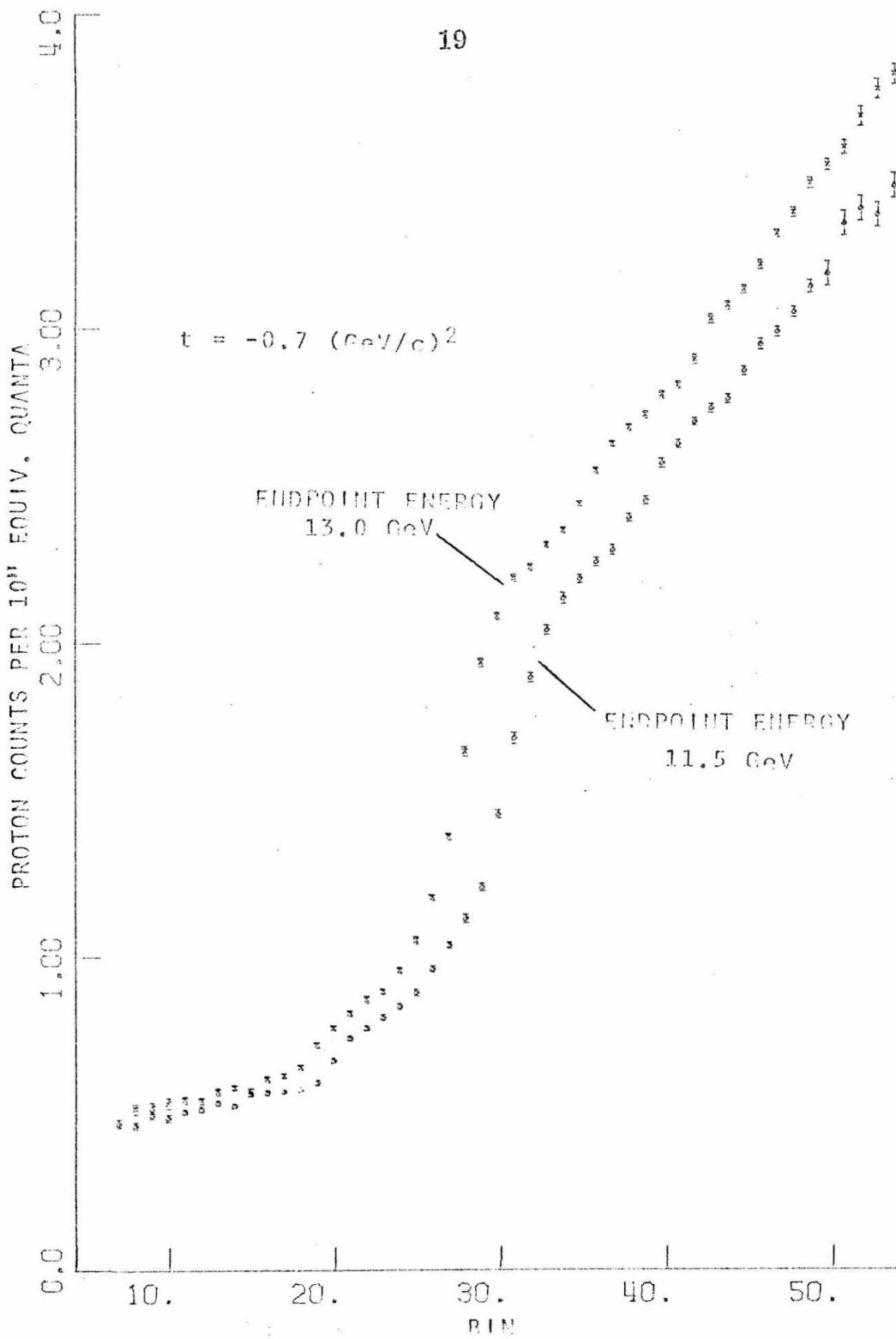
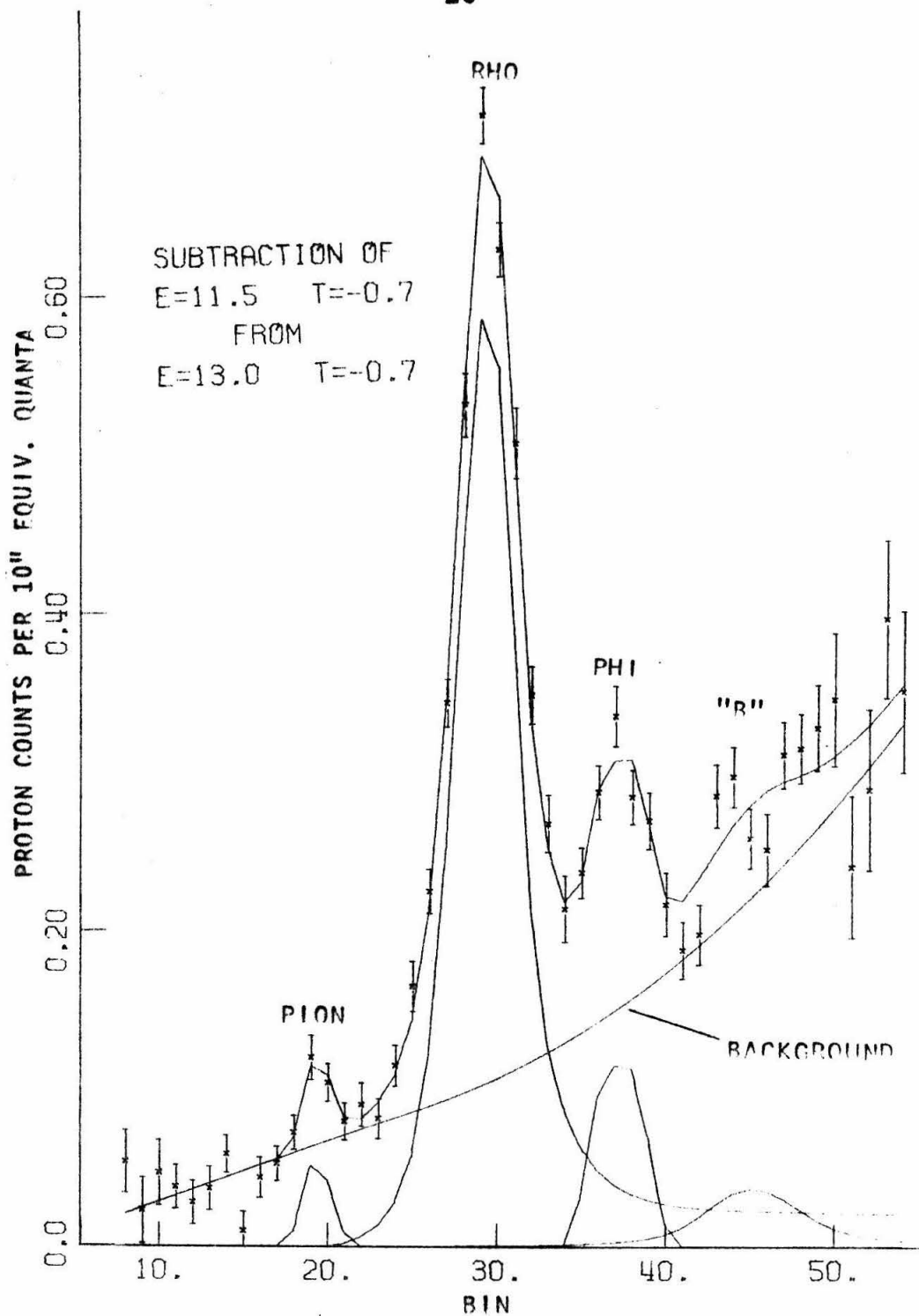


FIGURE 4 Two Yield Curves

**FIGURE 5** Subtracted Yield Curve

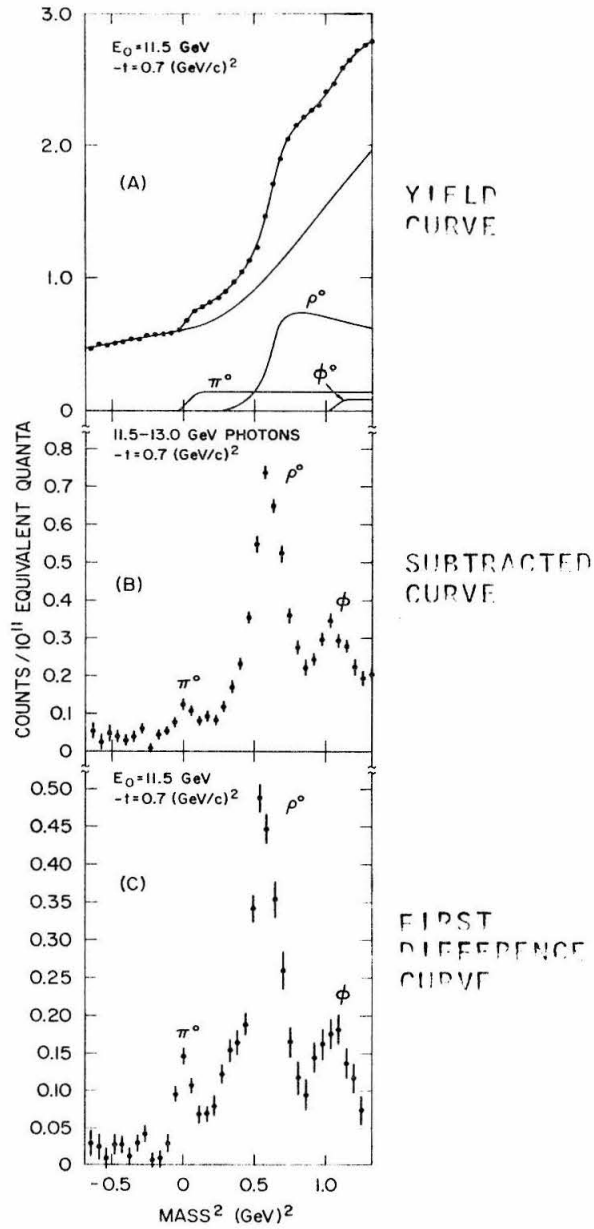


FIGURE 6 Comparison of Yield Curve, Subtracted Curve and First Difference Curve

will not change the apparent size of the step. A background can, on the other hand, create false steps and mask real ones if it varies with angle about as quickly as the steps of the particles expected. The steps from broad resonances like the rho and the B are therefore more susceptible to this kind of interference than the sharp steps of the pion, eta, and phi.

It is kinematically impossible, in single processes, for recoil protons to be produced at angles greater than that corresponding to elastic scattering of endpoint energy photons. Such "ghost protons" are nevertheless common, as can be seen in figure 4. The counting rate of this background is generally one to eight times as large as the rate due to pion production. The problem has been encountered in other photoproduction experiments in which only the recoil proton was observed. (22)

Ghost proton yield appears to have a smooth dependence on endpoint energy and momentum transfer, as shown in figures 7 and 8. In these graphs the plotted yield is the background in the forbidden region extrapolated to zero missing mass. Statistical errors are smaller than the symbol size. Dotted lines are only to guide the eye. Figure 7, showing ghost proton yield vs. photon energy for various t , has been split in two parts because the level of this background changed with experimental arrangement. Figure 7a shows yields obtained when a mask near the target blocked all but the target hydrogen from the view of the spectrometer. The yields of figure 7b, which are approximately 70 percent greater, were obtained without this mask. About half this experiment's data was taken with each arrangement. Filled in symbols in figure 7 identify data taken with other differences in experimental arrangement. In figure 8 ghost proton yield is plotted against t for three different photon energies.

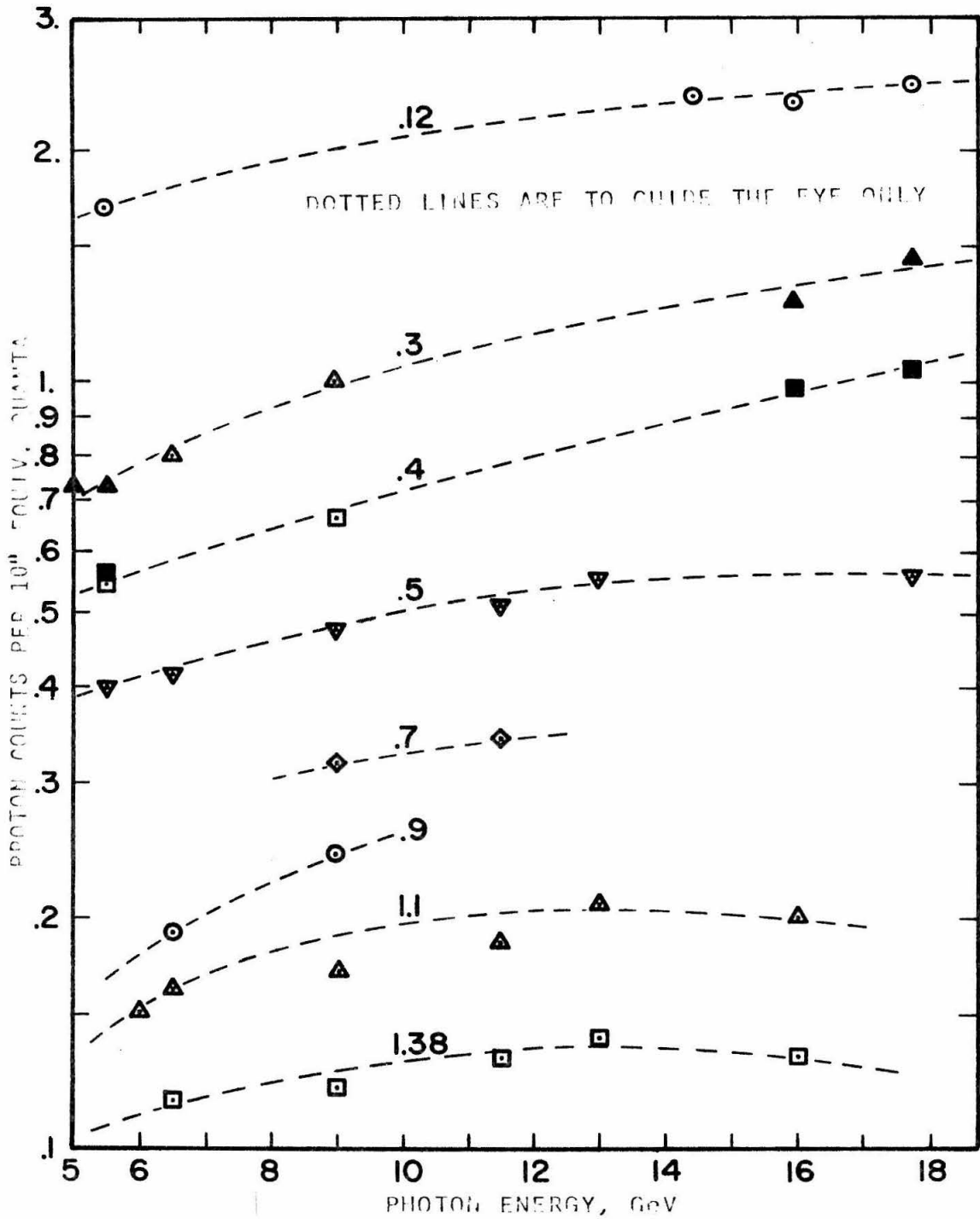


FIGURE 7a Ghost Proton Yield vs. Photon Energy for Various t

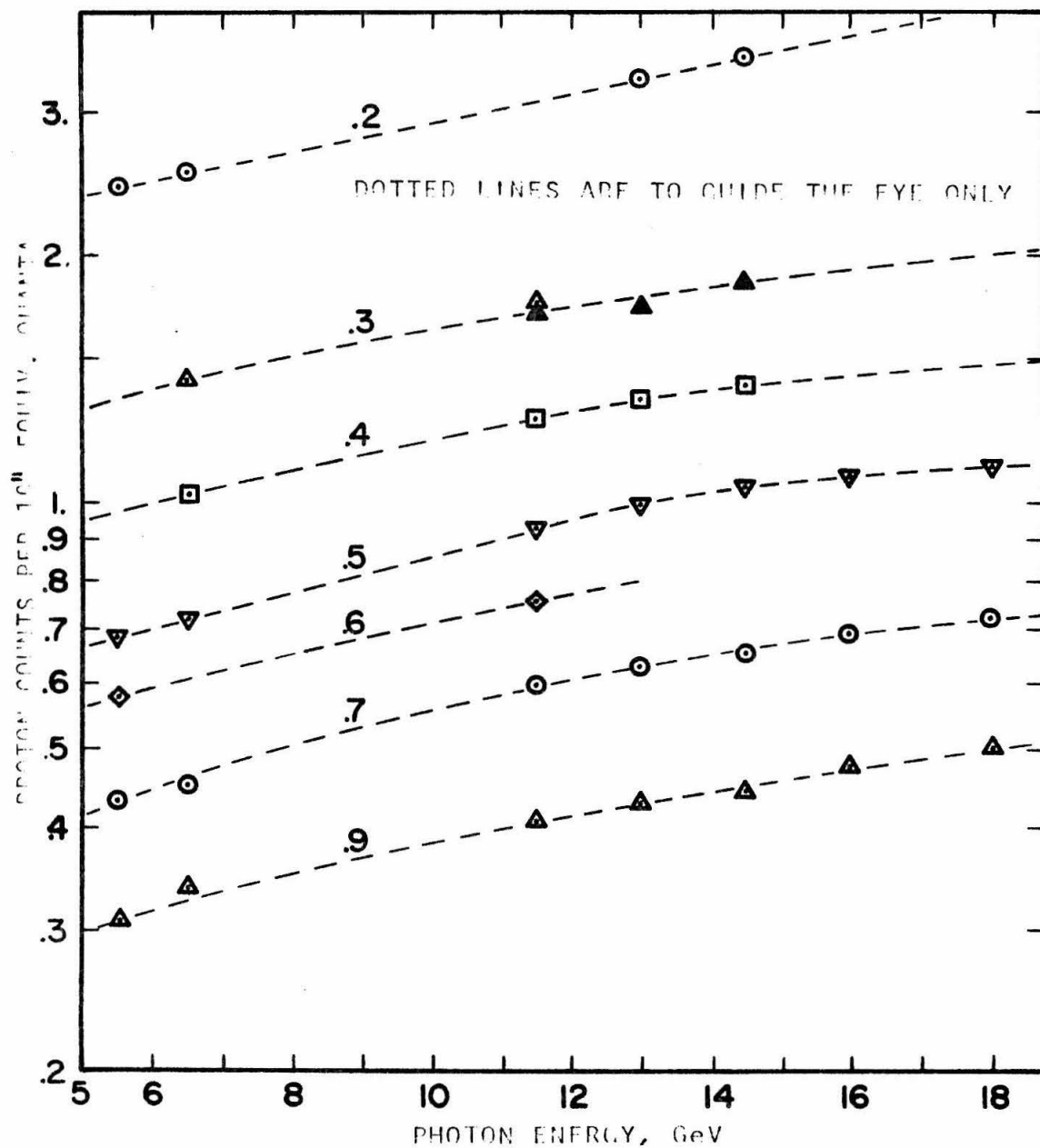


FIGURE 7b Ghost Proton Yield vs. Photon Energy for Various t

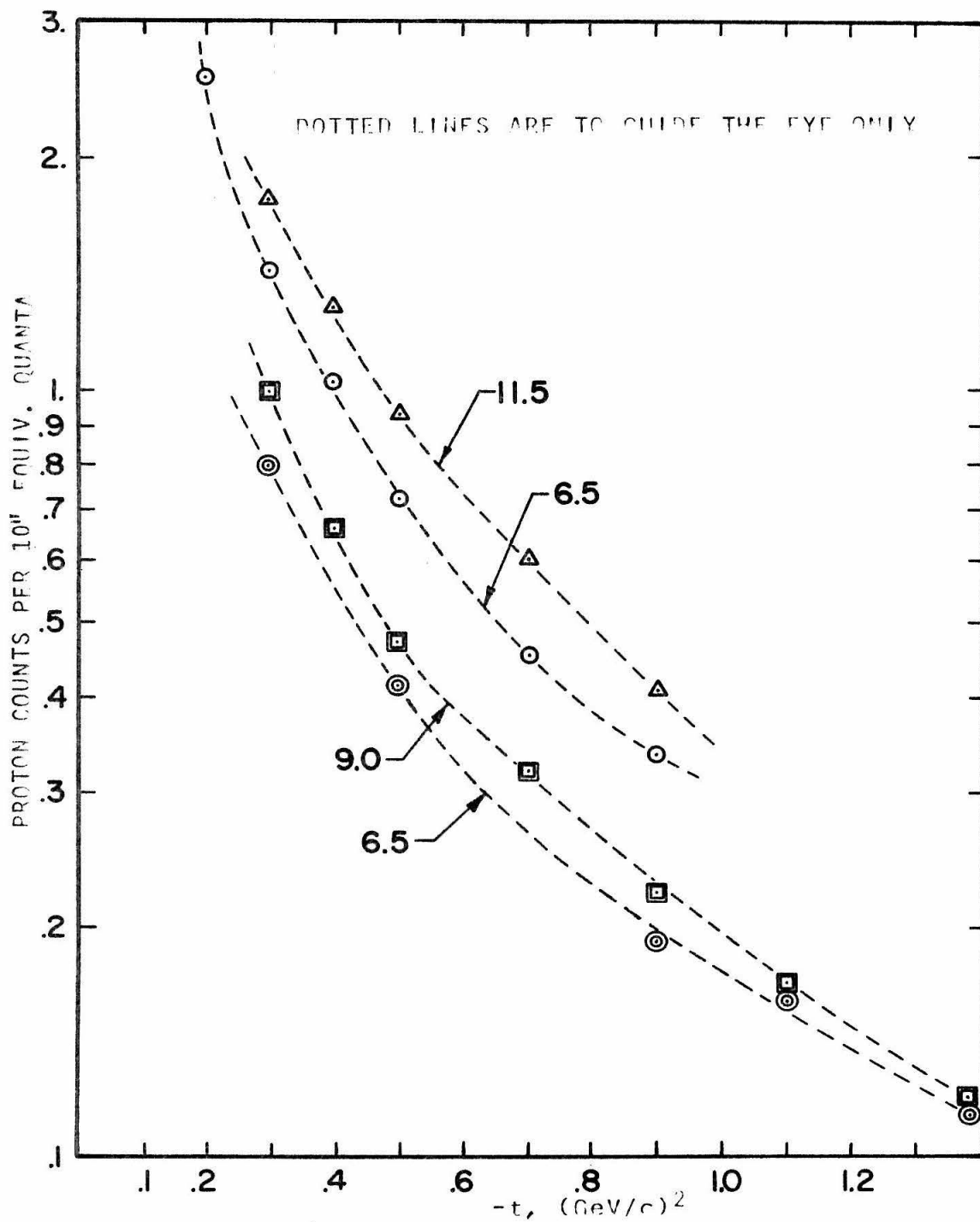


FIGURE 8 Ghost Proton Yield vs. t for Various Photon Energies

Data with doubled (single) symbols were taken with the mask in (out), as with figure 7a (7b). The shape of the background does not appear to have changed with the insertion of the mask.

Possible sources of ghost protons and their likely behavior in the allowed kinematics region will now be discussed.

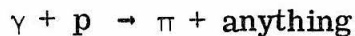
Beam particles can produce protons in interactions with the target structure. Empty target rates were measured by substituting an empty cell for the hydrogen-filled cell in the hydrogen target assembly. Counting rates in the forbidden region were reduced by about a factor of ten. It was found that this low counting rate was roughly independent of angle, and therefore empty target rates are negligible.

Misidentification of pions as protons is a second possible source of background which can be neglected. Even in the worst conditions, at high momentum transfers, fewer than 5 percent of the pions are mistaken for protons. A typical pion flux is indicated in figure 4 as a dashed line. It is clear that even 5 percent of this is small. The smooth variation of pion flux with angle indicates that this source of background cannot imitate or mask a step, so it can be ignored altogether.

A spurious signal might come from protons of the wrong momentum which reach the detectors by traveling through the shielding or bouncing off the walls of the magnet. Such protons should show different times of flight from protons of the proper momentum which reach the detectors in the normal way. Time of flight spectra in the kinematically forbidden region show a proton peak which is just as narrow as the peak in the allowed region. Relatively few particles arrive with a flight time characteristic of neither a proton nor a pion. An additional indication that most protons detected come

through the magnet in the proper way is that if the spectrometer entrance slits are closed down, counting rate decreases linearly with slit opening. Closing the slit entirely reduces the rate in the ghost region to about 3 percent of the full-aperture value.

Empty target counts, pion leakage, and wrong-momentum protons together cannot account for more than 20 percent of the ghost proton background. Thus 80 percent or more of the ghost protons are genuinely protons of the right momentum, whose production is associated with the presence of hydrogen in the target. Since single processes are kinematically forbidden, ghost protons must come from two-step processes. An attempt⁽²³⁾ has been made to calculate at 6 GeV the expected background made entirely in hydrogen from the processes



followed by $\pi + p \rightarrow p + \text{anything}$

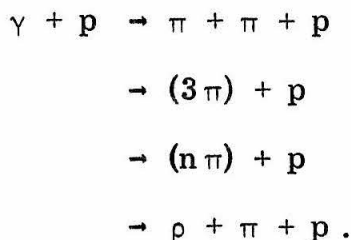
and $\gamma + p \rightarrow \text{nucleon} + \text{anything}$

followed by $\text{nucleon} + p \rightarrow p + \text{anything}$.

DESY 6 GeV bubble chamber data⁽⁵⁾ were used to obtain total pion and total nucleon production cross sections and angle dependences. The calculation roughly reproduces the t dependence, but accounts for only about 20 percent of the ghost protons. These calculations probably underestimate the production level because the second step of the process can also occur in the hydrogen target structure, e. g., the massive copper heat exchanger. The large decrease in ghost level when all but the hydrogen cell was masked from the view of the spectrometer suggests that the underestimation may be substantial.

In sum, the source of ghost protons is not fully understood, though probably most come from two-step processes. A smooth dependence of ghost proton rate with angle is expected.

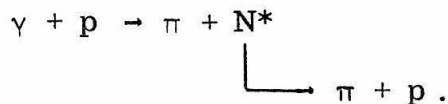
If the spectrometer angle is set to observe recoil protons in the kinematically allowed region, a second major source of background is encountered. As mentioned in chapter II, with the missing mass spectrometer technique recoil protons are assumed to be produced in two-body reactions, so three- or many-body final states appear as background. This class of reactions includes processes like



The thresholds for these reactions are easily computed, but the angle dependence of the yield depends on the matrix elements, phase space, kinematics and the bremsstrahlung spectrum in a complicated way. For a few of the reactions bubble chamber experiments give an idea of the proton spectrum in a limited range of momentum transfers and photon energies. Extrapolations to our region of interest would probably be inaccurate. Attempting to introduce this kind of information into the fitting procedure with free parameters is very likely to result in physically unreasonable fits from too many parameters. For these reasons many body final state reactions are assumed to be too complicated to compute individually.

If a particular many-body production mechanism is strong and rises rapidly at threshold, it will produce a step similar to that from production of a particle. However, phase space factors make rapid rises at threshold unlikely; also, for high effective missing mass, so many channels are open that it is unlikely any given one will be large. In practice this source of background appears to be well approximated by a smooth curve, with the possible exception of two- and three-pion production.

A similar type of background comes from production of baryon resonances which decay to yield the observed proton, e.g.,



A Monte Carlo calculation of this reaction indicates that the proton spectrum spreads smoothly over a broad range of angles. In addition the total number of protons seen from these processes is small.

Protons can also be produced in the decay of direct channel resonances like



Known strongly produced resonances require photons with energy less than 2 GeV. Although these are present in the bremsstrahlung beam, in most cases the protons produced in the decay come out at angles smaller than the angles of interest. However, at low endpoint energies and momentum transfers large broad peaks can interfere with analyses of the yield curves. A simple bremsstrahlung sub-

traction restores the data to usefulness. The mass search described and illustrated in chapter V is an excellent example.

D. Sample Data

Figure 9 shows a representative sample of yield curves obtained in this experiment. The sample was chosen to represent the average quality of the data and to show the complete mass spectrum. This latter requirement eliminated some of the highest quality data, which were taken to study individual particles. Subtracted curves as well as yield curves are shown, in order of increasing momentum transfer. Data with the same t are in order of increasing energy. Each yield curve is labelled with the endpoint energy (or energies) and the momentum transfer squared. The horizontal axis is threshold missing mass squared as computed from equation (III-1) substituting E_0 for k . Proton yield per 10^{11} equivalent quanta is plotted vertically. Each point is the rate observed in an angle bin; the spacing between points is about constant on an angular scale, and the spacing on a mass squared scale depends on kinematics. Error bars reflect counting statistics only. The points with error bars at the top of the figures are deviations of the data from the fit on a one-, two-, or five-times expanded scale.

The reader should be able to notice the following qualitative features of the curves. As momentum transfer increases and as energy increases, each angle bin defines a larger range of missing mass. At the highest t and photon energy the distance between points on a mass scale begins to make distinguishing steps difficult. Angle resolution also becomes poor at low momentum transfer because protons are multiple scattered more. At the lowest t it is very

FIGURE 9

Sample Yield Curves

Data are arranged in order of increasing momentum transfer and endpoint energy. Each part of the figure is labeled with the endpoint energy E in GeV, and t in $(\text{GeV}/c)^2$. Threshold missing mass increases along the abscissa and observed proton yield along the ordinate. Error bars are statistical. As in the previous figures the smooth curves are fits to particle production yields, background and the total yield. Points at the top of each figure represent deviations of the observed yield from the fit. In a few cases the interpolating plotting program has added structure to the fitting curves; this is not significant.

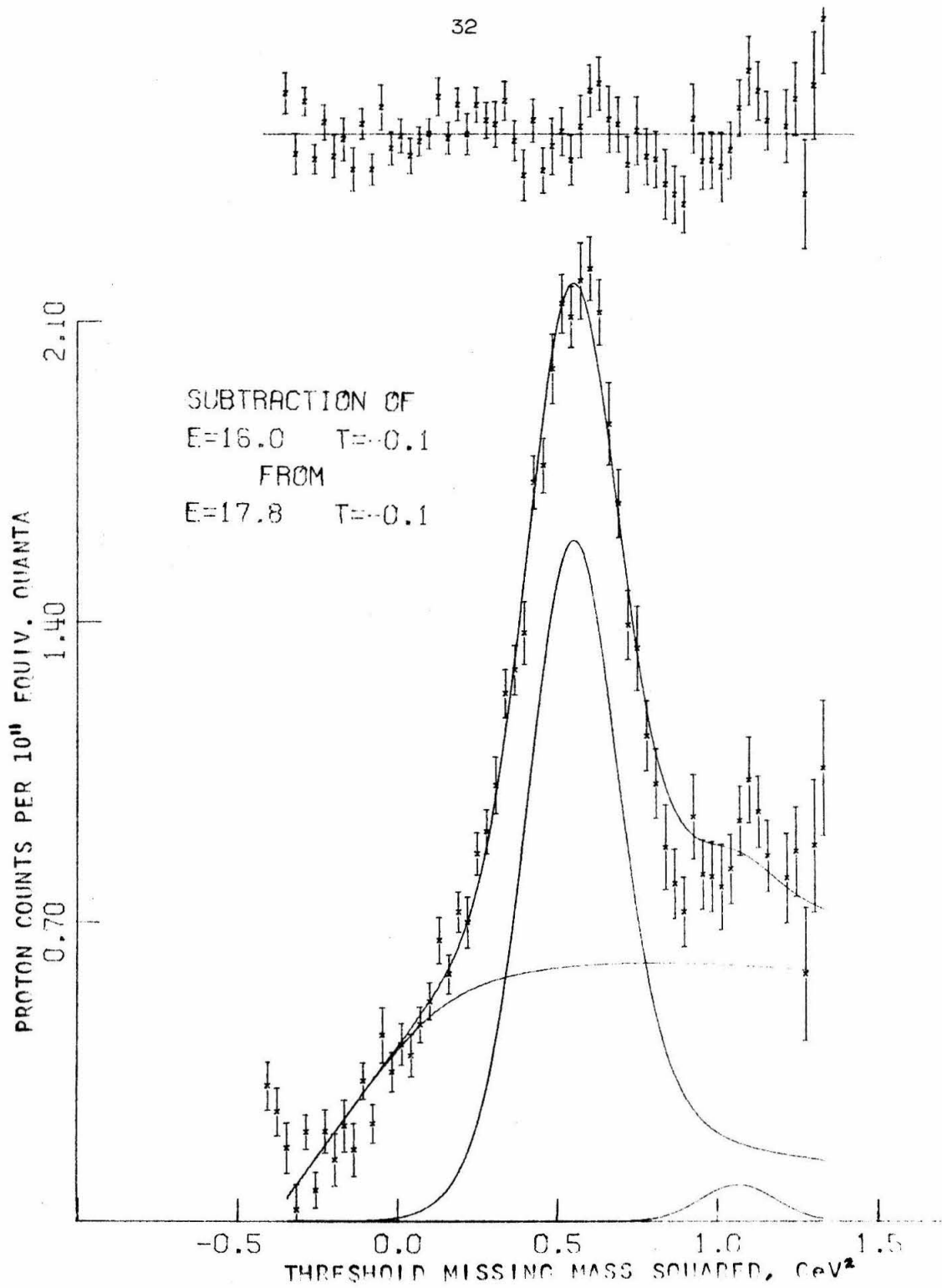


FIGURE 9a

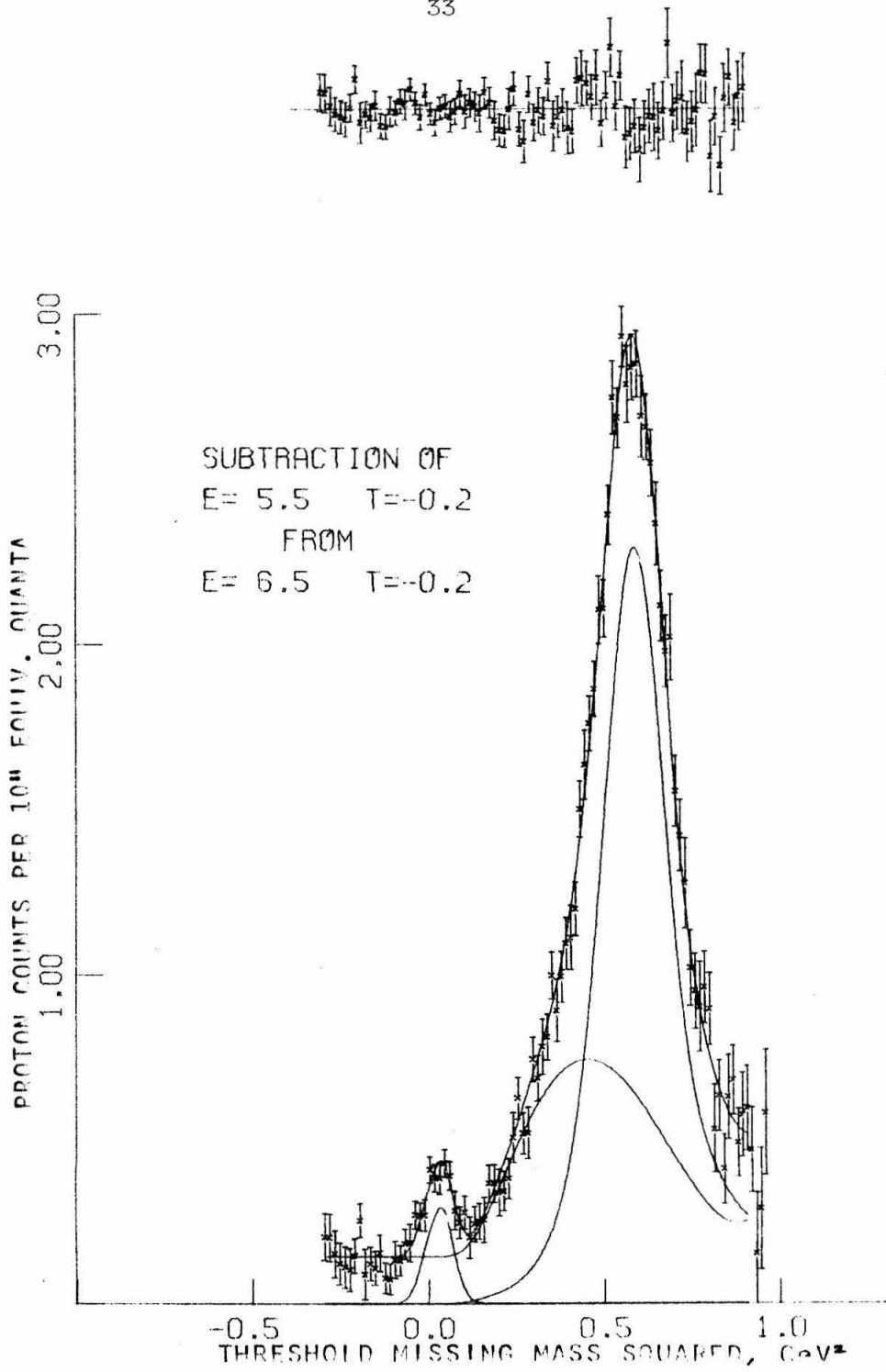


FIGURE 9b

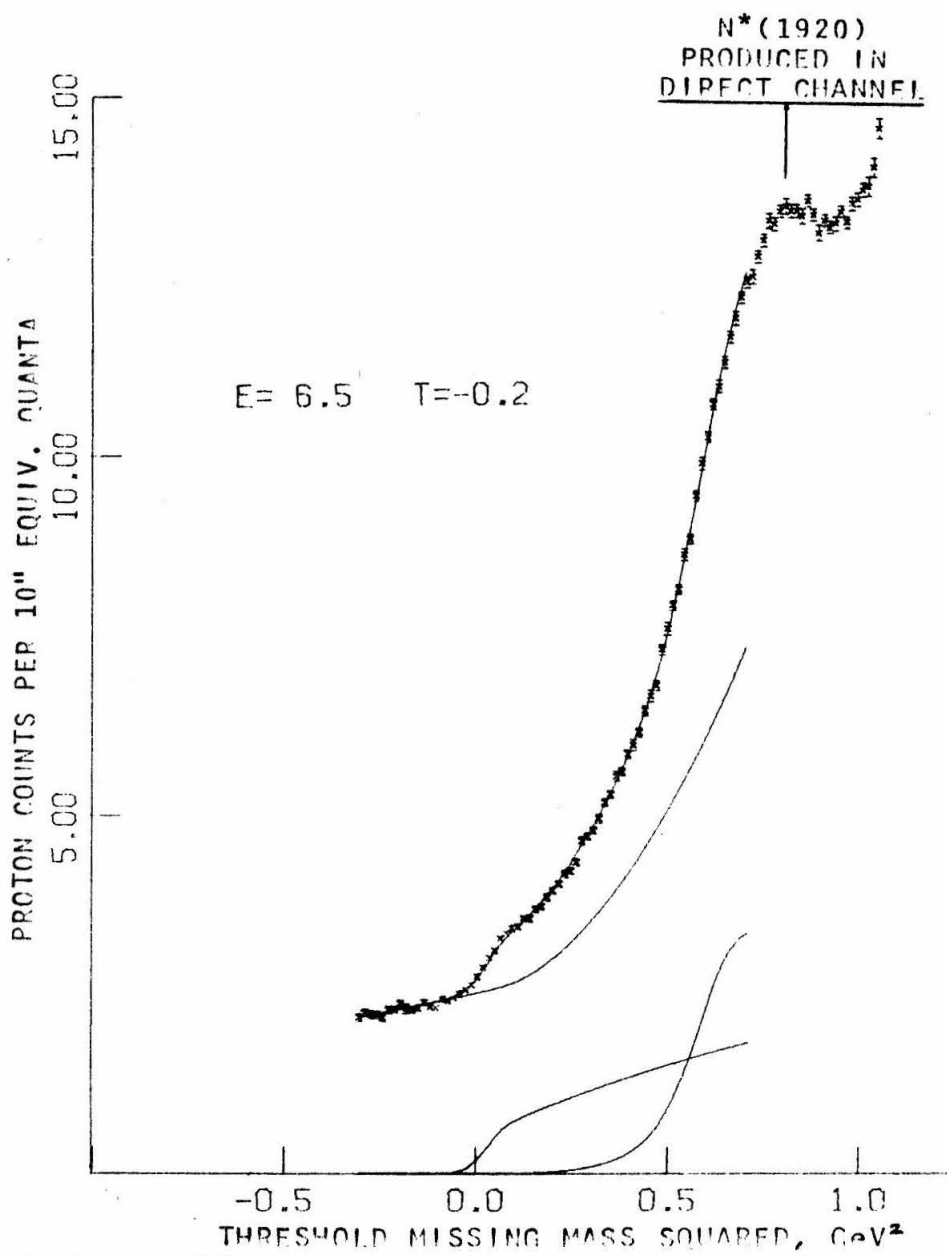


FIGURE 9c

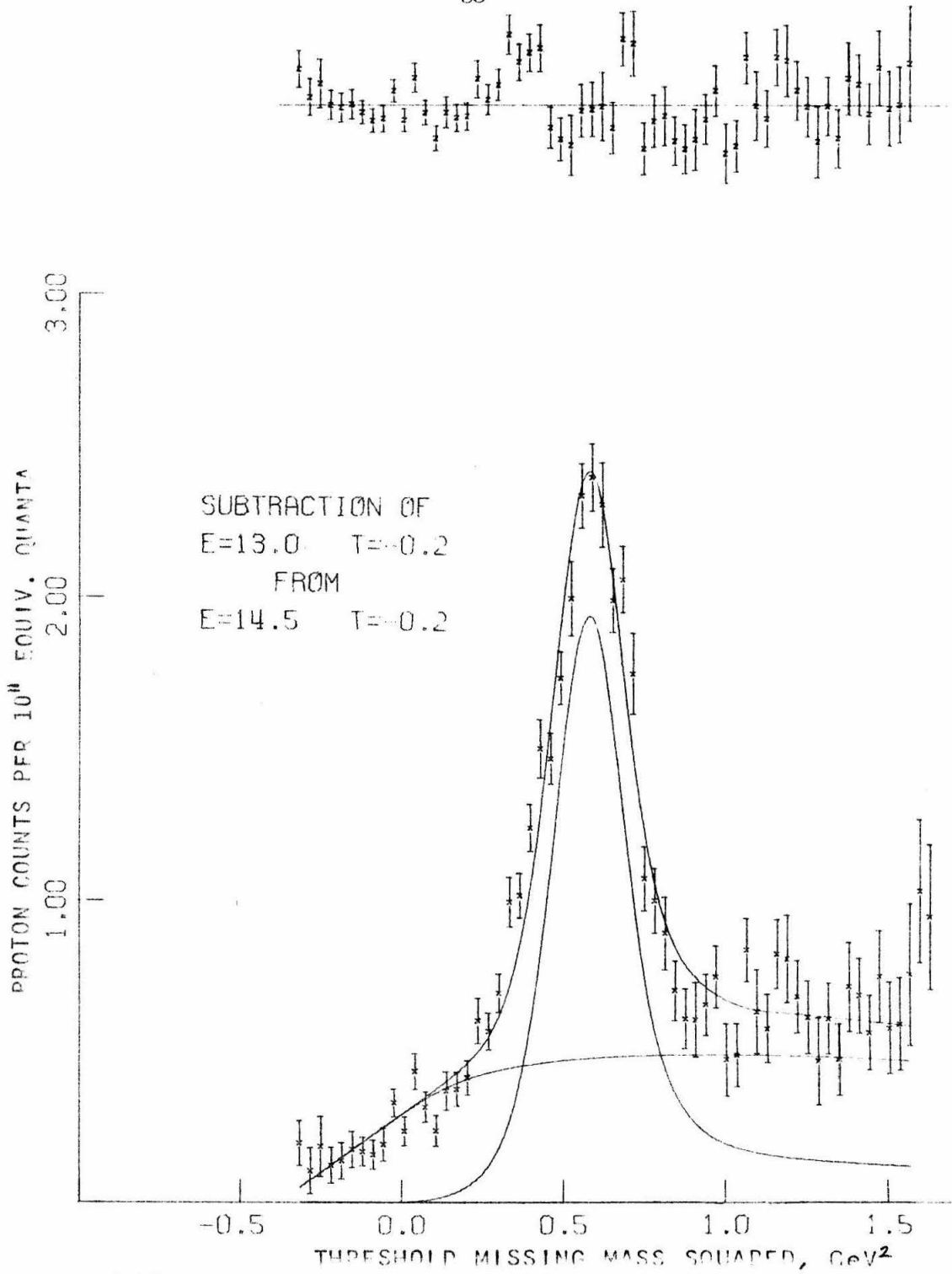


FIGURE 9d

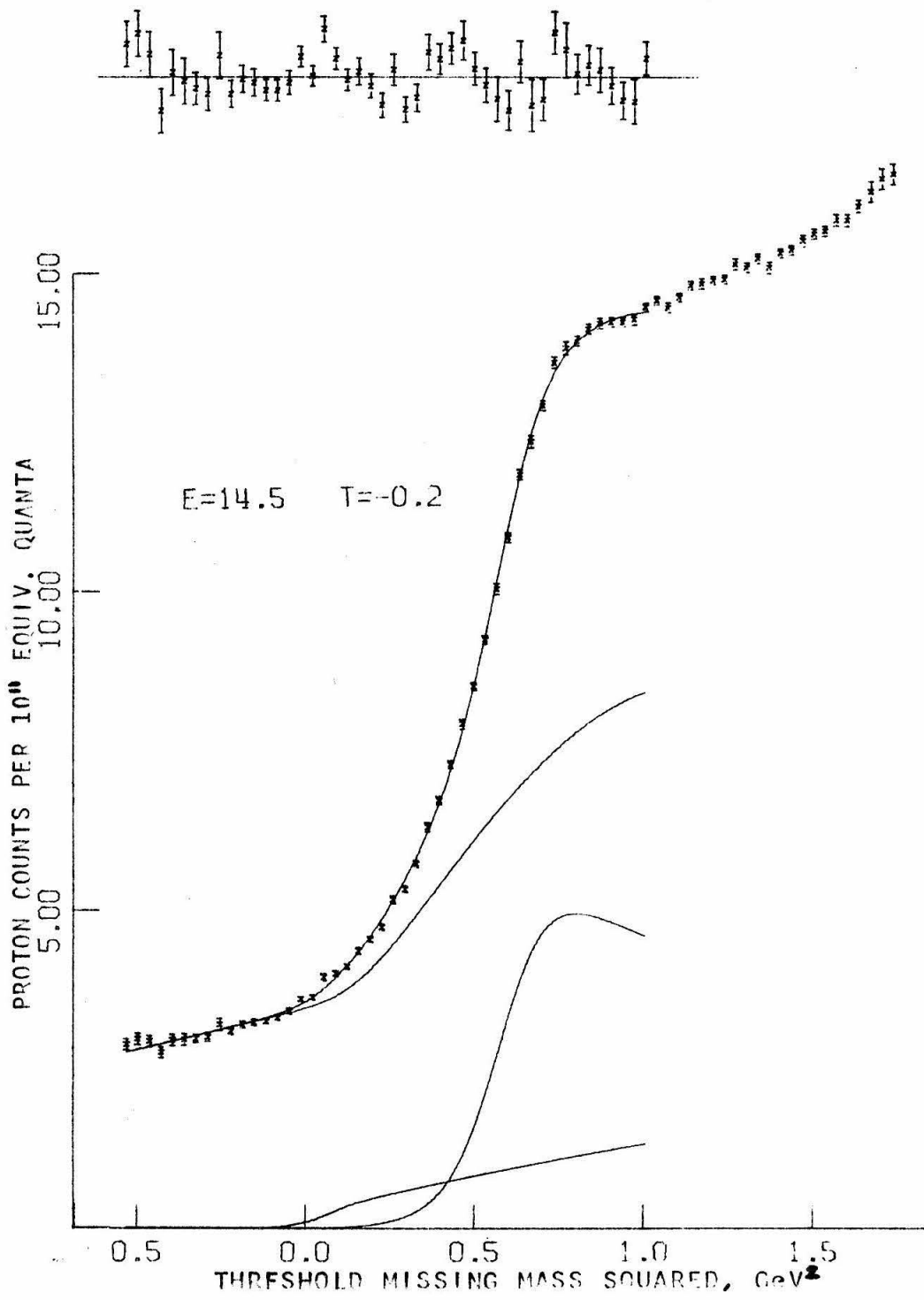


FIGURE 9e

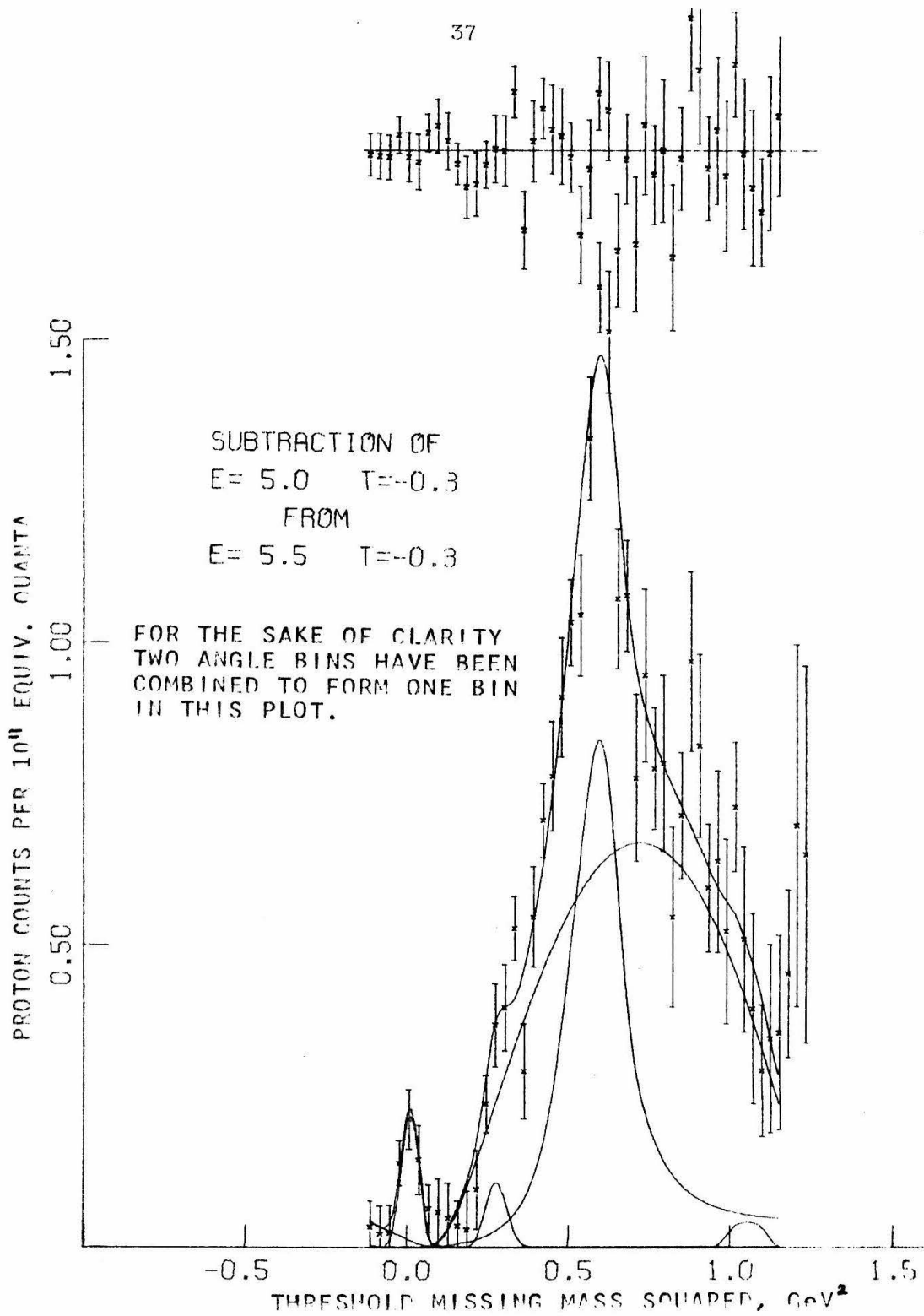


FIGURE 9f

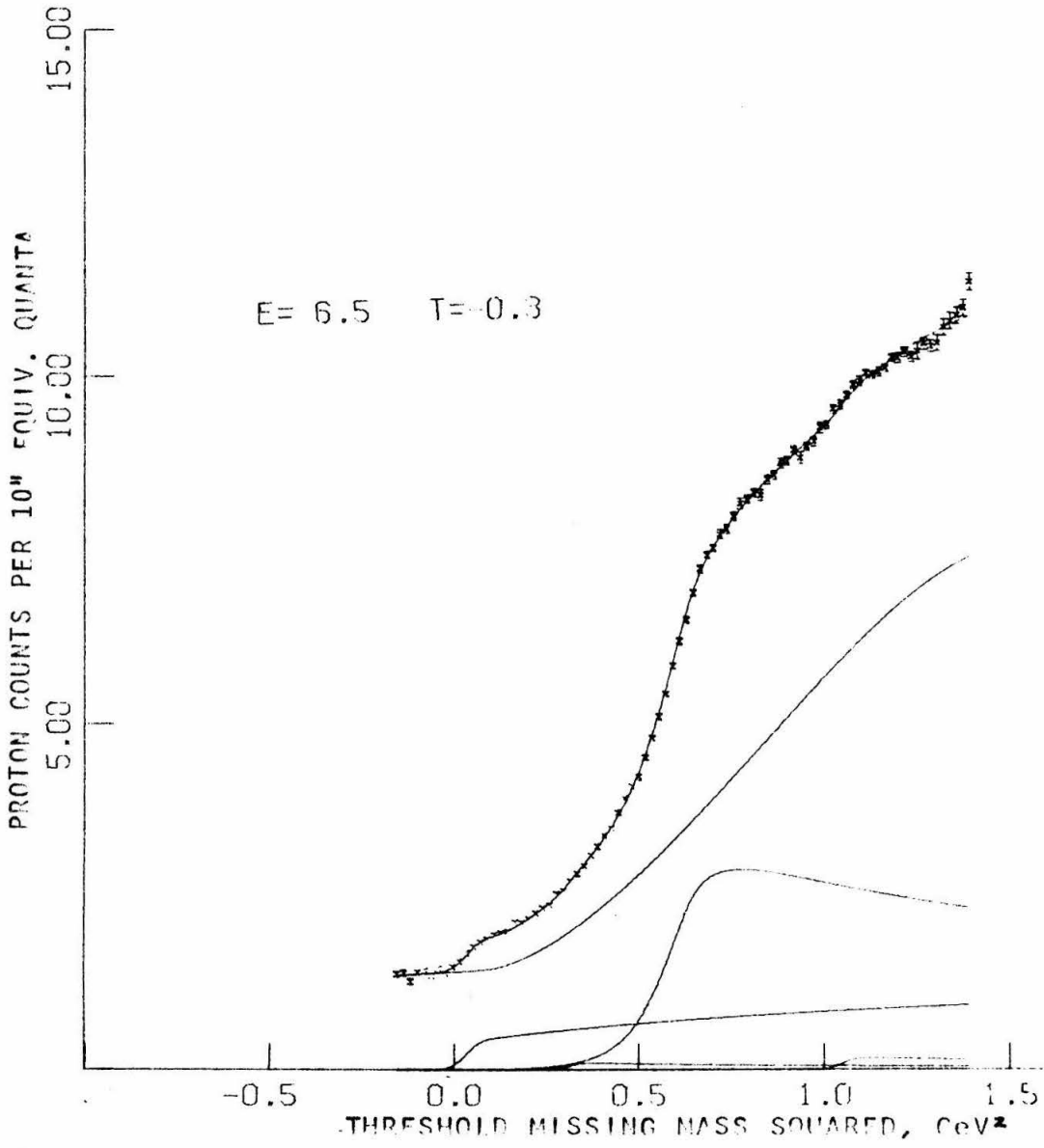


FIGURE 9g

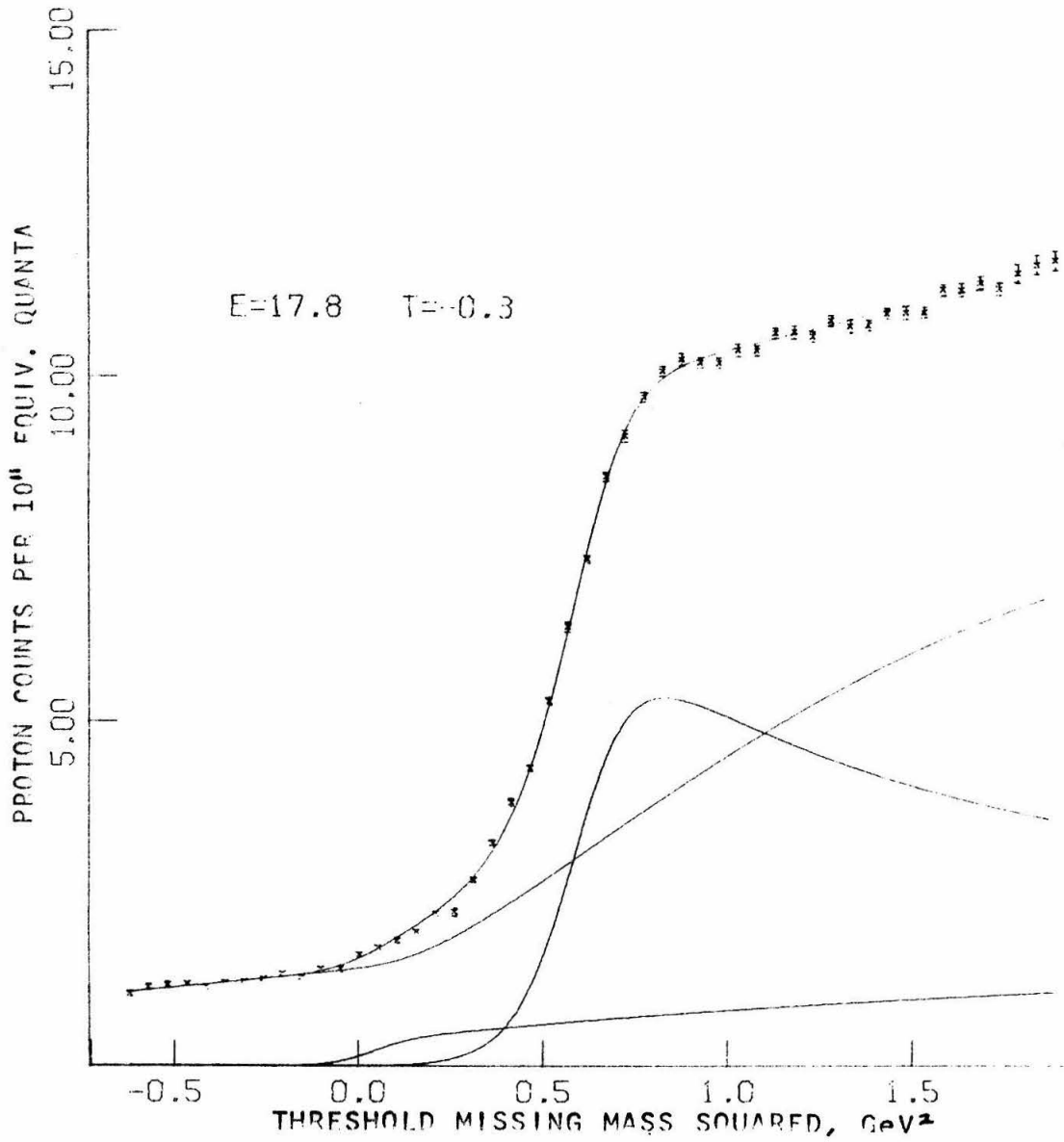


FIGURE 9h

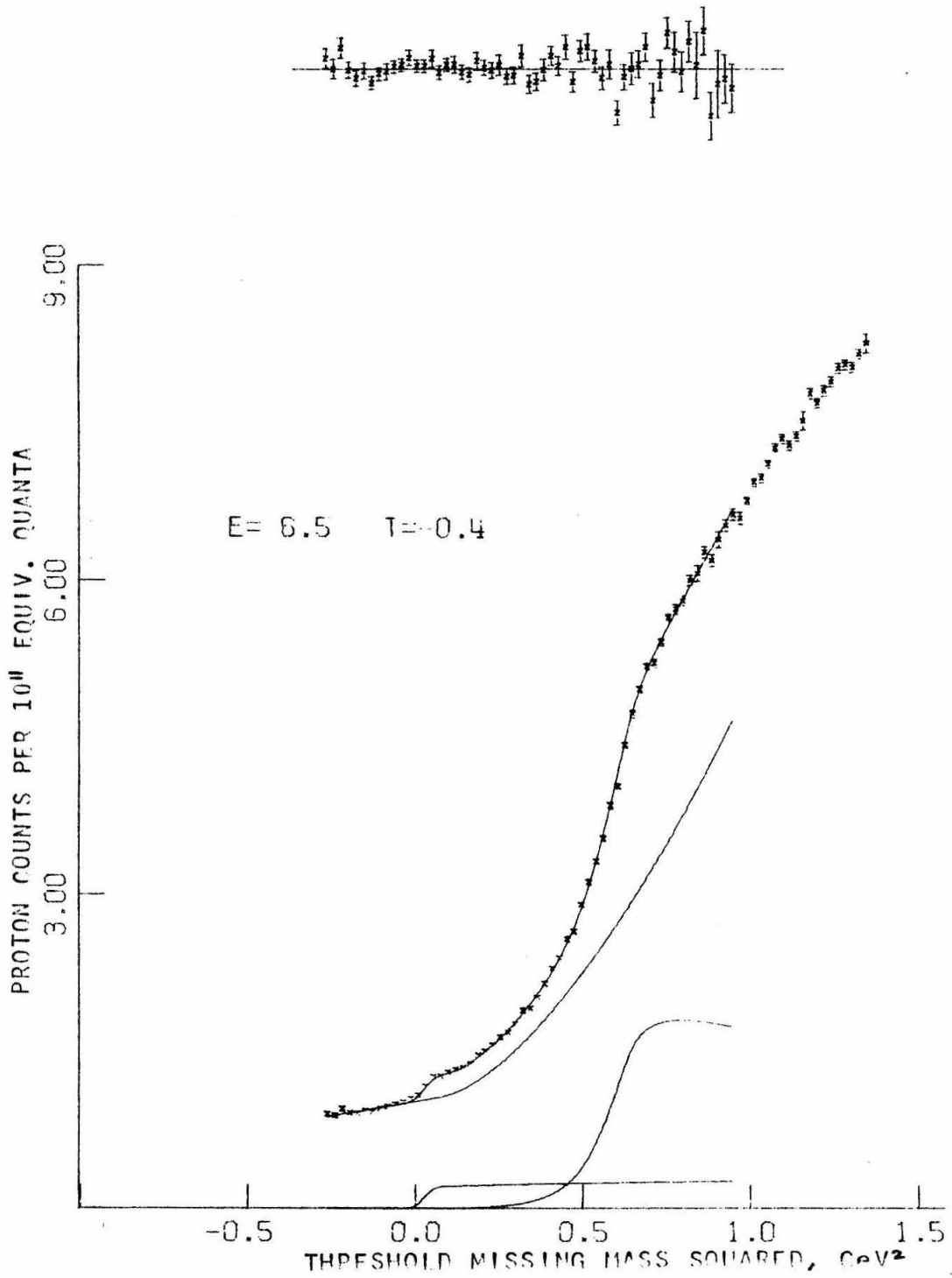


FIGURE 91

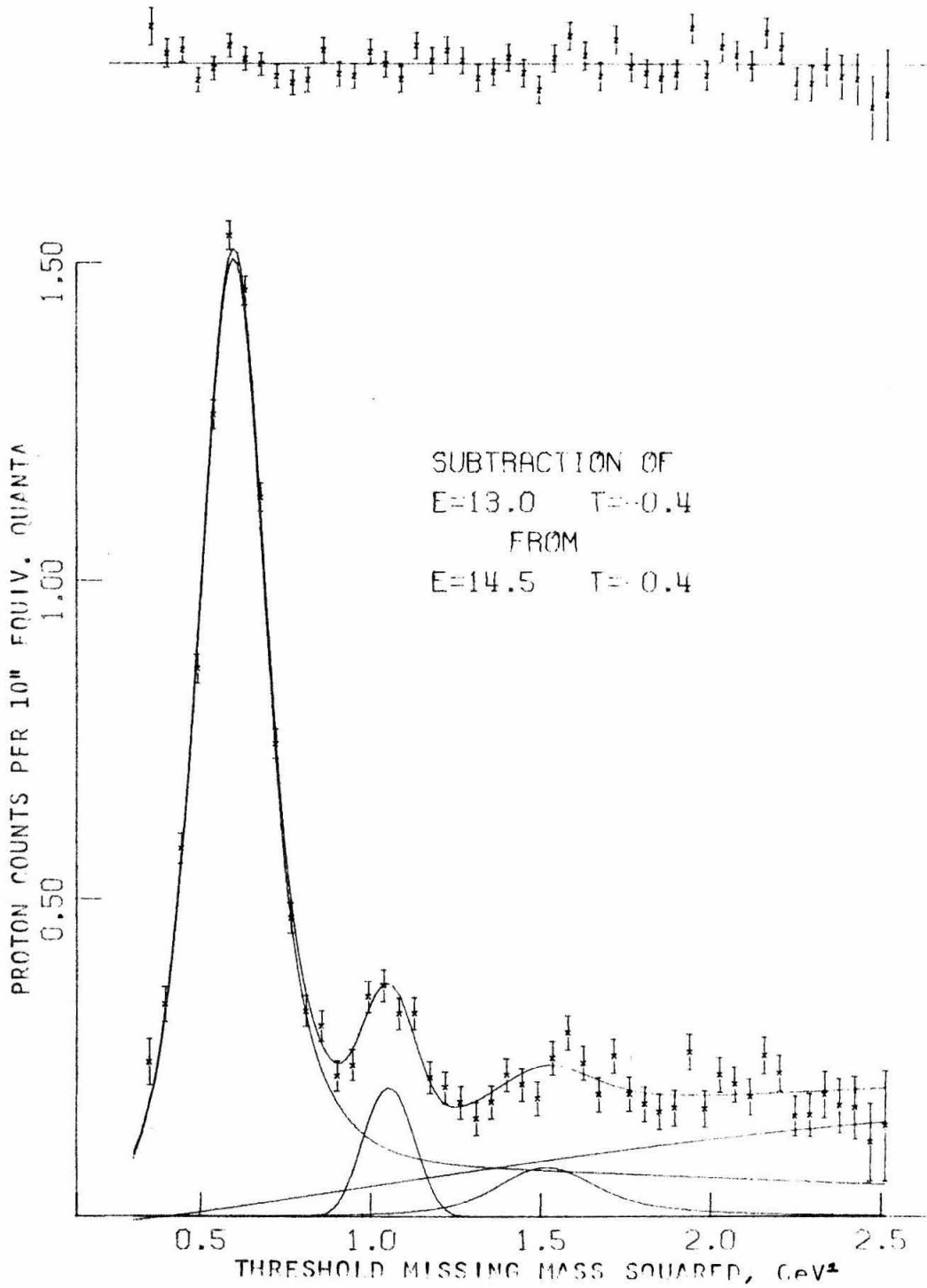


FIGURE 9j

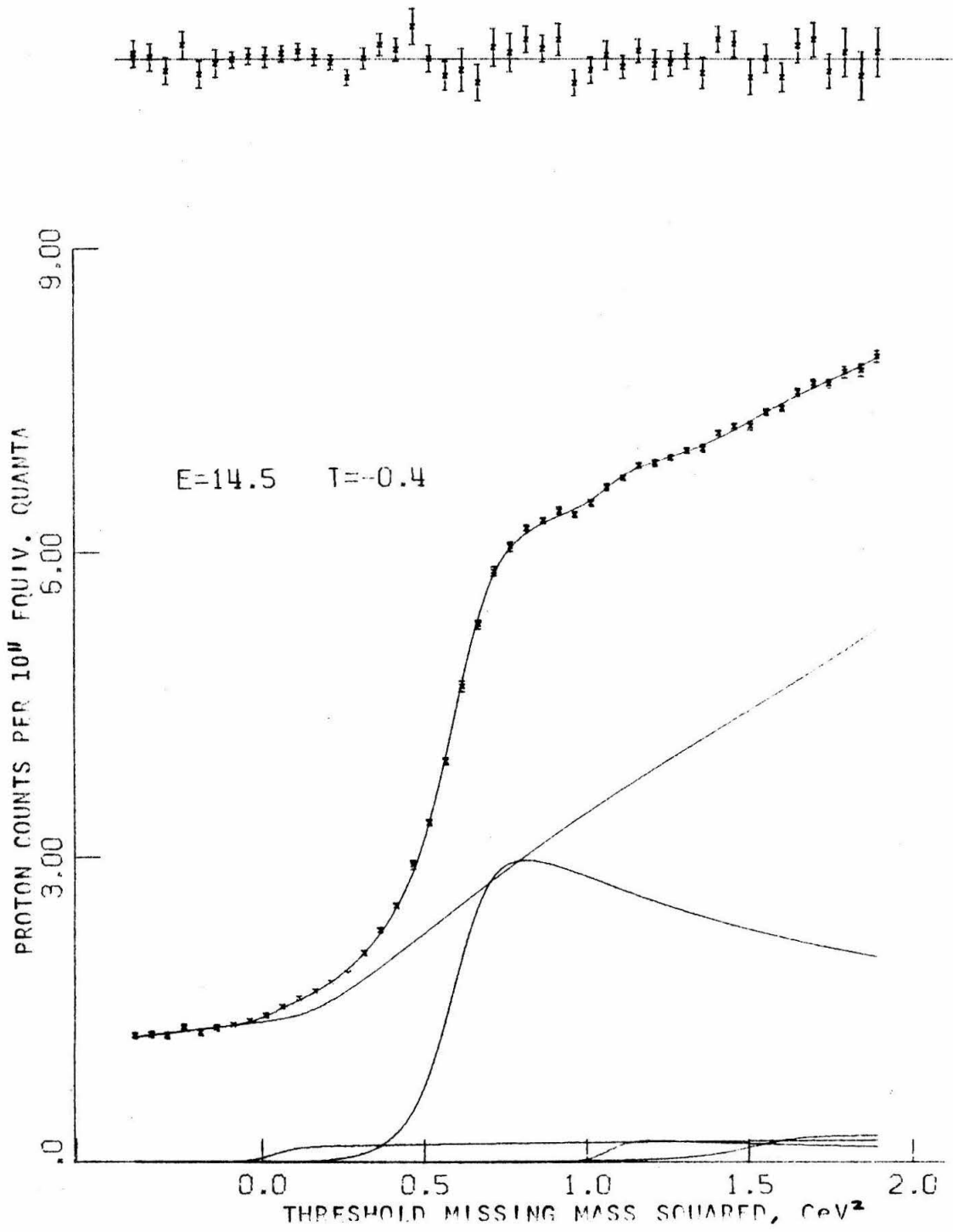


FIGURE 9k

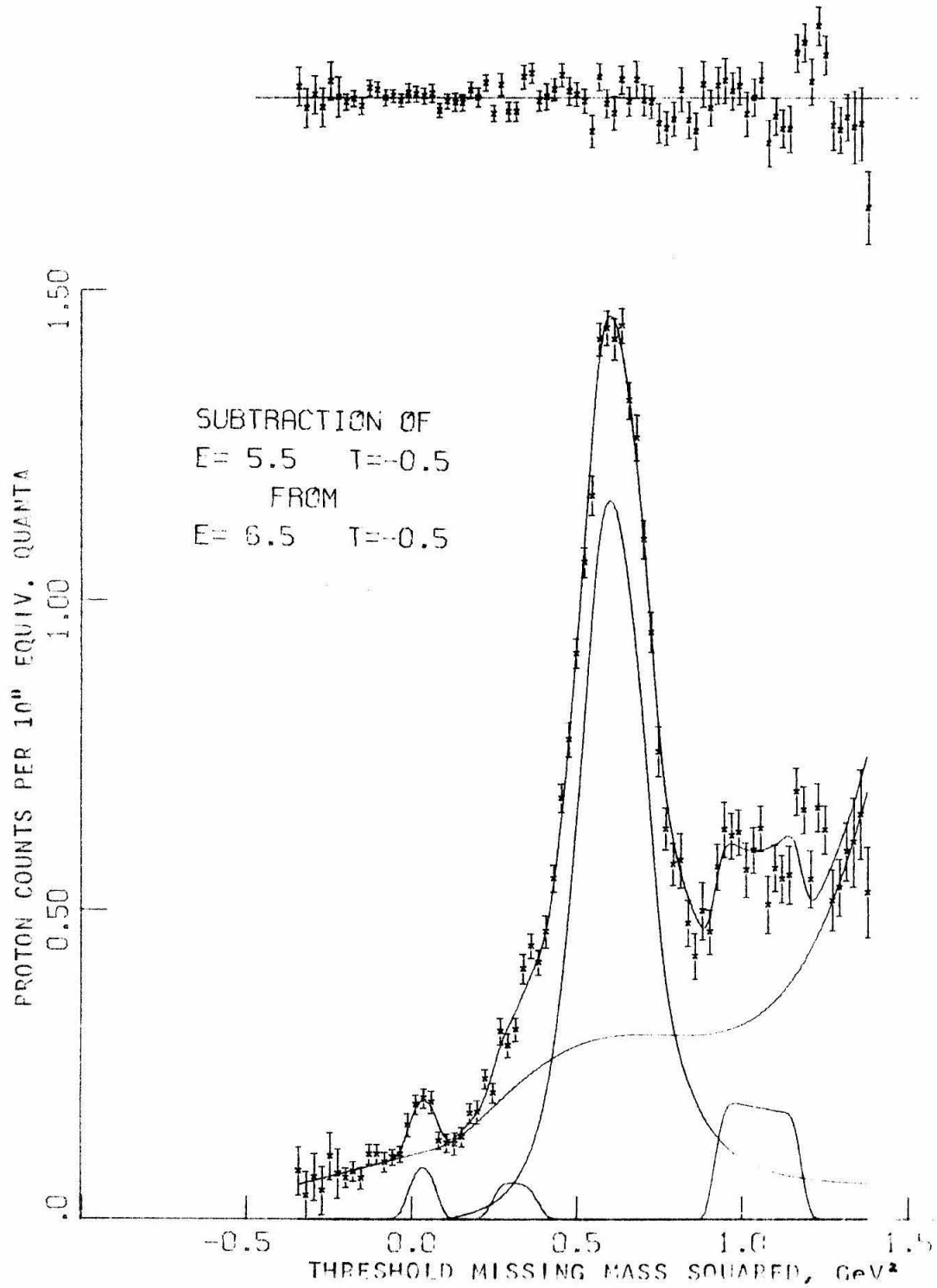


FIGURE 91

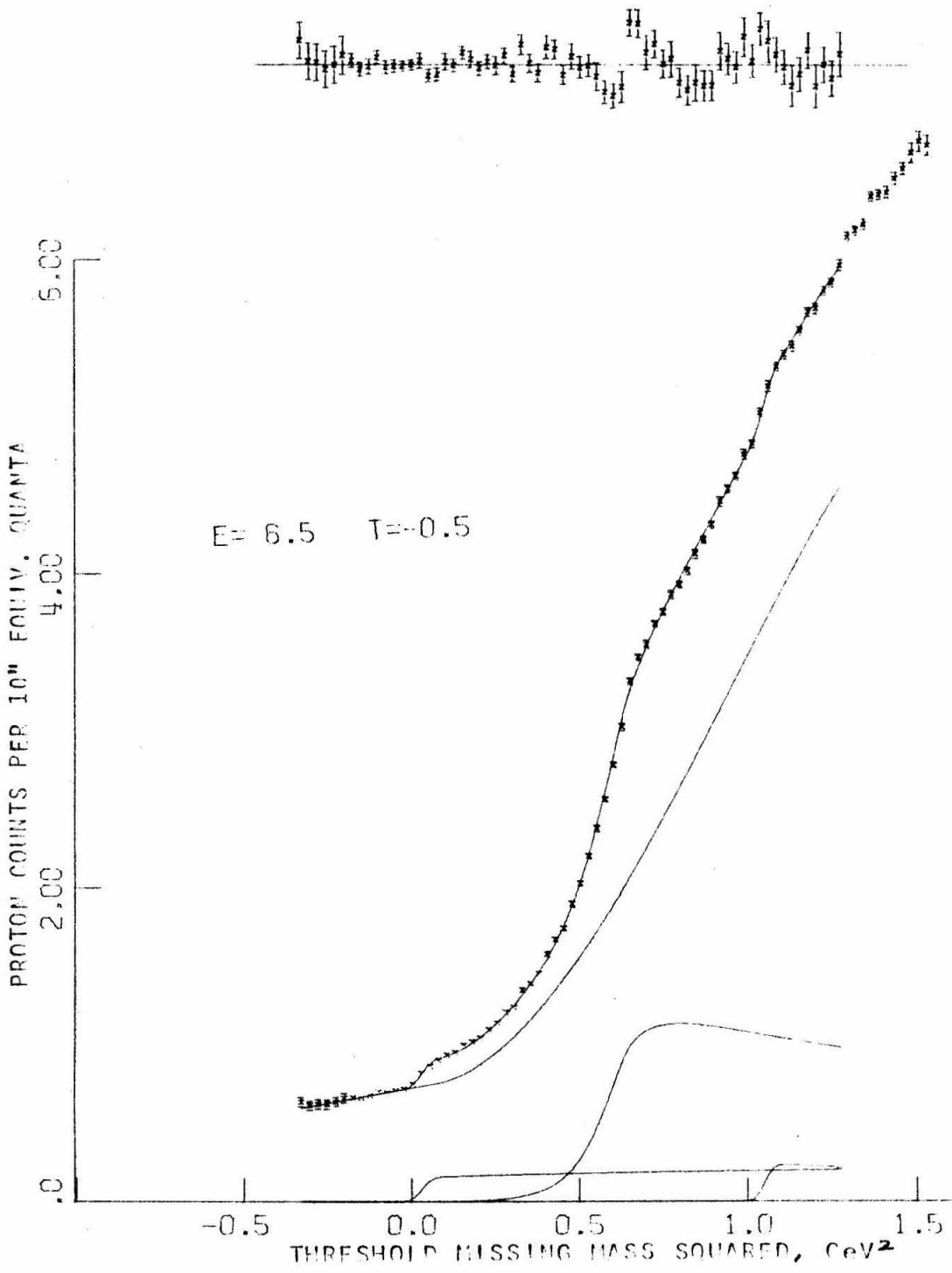


FIGURE 9m

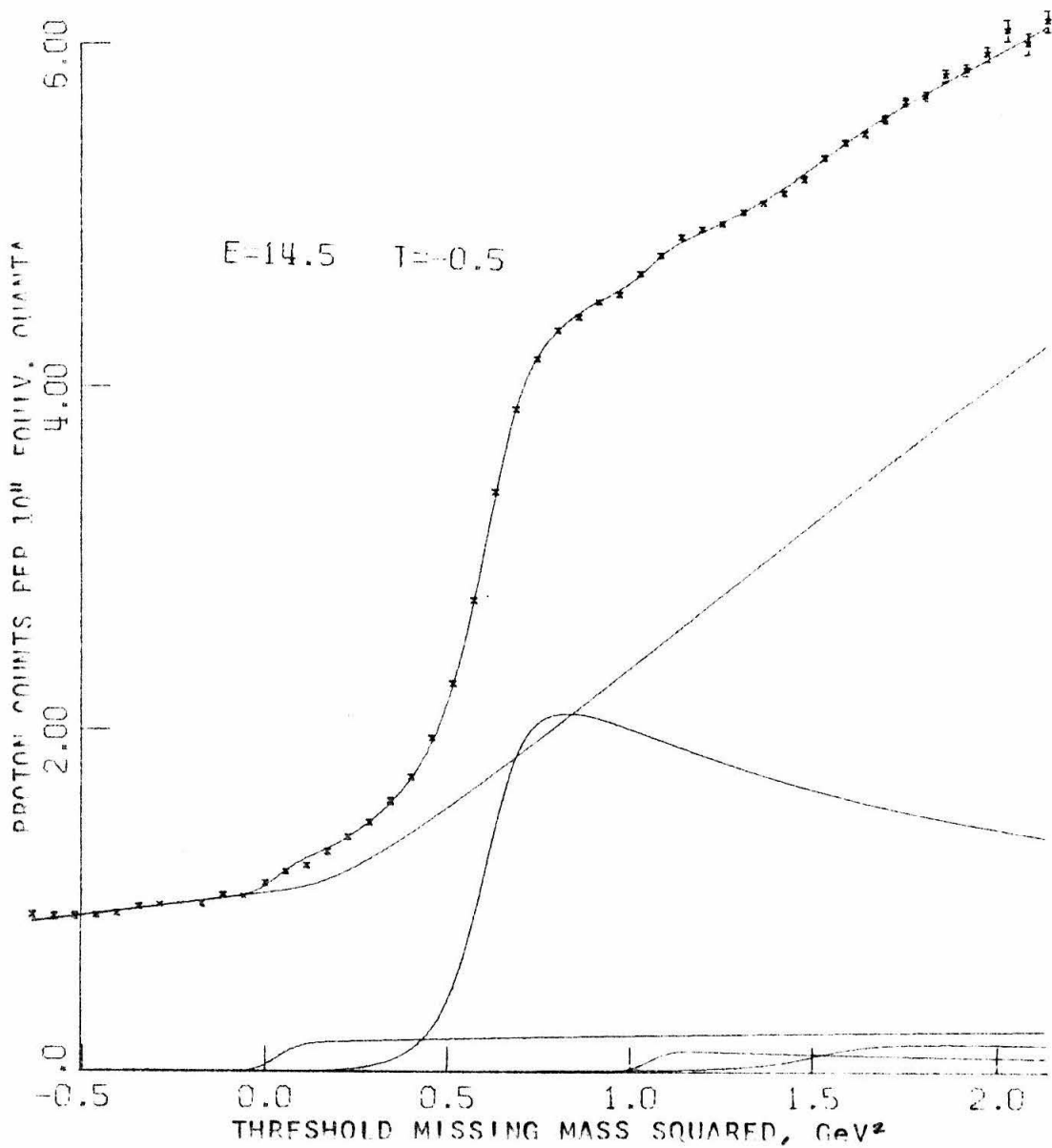
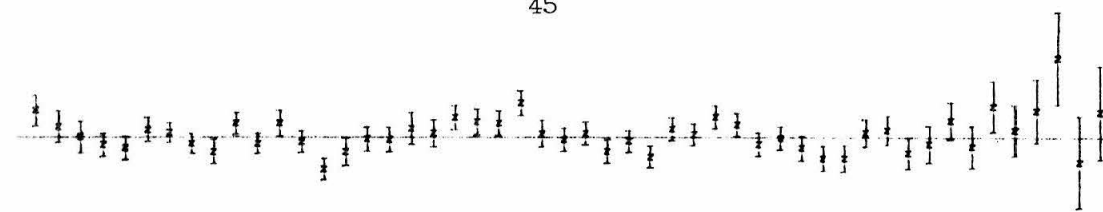


FIGURE 9n

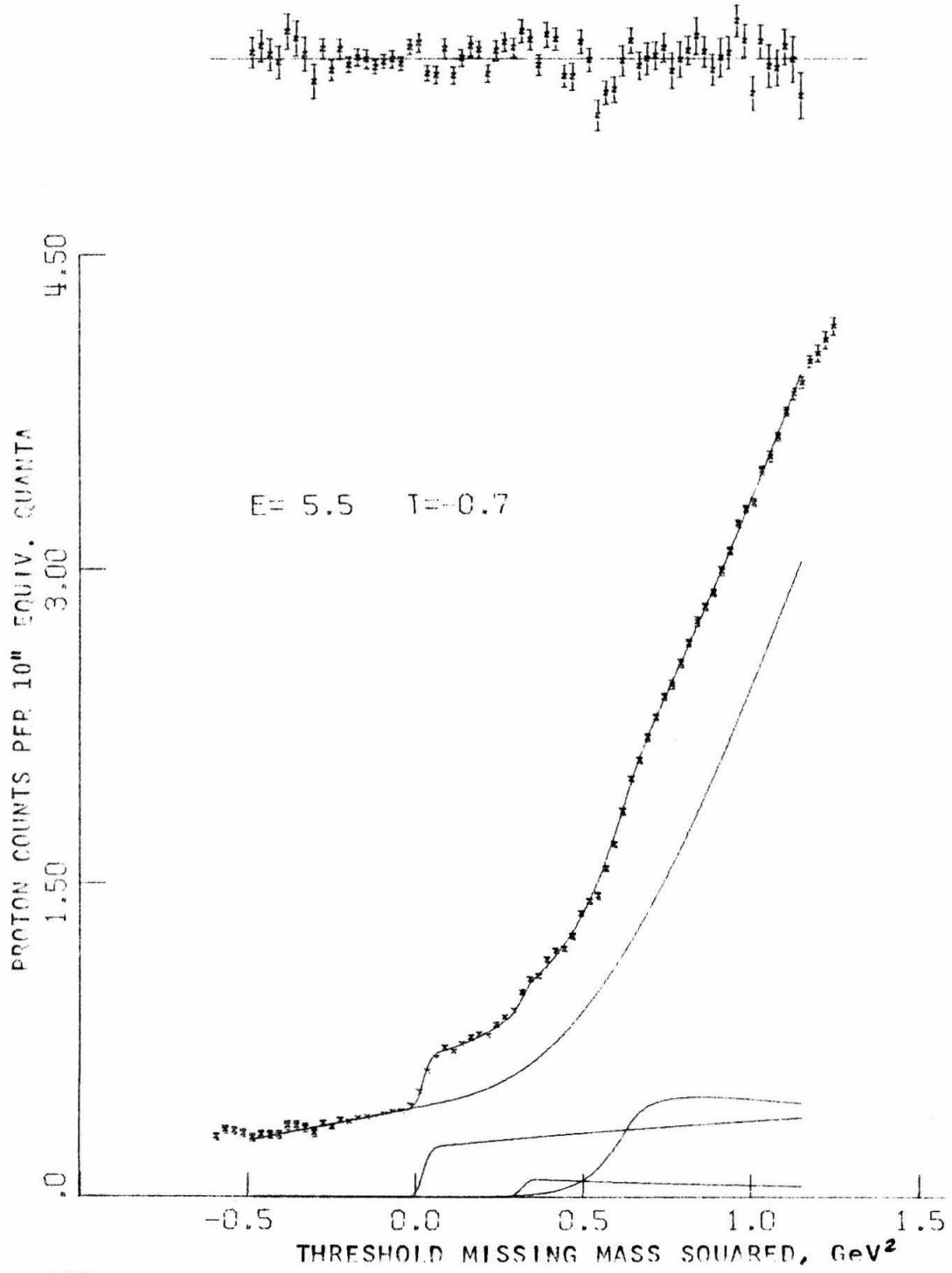


FIGURE 9o

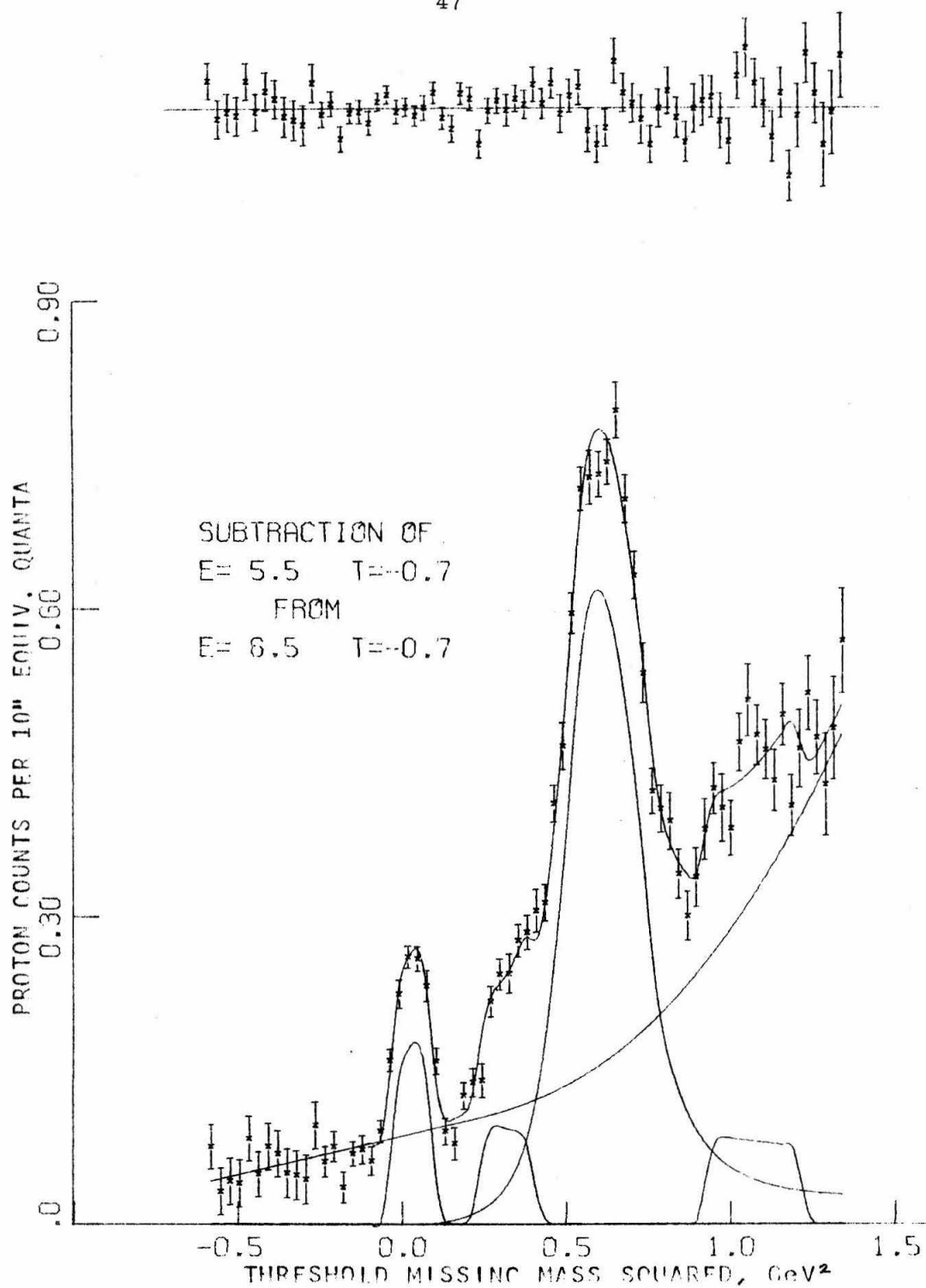


FIGURE 9p

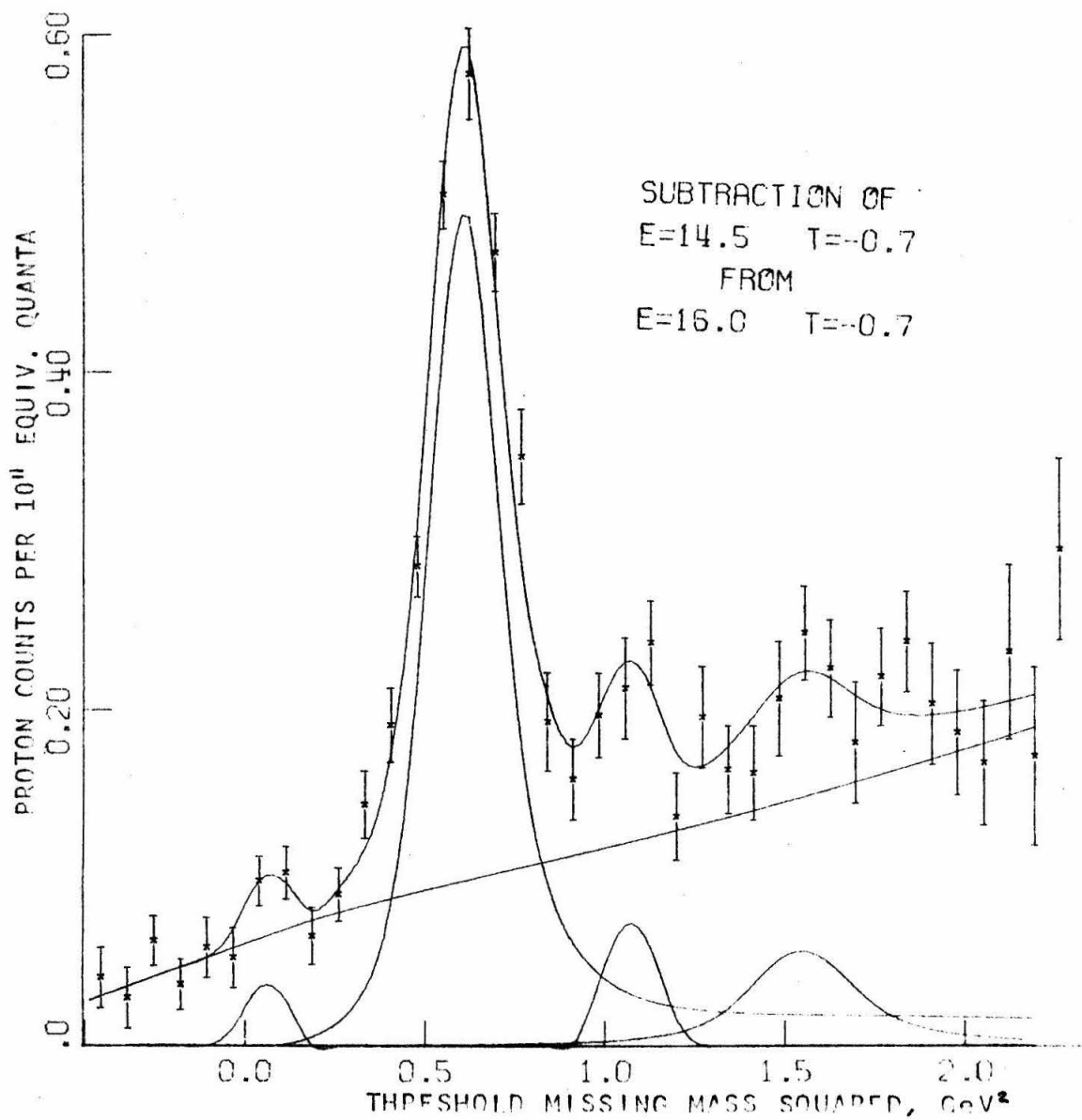


FIGURE 9q

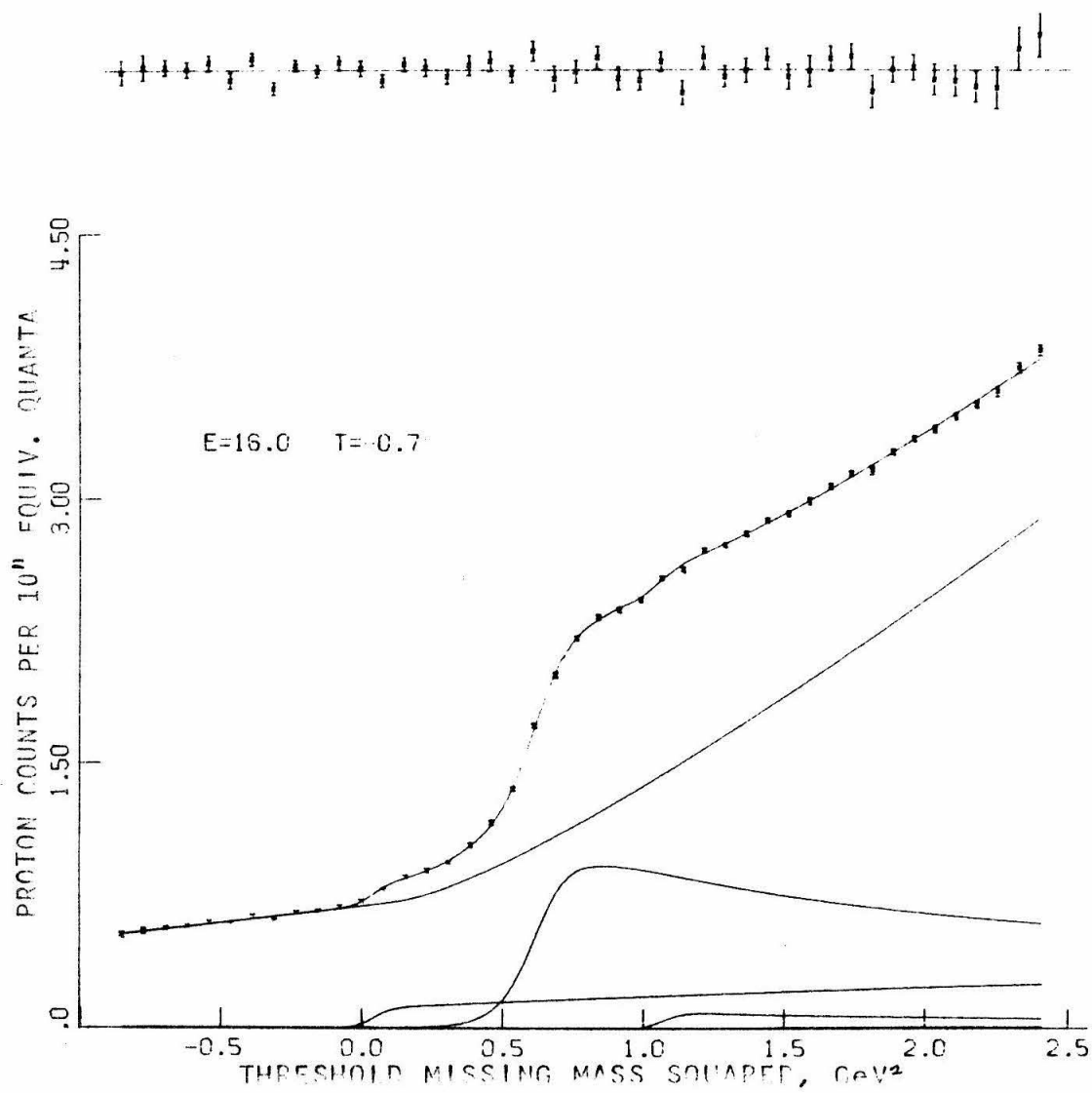


FIGURE 9r

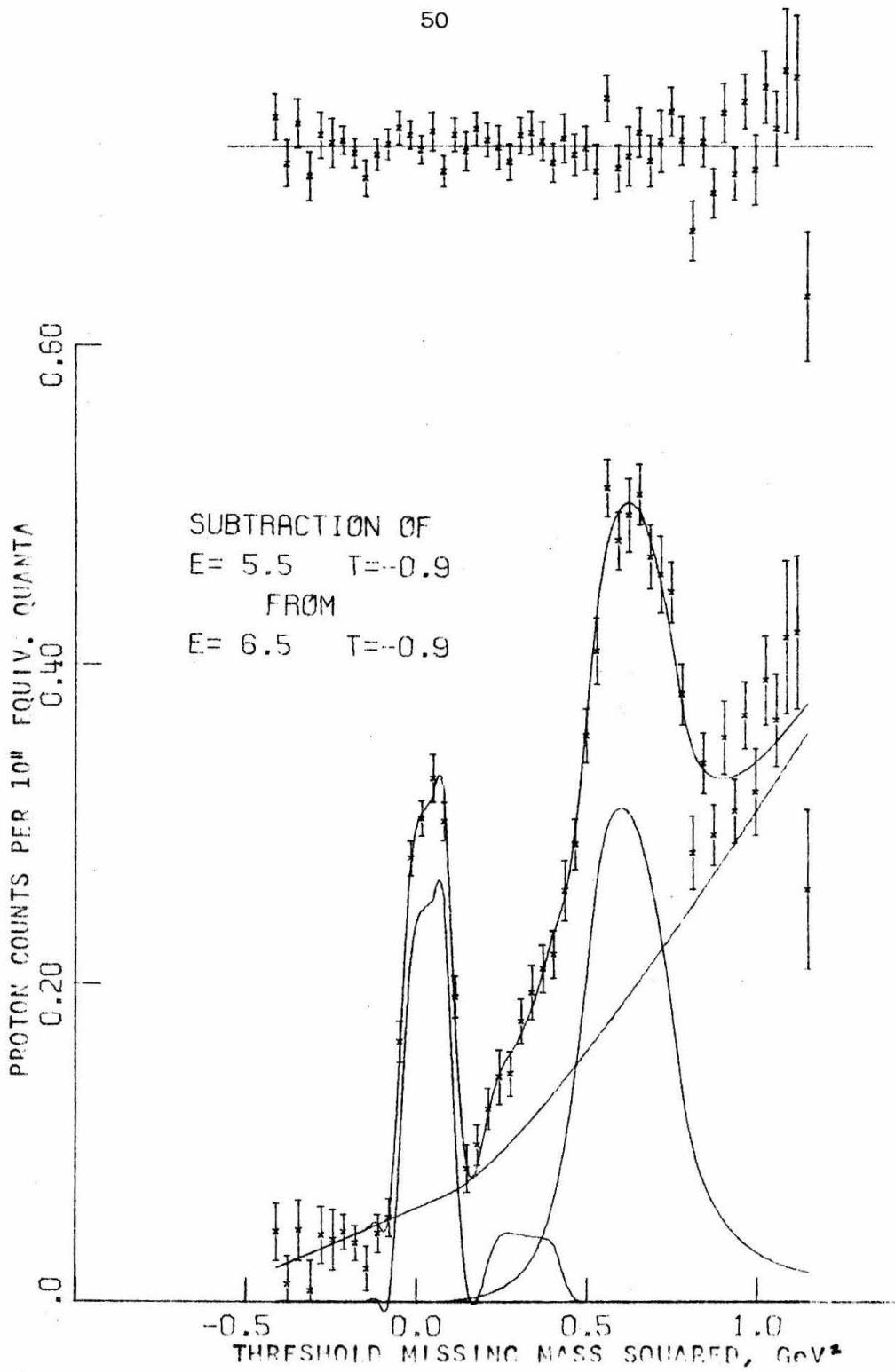


FIGURE 9s

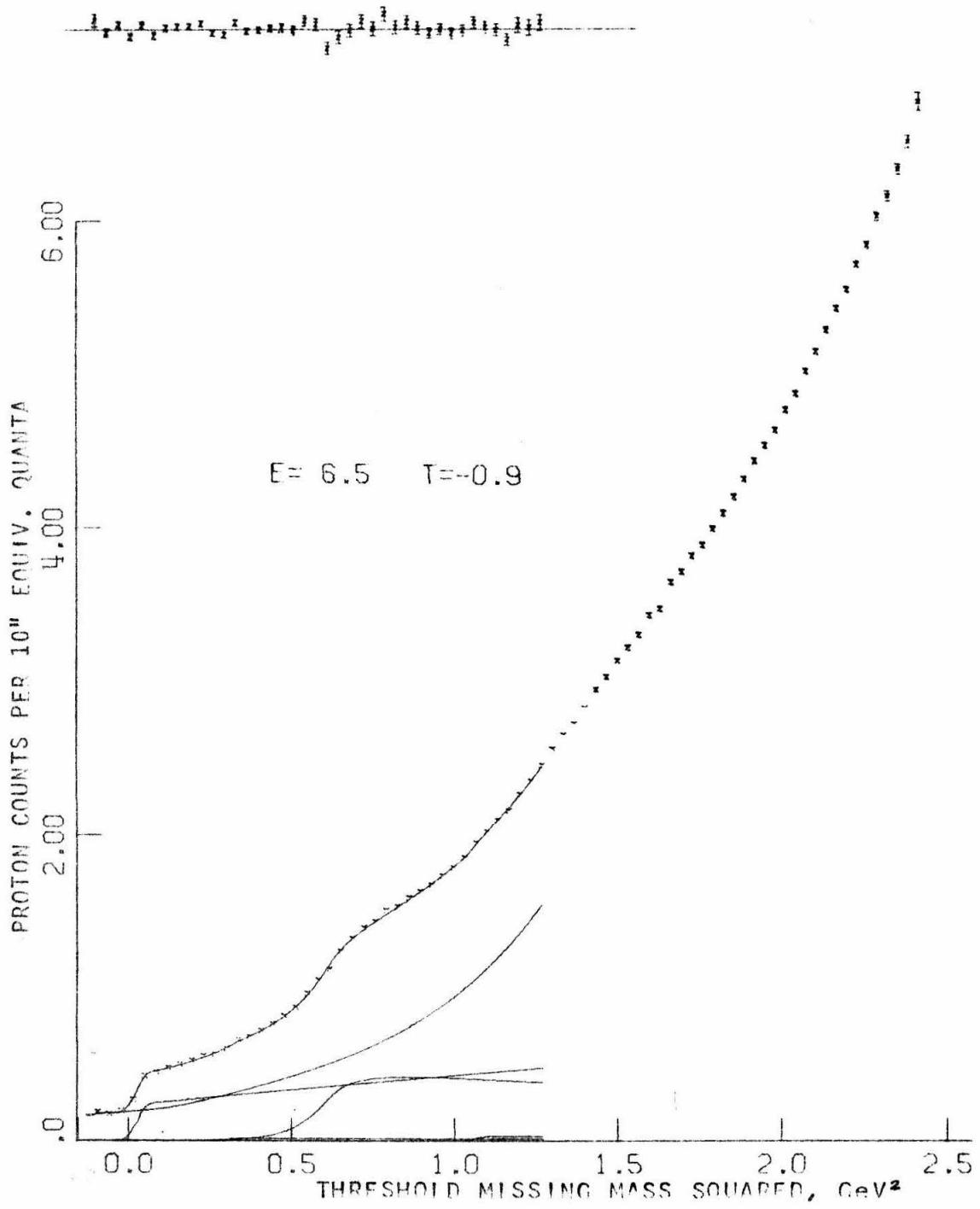


FIGURE 9t

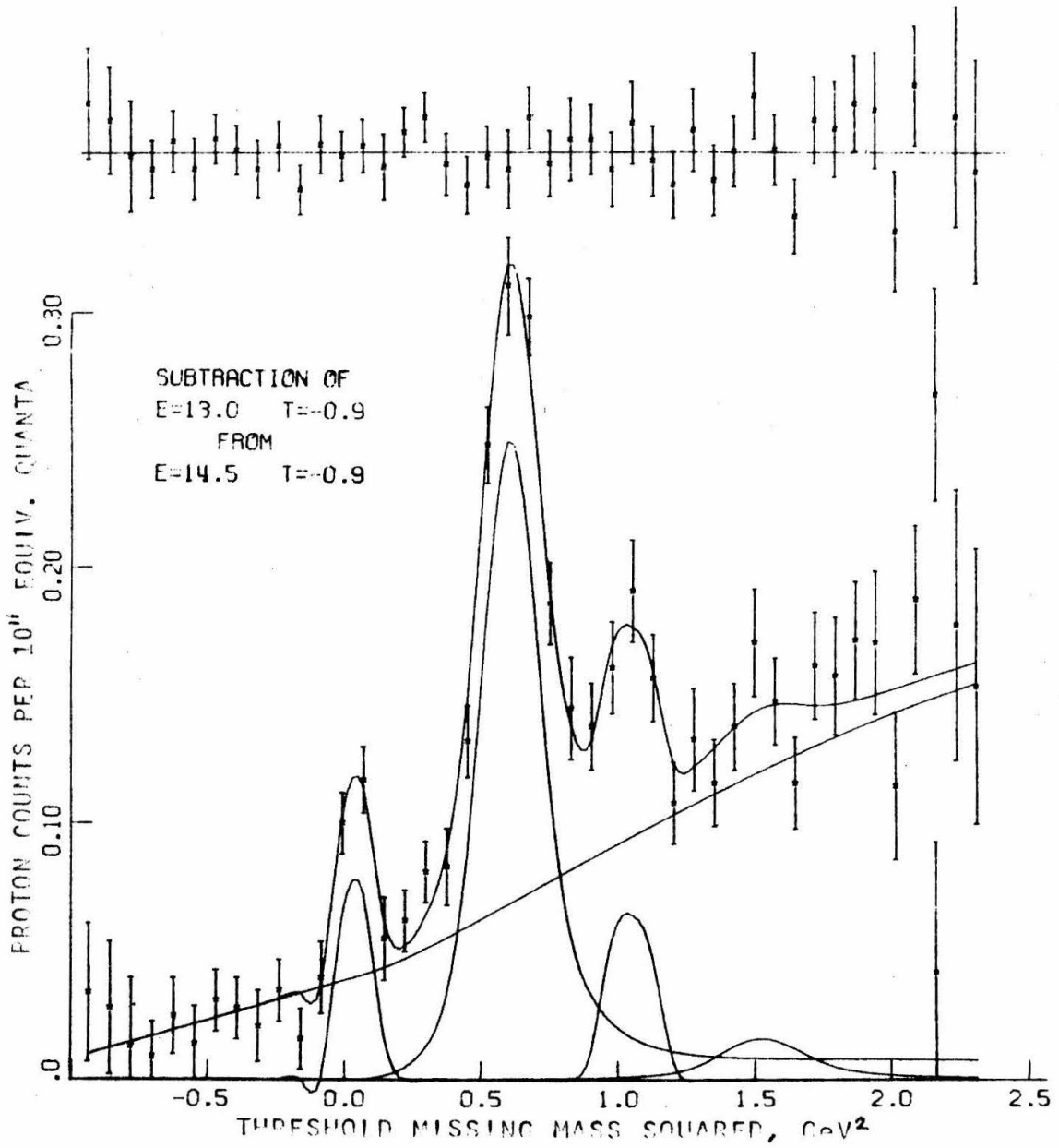


FIGURE 9u

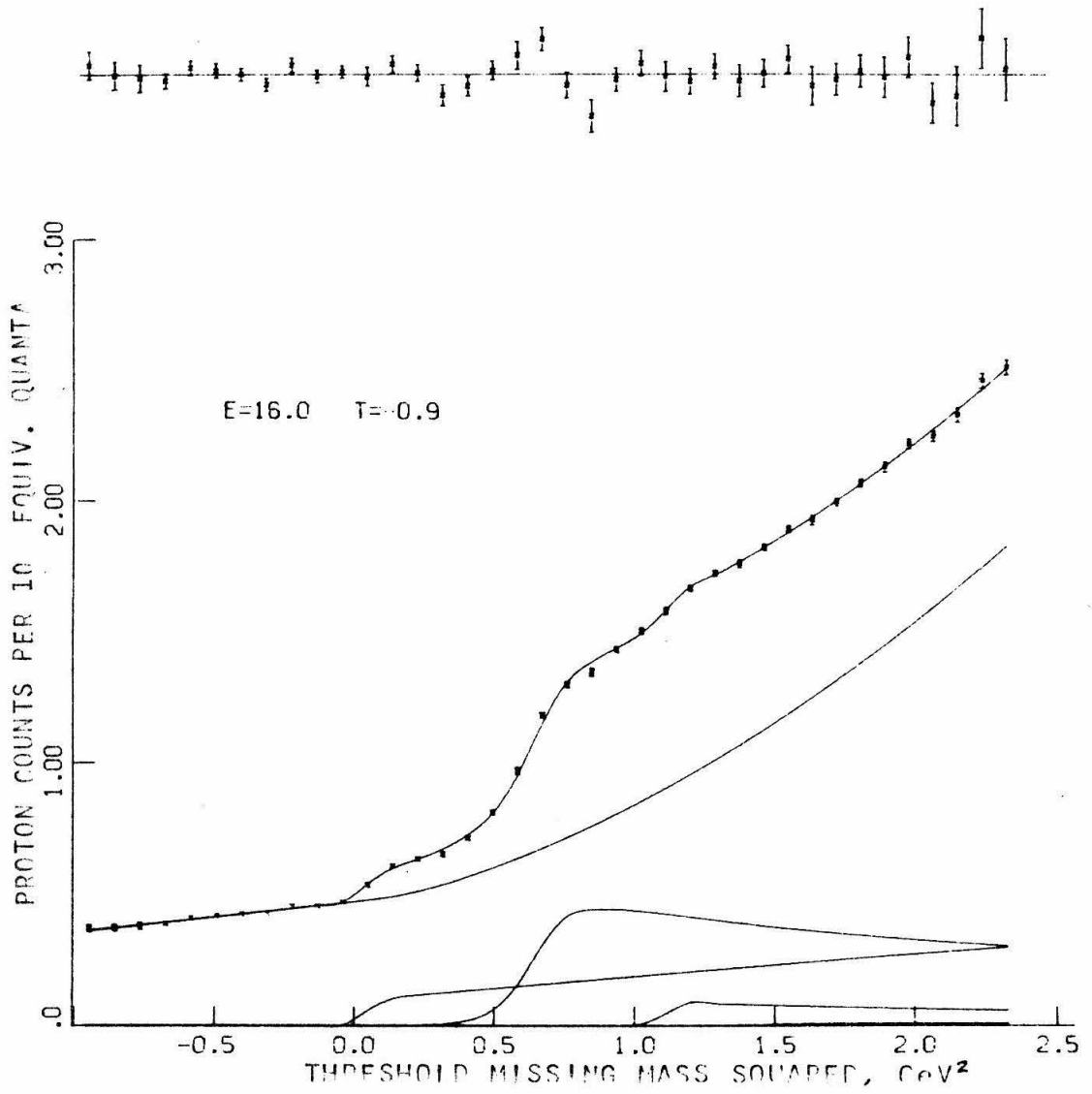


FIGURE 9v

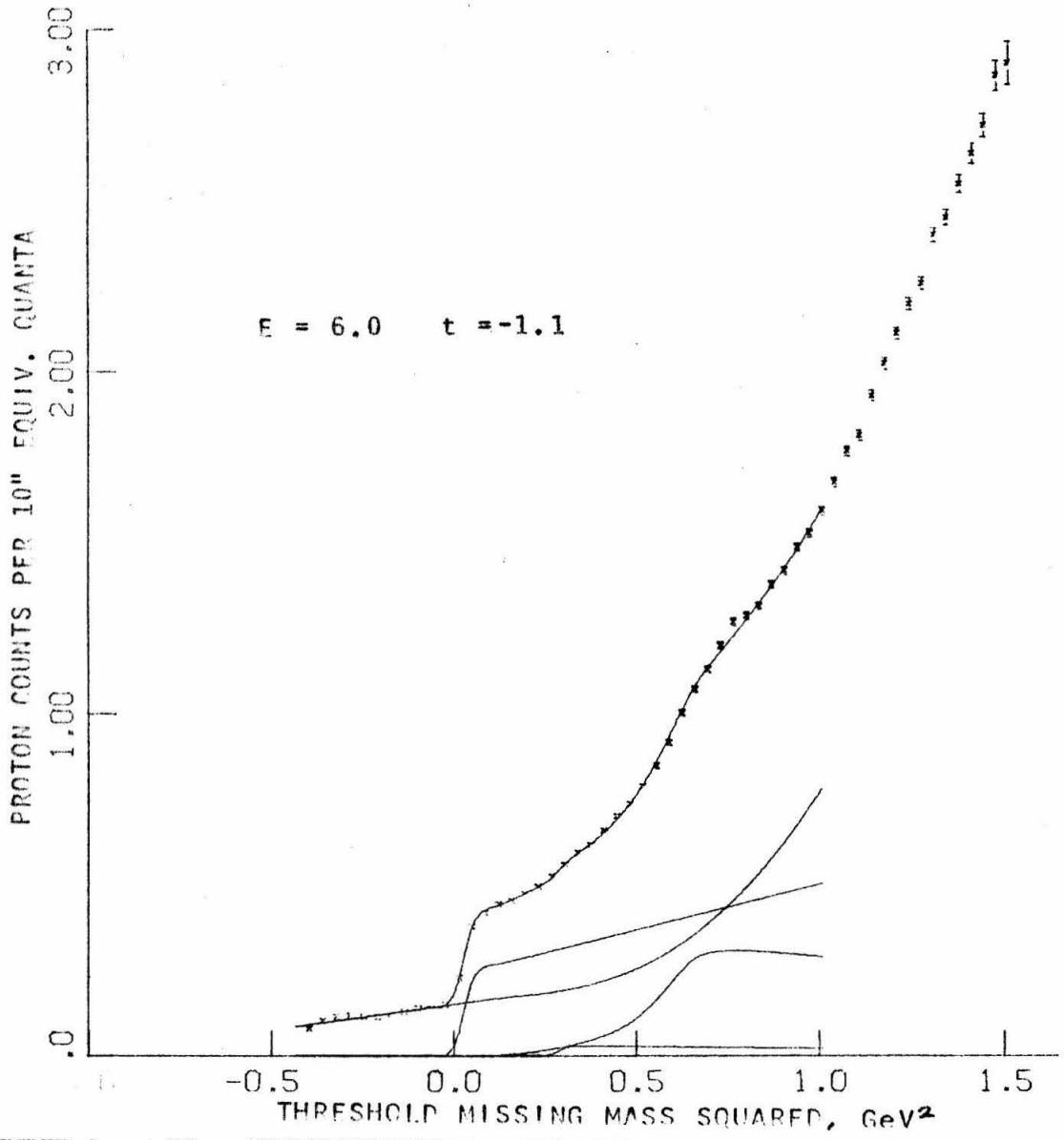


FIGURE 9w

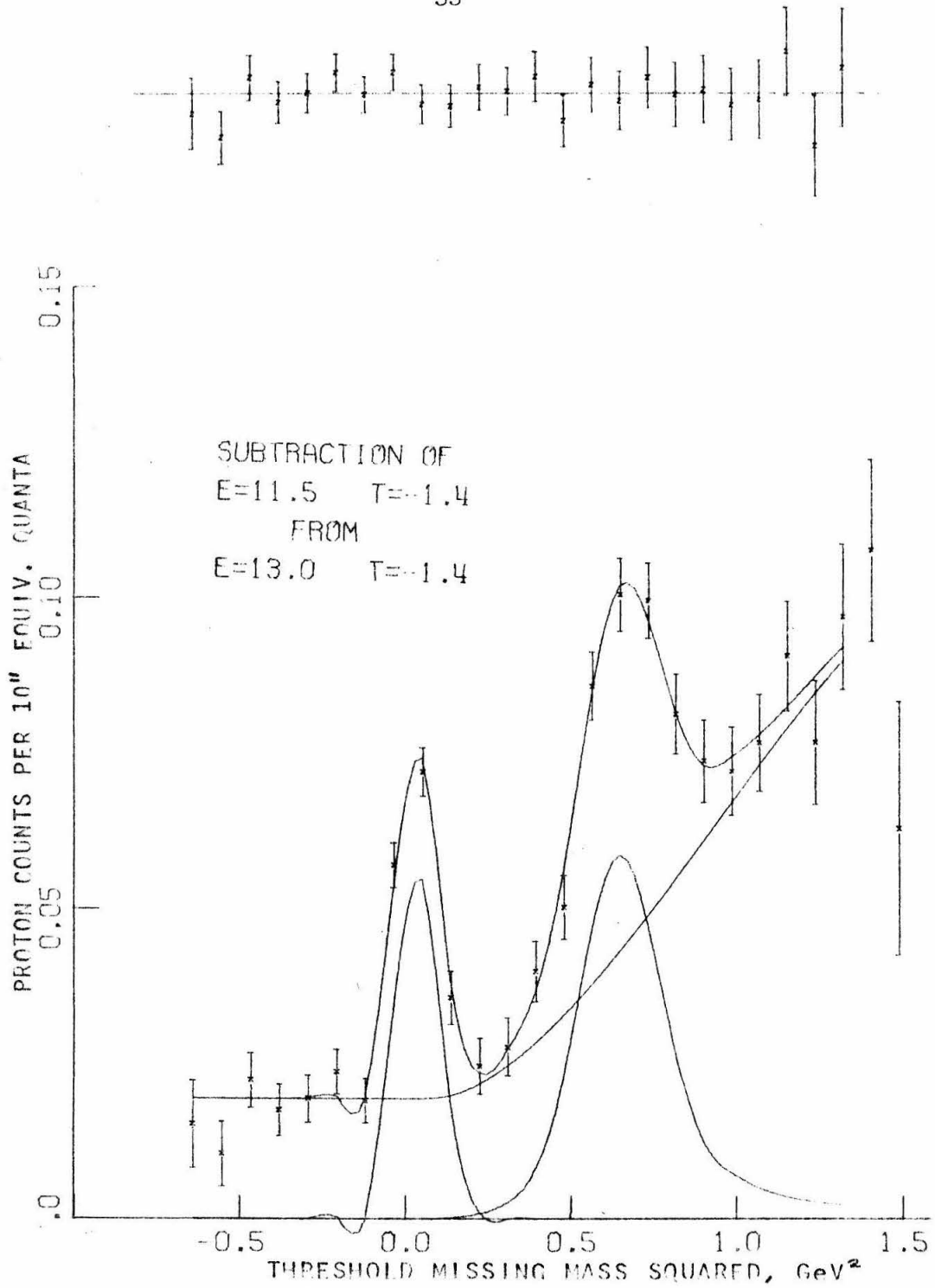


FIGURE 9x

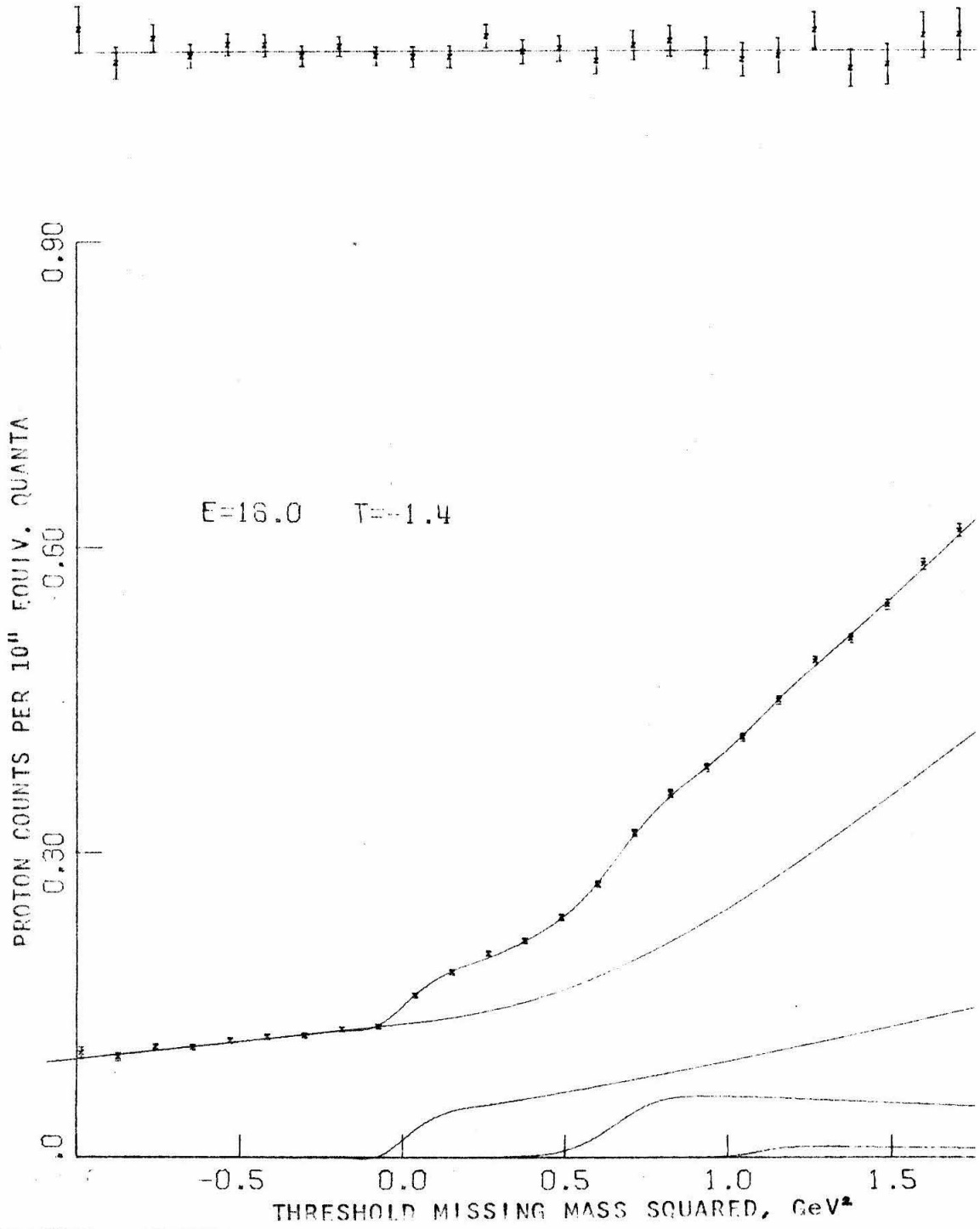


FIGURE 9y

difficult to distinguish the steps of the pion and the phi because they are so badly spread.

The yield from rho production dominates the structure for all but the highest momentum transfers. As momentum transfer increases the pion step becomes more and more pronounced, partly because pion cross sections fall less rapidly with t than the other particles', and partly because angle resolution improves. The eta step is only visible at low energies and intermediate momentum transfers; at high energy the cross section is low, and at low or high momentum transfer mass resolution becomes poor. Phi steps are consistently visible where statistics are good enough. The "B" steps shown are not the most impressive ones seen (cf. chapter V) and have large statistical errors, but are typical.

IV. DATA ANALYSIS

A. Data Consolidation

Each of the 108 angle sweeps at a definite endpoint energy and t consisted of approximately 25 separate runs, one for each spectrometer angle setting. Before the data could be fit these runs had to be organized into composite curves of proton yield vs. angle. Correction had to be made before this was possible.

The eight hodoscope counters have different proton detection efficiencies. These efficiencies change with t because of errors in correcting for differing proton flight times and ionization rates. The relative efficiencies were evaluated for each t by demanding that the partial yield curves obtained by the individual hodoscope counters all had the same normalization. The resulting efficiencies were taken out of the data before consolidation.

Accidental coincidences and dead times in the electronics were evaluated using an empirical formula and experimental data on accidental coincidences. The accidentals monitor was calibrated by comparing data at high and low counting rates. In many cases, the correction was applied run by run.

The stability of the beam monitor was verified using two secondary monitors, the smoothness of the pion yield curve, and redundancies in the proton yield data itself. A run was discarded or its measured photon flux corrected when the tests showed this necessary, roughly 5 percent of the time.

B. Fitting Procedure

The fitting procedure was a straightforward application of the concepts described in chapter III. For each particle a mass, a width, and an energy dependence for the cross section were assumed. From these the theoretical yield of recoil protons vs. angle was calculated for each particle, following equation (III-3). The effect of resolution was simulated. The resulting curve was matched to the data with a linear least squares fitting program to determine a normalization, and hence the cross section. Theoretical curves for fitting subtracted data were generated by subtracting the theoretical curves for the two endpoint energies. Backgrounds were estimated with polynomials.

The form of the function used to fit a yield curve was

$$\begin{aligned}
 Y(\theta) = & \frac{J}{\sin \theta} (a_{\pi} y_{\pi}(\theta) + a_{\eta} y_{\eta}(\theta) + a_{\rho} y_{\rho}(\theta) + \dots) \\
 & + b_0 + b_1(\theta - \theta_0) + b_2(m - 2m_{\pi})^2 + b_4(m - 2m_{\pi})^2 + \dots
 \end{aligned}
 \tag{IV-1}$$

where

J is the Jacobian defined in equation (III-3),

$\sin \theta$ corrects for the effective target length as viewed obliquely,

a_{π}, a_{η}, \dots are the parameters to be determined by fitting, and are related to the cross sections,

y_{π}, y_{η}, \dots are the calculated yield vs. angle curves for each particle,

b_0, b_1, \dots are fitted parameters for representing the background. (The b_2, b_4, \dots terms are zero for m less than two pion masses),

m is the threshold missing mass at angle θ , calculated assuming the photon has the endpoint energy,

and θ_0 is the angle for which m is zero.

The physical assumptions are contained in the form of the background polynomial and in the yield curves $y(\theta)$. Appendix B describes in detail the assumptions made and the rationale behind them. A sketch of the fitting procedure for each particle is presented here.

The eta and phi were fit with the simplest of assumptions. Both particles' cross sections were assumed independent of photon energy. The chief difficulty in obtaining their cross sections was background. The contribution of the eta was masked by poorly known yields from multi-pion production and the low mass tail of the rho distribution. The phi step is on a huge background from rho production.

Obtaining pion cross sections was more complicated. The variation of the cross section with photon energy was determined iteratively. An effective power law behavior was established in preliminary analyses and used for the final analysis. Two sources of confusion made the extraction of cross sections difficult. The photon energy was hard to determine because of a three-way collision between poor angle resolution, rapid variation with angle of the photon energy effective in producing pions, and rapid variation of the cross section with photon energy. The second source of confusion was Compton scattering, which is not resolved from pion

production. Measured total gamma-p cross sections^(5, 24), the optical theorem, and the photon-rho meson analogy were used to estimate

$$\frac{d\sigma}{dt} (\text{Compton}) = .68 \exp(8.5t) \mu\text{barn}/(\text{GeV}/c)^2 .$$

This correction is small for $-t$ greater than $.5 (\text{GeV}/c)^2$, but becomes as large as 50 percent at t of $-.2 (\text{GeV}/c)^2$.

The rho meson presented several serious problems. The proper resonance shape is unknown. This was dealt with by fitting with all currently popular shapes and investigating the sensitivity of derived cross sections to shape. The Jackson-Selleri⁽²⁵⁾ shape was used as standard in quoting cross sections. The rho width and mass have not been convincingly measured, so both were treated as parameters in preliminary fitting. Since no regular dependence on s or t was found, the final fits used the average values of 765 MeV mass and 125 MeV width. The omega, not resolvable from the rho, was estimated to be 10 percent of the rho plus omega cross section. The lack of knowledge about multipion production background was a serious problem since large changes are possible over the large width of the rho. Errors due to possible structure in the background were estimated by eye. Uncertainties from these sources dominate the specified errors in the rho cross sections.

The 1240 MeV particle was fit with a simple Breit-Wigner shape. The broad width and poor statistics were the primary sources of difficulty in determining the cross section.

The analysis of the mass search was very different from fitting for a particle's cross section. Discussion will be deferred to chapter V.

The technique of fitting theoretical functions to the data to determine cross sections has the advantage of objectivity and of being able to account for energy dependence of cross sections and mass resolution correctly. However, its inflexible insistence on the assumed form can be a hindrance if that form is only an approximation. For example, the rho size is determined primarily by the threshold missing mass region near 765 MeV. If the assumed mass distribution is inaccurate on the tails of the rho, the background polynomial will adjust to correct the error. Since the background has only a few degrees of freedom, the adjustment will affect the background everywhere. The entire fit can be ruined.

For this reason all fits were plotted and examined to be sure that the background was physically reasonable and that the fits to each particle were good. Each yield curve was fit several times with differing assumptions. Sometimes particles were fit individually. For the narrow particles, pi, eta and phi, two additional entirely independent methods (described in appendix B) were used to measure cross sections and the results were compared. The use of a variety of rho shapes helped to guarantee that wrong shapes did not ruin the fits.

C. Calculation of Cross Sections

Equation (III-3b) can be inverted to express the cross section in terms of experimental data and kinematic factors:

$$\frac{d\sigma}{dt} = \left\{ \frac{\text{Proton counts} \cdot E_o}{\text{SEQ} \cdot F} \right\} \left[\frac{\sin \theta}{J} \frac{1}{\alpha(k, E_o)} \right] \frac{1}{\eta} \left(\frac{A}{\rho N_o} \right) \frac{1}{L} \frac{1}{\frac{\Delta p}{p} \Delta \Omega} \quad (\text{IV-2})$$

where all symbols have the same meaning as in equation (III-3); in addition SEQ represents the charge accumulated on the SEQ capacitor, and F is a measured factor converting SEQ charge to total energy in the photon beam. The expression in the curly brackets is thus proton counts per equivalent quantum. It is the result of the data consolidation process described in section A of this chapter, and is input data to the fitting program. The kinematic factors in the square brackets are incorporated into the fitting functions as described in section B. The remaining factors account for target length and density, spectrometer acceptance and the various efficiencies. Table 1 lists the values of the parameters used in equation (IV-2).

The efficiency factor η includes the effects listed in table 2. These are described in appendix B.

Adding in quadrature the various estimated errors from tables 1 and 2 we find a total systematic normalization uncertainty of approximately 6 percent. This does not include possible systematic errors in fitting, which have been included in the error bars for each point.

TABLE 1 - Parameters for Computing Cross Section

Parameter	Value	Error	
F	SEQ conversion factor	2.10×10^{12} GeV/ μ coul	$\pm 2\%$
$\alpha(k, E_0)$	bremsstrahlung spectrum	.923 (except for rho)	$\pm 2\%$
ρ	target density	.070 gm/cm ³	$\pm 2\%$
L	target length aperture	6.0 inches	}
$(\frac{\Delta p}{p}) \Delta \Omega$	spectrometer aperture	6.8×10^{-4} steradian	
η^{-1}	typical correction (cf. table 2)	1.196	$\pm 3.5\%$
Estimated normalization error			6%

TABLE 2 - Corrections to the Cross Sections
(All entries are in percent)

$-t(\text{GeV}/c)^2$.12	.2	.3	.4	.5	.7	.9	1.1	1.38	
Correction										
Loss of beam from pair production		3 ± .5	independent of t							
Ionization loss effect on momentum aperture	18.7 ± 1.9	7.5 ± .8	3.3 ± .3	1.9 ± .2	1.4 ± .1	0.7 ± .1	- negligible -			
Absorption loss of protons	9 ± 3	5 ± 1	11 ± 3	9 ± 2	8 ± 2	8 ± 2	8 ± 2	8 ± 3	8 ± 3	
Hodoscope counter inefficiency	3 ± 1	5 ± 2	5 ± 2	5 ± 2	5 ± 2	5 ± 2	5 ± 2	5 ± 2	5 ± 2	
Cerenkov vetoes proton	-	1 ± .5	1 ± .5	1 ± .5	1 ± .5	1 ± .5	1.5 ± .5	2.8 ± 1.0	5.8 ± 1.5	
Rate dependence	Varies between 0 and 5, uncertainty ± 2									
TOTAL	36.3 ± 4.2	23.3 ± 3.2	25.2 ± 4.2	21 ± 3.5	19.6 ± 3.5	18.8 ± 3.5	18.6 ± 3.5	20.0 ± 4.3	23.6 ± 4.4	

V. RESULTS AND DISCUSSION

A. Pion

Differential cross sections obtained for pion photoproduction are plotted in figure 10. DESY data at photon energies below 6 GeV are also plotted. Our error bars include counting statistics and an estimate of background uncertainty. At low momentum transfers, poor resolution and large Compton scattering corrections contribute large systematic uncertainties. Corrections have been made which are peculiar to the pion data. The derivation of effective photon energy from endpoint energy and the angle resolution is described in appendix B. Estimates of the Compton effect cross sections use the measured total photon-proton cross section and the photon-rho meson analogy as described in appendix B.

The data are plotted versus $(s - M^2)$, where s is the square of the total energy in the center of mass, and M is the mass of a proton. Full logarithmic axes show the power law dependence of the cross section. The straight lines are least squares fits with the fitting function*

$$\frac{d\sigma}{dt} = A (s - M^2)^{2\alpha(t) - 2} .$$

* The Regge behavior of cross sections with s is often written $A(s/s_0)^{2\alpha-2}$, with s_0 customarily taken as 1 GeV. Using $(s - M^2)$ guarantees the cross section vanishes at threshold, and therefore may be a better form to use at low energy. The trajectory derived using s instead of $(s - M^2)$ is almost indistinguishable, if only photon energies above 5 GeV are involved.

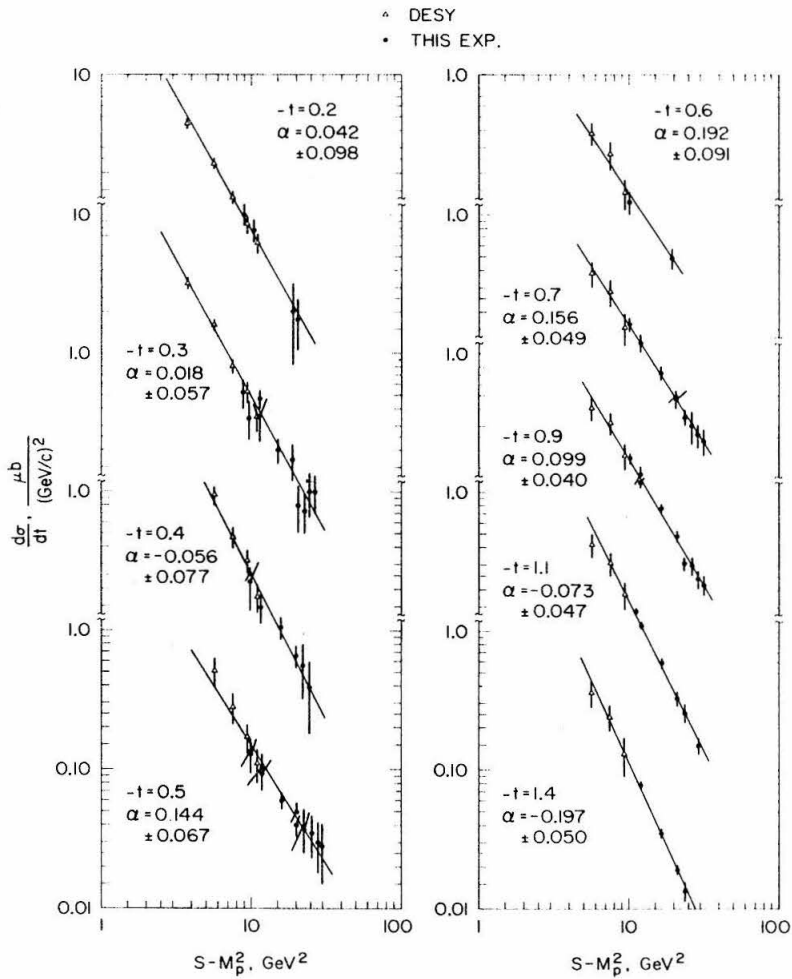


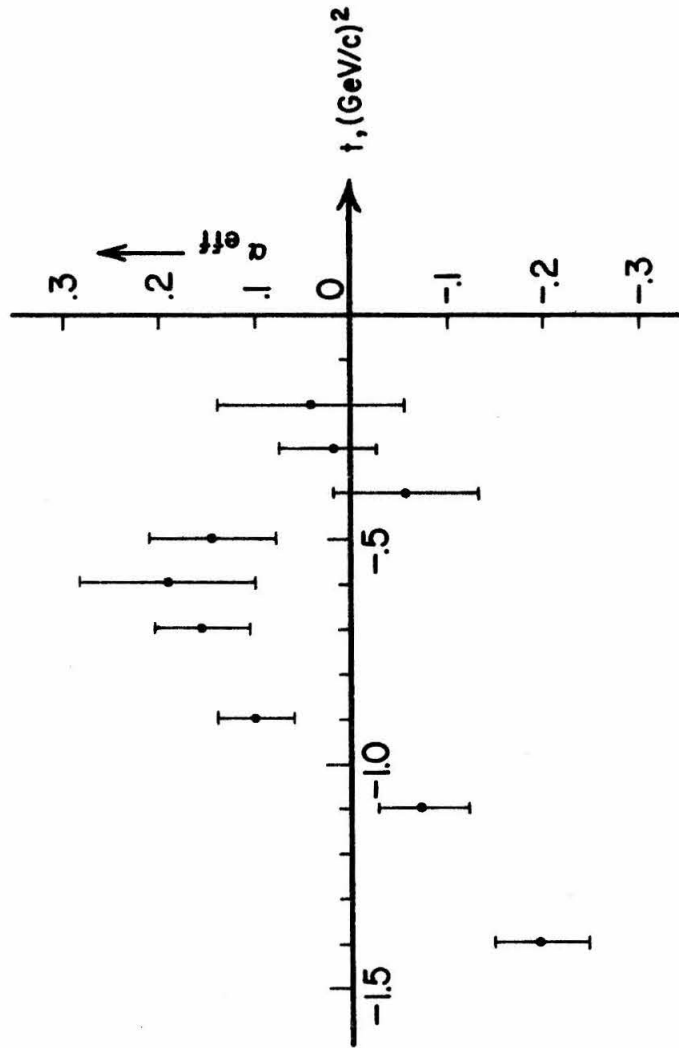
FIGURE 10 Pion Cross Section vs. $s - M^2$

The DESY data were included in this fit. The effective Regge trajectory $\alpha(t)$ is plotted versus t in figure 11.

Because the data are taken at varying effective s , plotting cross section against t for various photon energies requires interpolation. This was done assuming a power law dependence of cross section on photon energy. The results are plotted in figure 12 for photon energies of 6, 9, 12, and 15 GeV. At low momentum transfer, the cross section drops rapidly, approximately as $\exp(6t)$. The outstanding feature of the curves is the "dip" at a t of $-.5 (\text{GeV}/c)^2$ which is pronounced at 6 GeV photon energy, but becomes only a shoulder at higher energies. Above the dip region the data again show smooth exponential decreases. Figure 13 shows the 6 GeV data from this experiment plotted along with the DESY results at 5.8 and 5.0 GeV. The cross sections are multiplied by a factor of s^2 which takes out most of the energy dependence and makes comparison easier. The results of the two experiments are completely consistent. In both figures 12 and 13 the dotted lines are merely to guide the eye.

Because the disappearance of the dip at high energies runs counter to the prior expectations of simple Regge theory, it is important to estimate the strength of the evidence. Within the model taken for the background, the quoted errors are very conservative. The background was assumed to be a straight line below the threshold for producing two pions, and a polynomial above. Attempts were made to estimate sensitivity to the model by increasing the order of polynomial below threshold. The results were erratic, indicating overparametrization, but averaged about 20 percent lower. Pion curves have also all been fit by eye and with a second computerized method described in appendix B. Errors quoted include estimates

FIGURE 11 Pion Production Effective Regge Trajectory



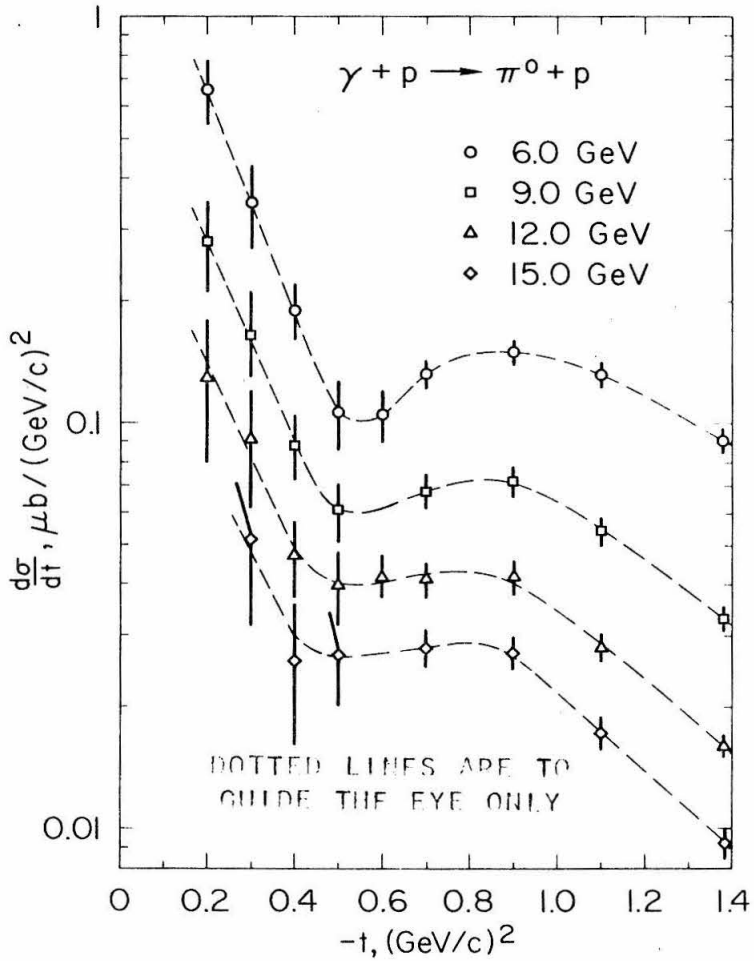
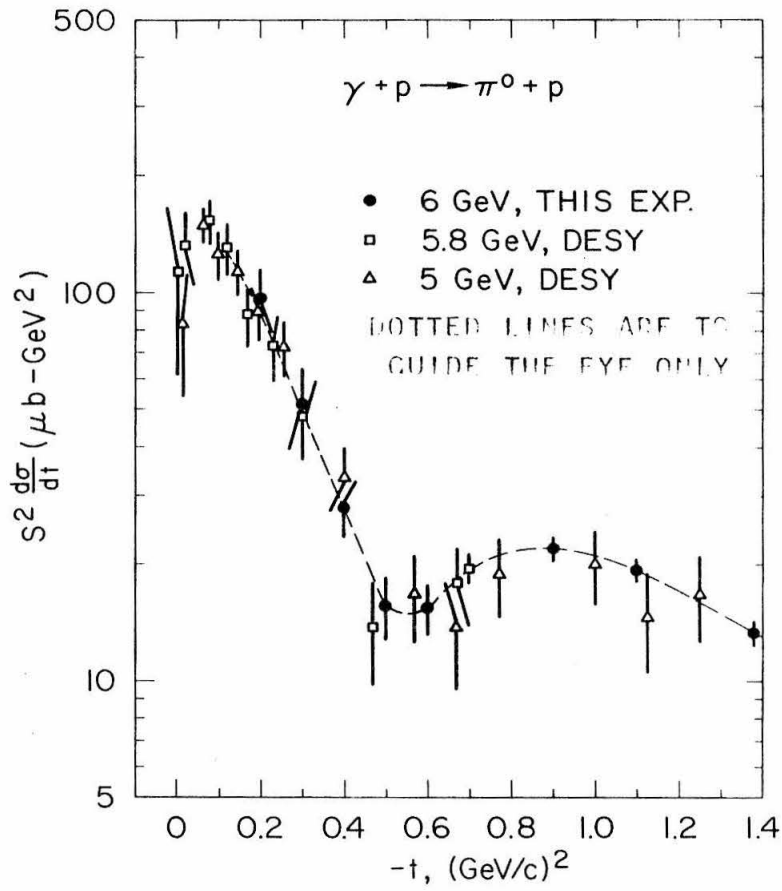


FIGURE 12 Pion Cross Section vs. t

FIGURE 13 Pion Cross Section vs. t

of systematic fitting uncertainties based, in part, on a comparison of results from all these models. The disappearance of the dip is therefore probably real. However, a more definitive experiment is needed. Such an experiment has been proposed⁽²¹⁾ and will be run soon.

If the dip really does go away, the Regge theory explanation of neutral pion photoproduction must be modified. A theory quite successful in explaining the data^(1, 2) at the time this experiment was begun used Regge single particle exchange^(4, 3). Conservation laws allow only omega, rho, phi, and B single-trajectory exchanges. $\rho\pi\gamma$ and $\phi\pi\gamma$ couplings are small, so omega can be taken to represent the vector mesons. The omega trajectory contribution should dominate the cross section. The dip is supposed to be produced where the omega trajectory passes through zero and its contribution vanishes. The residual cross section in the dip region is attributed to sources which are negligible elsewhere -- the B meson exchange contribution in the Ader, Capdeville and Salin theory⁽⁴⁾. These contributions should decrease faster with increasing s than the omega contribution, so the dip should become deeper as energy increases.

Other evidence than the vanishing of the dip casts doubt on the simple omega exchange model. The energy dependence of the differential cross section outside the dip region also disagrees with predictions of omega trajectory exchange, as can be seen from the effective Regge trajectory in figure 11. Furthermore, as Harari⁽²⁶⁾ shows using the vector dominance model and experimental limits on $\pi^+ + n \rightarrow \omega + p$, the B trajectory exchange contribution is too small by at least a factor of four to fill in the dip. Finally, measurements

at CEA of neutral pion photoproduction with polarized 3 GeV photons⁽²⁷⁾ show a polarization of the wrong sign for B exchange in the dip region.

In the face of this evidence, several new theories have appeared, all of which allow cuts or absorption as well as single Regge pole exchanges. J. Frøylund⁽²⁸⁾ and A. Capella and J. Tran Thanh Van⁽²⁹⁾ each use omega exchange and a cut term from omega and Pomeranchuk exchange. Both ignore the contribution of the B. The dip from the vanishing of the omega trajectory contribution is filled in by the contribution from the cut term, which becomes increasingly important with increasing energy. Each of the two theories achieves a good fit to our data and the polarization data. The theory of Blackmon, Kramer, and Schilling⁽³⁰⁾ uses rho, omega and B exchange with absorption to obtain a good fit to our published data and a fair fit to the polarization data. Some B exchange is required, and the B trajectory has an unusually high intercept and small slope. Furthermore, the model predicts a pronounced peaking at low momentum transfers for high energies. Even though our data in this region are too poor to have been published, the anticipated factor of three enhancement should have been qualitatively visible and was not.

A different type of theory⁽³¹⁾ uses vector dominance* to relate pion $\gamma_{\rho}^2/4\pi$ photoproduction to production of vector mesons by pions, without going into the workings of the reaction as does the Regge theory. The prediction using $\gamma_{\rho}^2/4\pi = .5$ is consistent with the data, although the uncertainties in the data on vector meson production by pions are rather large.

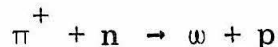
* The vector dominance model will be discussed in connection with rho meson photoproduction.

B. Eta

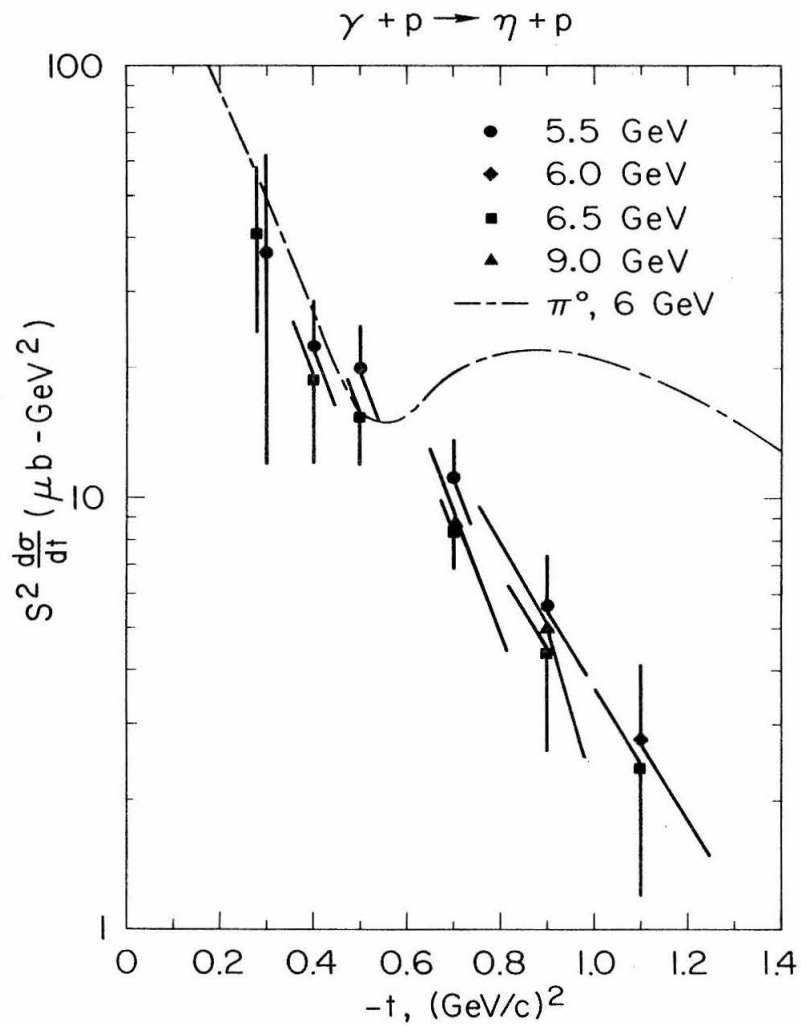
Differential cross sections for eta photoproduction are plotted in figure 14 as $s^2 \frac{d\sigma}{dt}$ vs. t . Reliable data are only obtained at 5.5, 6.0, 6.5 and 9.0 GeV because of background problems. The dotted line of figure 14 is the 6 GeV pion production cross section taken from figure 12. It shows that eta cross sections are of the same order of magnitude as pion cross sections, but lack the dramatic dip. For the small range of energies and momentum transfers covered, the differential cross section is consistent with an s^{-2} energy dependence and an $\exp(3t)$ dependence on momentum transfer.

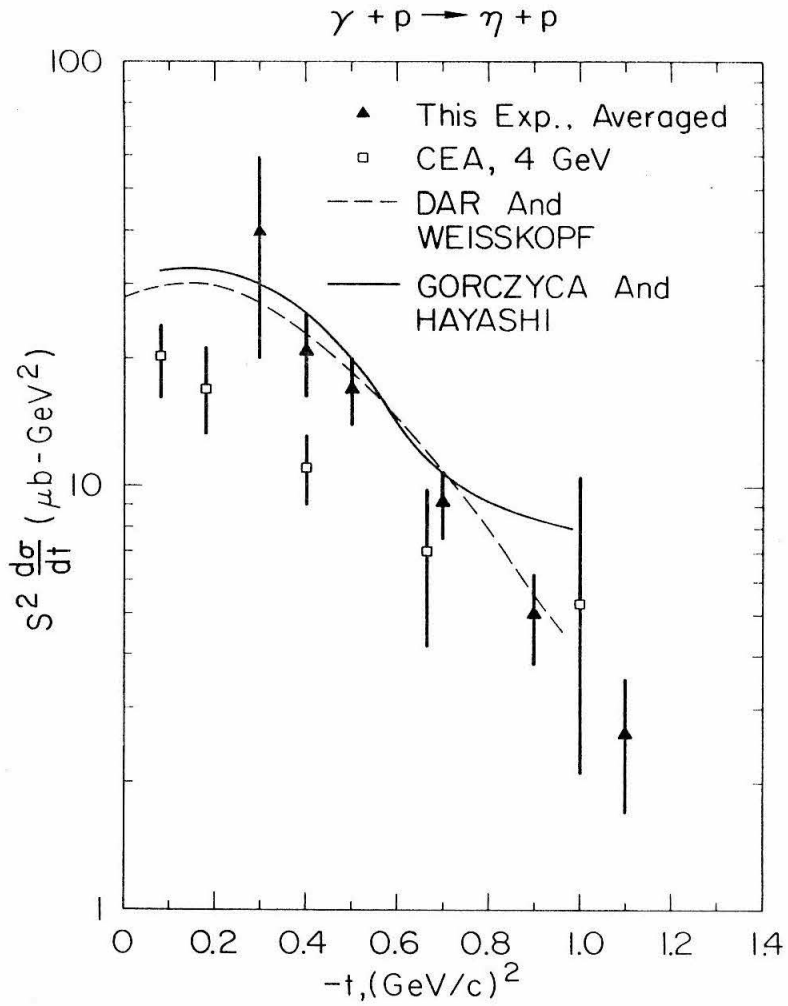
In figure 15 the eta production data of this experiment are compared with 4 GeV measurements by Bellenger *et al.* at CEA⁽⁷⁾. In the CEA experiment the eta decay into two photons was measured by observing the decay photons. As in figure 14, s^2 times the differential cross section is plotted to take out the s dependence for comparison. Our data appear to fall more rapidly with t , and also seem somewhat higher. This may reflect a genuine change in t -dependence with energy and a fall off with energy slower than s^{-2} , but the conclusion is not firm considering the errors and the two very different techniques.

Figure 15 also depicts two fits to the data made using vector dominance and SU_3 . Dar and Weisskopf⁽⁸⁾ assume rho exchange dominance to relate eta photoproduction to the process



and also to the process $\pi^- + p \rightarrow \omega + n$.

**FIGURE 14** Eta Cross Section vs. t

**FIGURE 15** Eta Cross Section vs. t

Gorczyca and Hayashi⁽³²⁾ allow omega and B exchange as well as rho exchange and relate eta photoproduction to neutral pion photoproduction and vector meson production by pions. Both fits agree reasonably well with the data. Although ideally neither fit has any parameters, the poorly known coupling constant $\gamma_{\omega\gamma}$ allows a certain freedom.

One might expect simple Regge theory⁽⁹⁾ to predict a dip in the eta photoproduction cross section, analogous to the dip in pion photoproduction, due to the vanishing of the contribution of the rho trajectory. The absence of a dip can be reconciled with Regge theory. It is possible for B exchange to fill dips in eta photoproduction but not in pion photoproduction if amplitudes interfere in just the right way. However, such a theory does not seem to have much predictive value. A recent theory by F. Henyey et al.⁽³³⁾ explains dips as interference between a Regge pole exchange amplitude and the amplitudes of its associated absorptive cuts. The authors expect to be able to reproduce the pion photoproduction data without using B exchange. They also appear to be able to fit the reaction $\pi^+ + n \rightarrow \omega + p$ ⁽³⁴⁾, which is closely related to eta photoproduction as noted in the previous paragraph. However, the absence of a dip in their model appears to be due to a post hoc assumption about the absence of nonsense wrong-signature zeroes. A theory which required the presence of a dip in pion photoproduction and the absence of a dip in eta photoproduction would be more satisfying.

C. Rho

Rho meson photoproduction differential cross sections are listed in table 3. These numbers were obtained assuming a Jackson-

TABLE 3 RHO PRODUCTION DIFFERENTIAL CROSS SECTION

-T		ENERGY*		CROSS SECTION		-T		ENERGY*		CROSS SECTION	
(GEV/C) ²	GEV	(GEV/C) ²	GEV	NANOBNRN/(GEV/C) ²		(GEV/C) ²	GEV	NANOBNRN/(GEV/C) ²		(GEV/C) ²	GEV
0.12	5.75 S	0.12	5.50 Y	40000. +- 8000.		0.40	5.50 Y	9300. +- 1700.		0.40	16.00 Y
0.12	6.25 S	0.12	6.50 Y	40000. +- 7000.		0.40	6.50 Y	5100. +- 900.		0.40	16.90 S
0.12	14.50 Y	0.40	11.50 Y	37000. +- 5000.		0.40	11.50 Y	4800. +- 700.		0.40	17.80 Y
0.12	15.25 S	0.40	12.25 S	35000. +- 7000.		0.40	12.25 S	4300. +- 600.			
0.12	16.00 Y	0.40	13.00 Y	32000. +- 5000.		0.40	13.00 Y	4500. +- 700.			
0.12	16.90 S	0.40	13.75 S	38000. +- 7000.		0.40	13.75 S	4200. +- 350.			
0.12	17.80 Y	0.40	14.50 Y	35000. +- 5000.		0.40	14.50 Y	4000. +- 600.			
		0.40	16.00 Y			0.40	16.00 Y	4400. +- 600.			
0.20	6.00 S	0.40	16.90 S	26000. +- 3500.		0.40	16.90 S	4100. +- 500.			
0.20	6.50 Y	0.40	17.80 Y	27000. +- 5000.				4100. +- 600.			
0.20	11.50 Y	0.50	5.50 Y	22000. +- 3500.				3500. +- 500.			
0.20	13.00 Y	0.50	6.00 S	16500. +- 3500.				3400. +- 400.			
0.20	13.75 S	0.50	6.50 Y	16500. +- 3500.				2500. +- 530.			
0.20	14.50 Y	0.50	7.75 S	15000. +- 3000.				2800. +- 710.			
0.20	16.00 Y	0.50	9.00 Y	16000. +- 3500.				3000. +- 360.			
0.20	16.90 S	0.50	11.50 Y	24000. +- 5000.				2200. +- 290.			
0.20	17.80 Y	0.50	12.25 S	18000. +- 3500.				2200. +- 320.			
0.20	17.80 Y	0.50	13.00 Y	18000. +- 3000.				2240. +- 290.			
		0.50	13.00 Y					2100. +- 300.			
0.30	5.00 Y	0.50	13.75 S	18000. +- 5000.				2200. +- 350.			
0.30	5.25 S	0.50	14.50 Y	9500. +- 4000.				2100. +- 290.			
0.30	5.50 Y	0.50	15.25 S	14000. +- 4000.				2300. +- 290.			
0.30	6.50 Y	0.50	16.00 Y	11000. +- 2500.				2050. +- 230.			
0.30	11.50 Y	0.50	16.90 S	8300. +- 1800.				2000. +- 290.			
0.30	12.25 S	0.50	17.80 Y	9200. +- 1300.				1960. +- 290.			
0.30	13.00 Y			7600. +- 1200.							
0.30	13.75 S			8200. +- 1200.							
0.30	14.50 Y			7300. +- 1200.							
0.30	16.00 Y			8900. +- 1800.							
0.30	16.90 S			9300. +- 1800.							
0.30	17.80 Y			8300. +- 1200.							

* Y IDENTIFIES DATA TAKEN FROM YIELD CURVE AT THE SPECIFIED ENDPOINT ENERGY.
S IDENTIFIES DATA TAKEN FROM SUBTRACTION AT THE SPECIFIED AVERAGE ENERGY.

TABLE 3 RHO PRODUCTION DIFFERENTIAL CROSS SECTION (CONTINUED)

-T (GEV/C) ²	ENERGY* GEV	CROSS SECTION NANOBN/((GEV/C) ²)	-T (GEV/C) ²	ENERGY* GEV	CROSS SECTION NANOBN/((GEV/C) ²)
0.70	5.50	810. +- 160.	1.10	6.00	260. +- 48.
0.70	6.00	1080. +- 230.	1.10	6.25	210. +- 59.
0.70	6.50	900. +- 140.	1.10	6.50	170. +- 89.
0.70	7.75	880. +- 230.	1.10	7.75	130. +- 42.
0.70	9.00	840. +- 180.	1.10	9.00	110. +- 14.
0.70	10.25	750. +- 180.	1.10	10.25	100. +- 29.
0.70	11.50	660. +- 70.	1.10	11.50	108. +- 14.
0.70	11.50	700. +- 180.	1.10	12.25	114. +- 24.
0.70	12.25	670. +- 80.	1.10	13.00	103. +- 17.
0.70	13.00	670. +- 90.	1.10	14.50	90. +- 16.
0.70	13.75	620. +- 70.	1.10	16.00	89. +- 12.
0.70	14.50	590. +- 80.			
0.70	15.25	590. +- 70.	1.40	9.00	29. +- 12.
0.70	16.00	570. +- 70.	1.40	10.25	31. +- 15.
0.70	16.90	550. +- 70.	1.40	11.50	36. +- 12.
0.70	17.80	540. +- 60.	1.40	12.25	32. +- 11.
			1.40	13.00	33. +- 10.
			1.40	14.50	23. +- 9.
			1.40	16.00	22. +- 8.
0.90	5.50	350. +- 150.			
0.90	6.00	390. +- 60.			
0.90	6.50	410. +- 80.			
0.90	6.50	500. +- 70.			
0.90	7.75	340. +- 50.			
0.90	9.00	340. +- 60.			
0.90	11.50	240. +- 34.			
0.90	12.25	250. +- 28.			
0.90	13.00	190. +- 23.			
0.90	13.75	200. +- 28.			
0.90	14.50	230. +- 23.			
0.90	15.25	230. +- 28.			
0.90	16.00	210. +- 23.			
0.90	16.90	210. +- 28.			
0.90	17.80	190. +- 23.			

* Y IDENTIFIES DATA TAKEN FROM YIELD CURVE AT THE SPECIFIED ENDPOINT ENERGY.
S IDENTIFIES DATA TAKEN FROM SUBTRACTION AT THE SPECIFIED AVERAGE ENERGY.

Selleri type shape for the rho (equation B-5) with a 10 percent admixture of omega. Average values of rho mass and width were obtained by fitting each yield curve. These average values, 765 ± 20 MeV mass and 125 ± 20 MeV width, were adopted as standard for fitting all data. Errors cited in table 3 include statistical errors and estimates of the error due to the unknown shape and width of the rho, background uncertainty, and omega admixture. The assumptions made in fitting are discussed in appendix B.

In figure 16 the differential cross section is plotted against t for various photon energies. The smooth curves are from a fit using the quark model and vector dominance which will be discussed shortly. The data are also well represented by a function of the form

$$\frac{d\sigma}{dt} = A \exp(Bt + Ct^2) \quad (V-1)$$

with A about $100 \mu\text{barn}/(\text{GeV}/c)^2$, B about $8.5 (\text{GeV}/c)^{-2}$, and C about $2 (\text{GeV}/c)^{-4}$. The B and C values are very similar to those obtained in fitting pion-proton elastic scattering⁽³⁵⁾. Attempts to fit the data without the C term are successful up to $t = -.6 (\text{GeV}/c)^2$, although they fail badly over the full range of momentum transfers. The discrepancy at high momentum transfers is approximately exponential, i.e., a sum of exponentials

$$\frac{d\sigma}{dt} = A \exp(Bt) + A' \exp(B't) \quad (V-2)$$

with A about $100 \mu\text{barn}/(\text{GeV}/c)^2$, B about $8 (\text{GeV}/c)^{-2}$, A' about $1.5 \mu\text{barn}/(\text{GeV}/c)^2$, and B' about $2.5 (\text{GeV}/c)^{-2}$ also fits the data. The data are not of sufficient quality and do not extend to large enough momentum transfers for one of the forms (V-1) and (V-2) to be preferred.

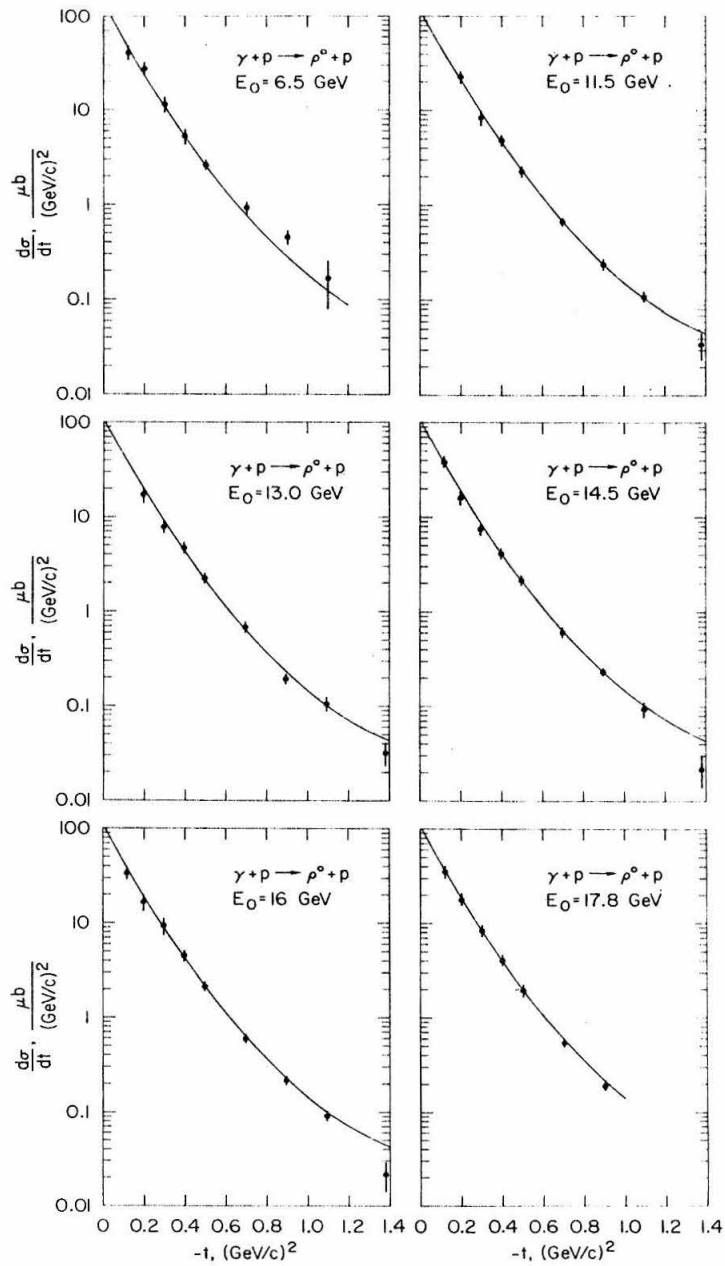


FIGURE 16 Rho Cross Section vs. t

In figure 17 our cross sections for photon energies between 5.5 and 6.5 GeV are compared to a fit of the DESY data⁽⁵⁾ at nearby energies and the data of McClellan et al.⁽¹³⁾ at 6 GeV. The dashed lines about the DESY fit indicate the size of their errors. Cross sections from the three experiments are consistent.

The quark model fits have been used to extrapolate rho differential cross sections to zero momentum transfer and to obtain the total rho cross section as a function of photon energy. The results are listed in table 4. McClellan et al.⁽¹³⁾ obtain forward cross sections with a much smaller extrapolation. Their value is $130 \mu\text{barn}/(\text{GeV}/c)^2$ for the forward differential cross section, approximately constant with photon energy between 4 and 9 GeV. Our results are consistent with this value, but show a greater tendency to fall with energy, from about $140 \mu\text{barn}/(\text{GeV}/c)^2$ at 6 GeV to about $100 \mu\text{barn}/(\text{GeV}/c)^2$ at 17 GeV.

Figure 18 shows the rho differential cross section at various t plotted against s on full logarithmic scales. The dashed straight lines drawn through the data are best fits with the function

$$\frac{d\sigma}{dt} = C (s - M^2)^{2\alpha(t) - 2} . \quad (\text{V-3})$$

The values of α obtained are shown as a function of t in figure 19. For $t = -.4$ and $-1.1 (\text{GeV}/c)^2$ the lowest energy data lie far away from the general trend of the other data. The dotted lines in figure 18 and the dashed points in figure 19 show the best fit ignoring these points. A straight line fit to $\alpha(t)$ gives

$$\alpha_{\text{eff}}(t) = (.89 \pm .04) + (.23 \pm .07)t . \quad (\text{V-4})$$

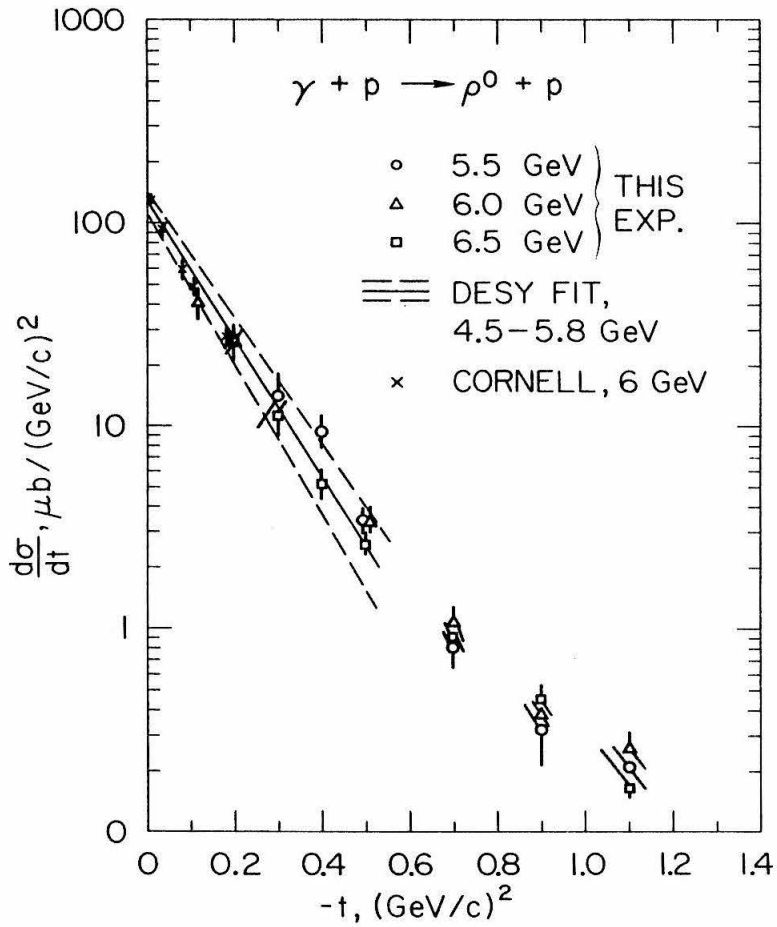


FIGURE 17 Rho Cross Section vs. t

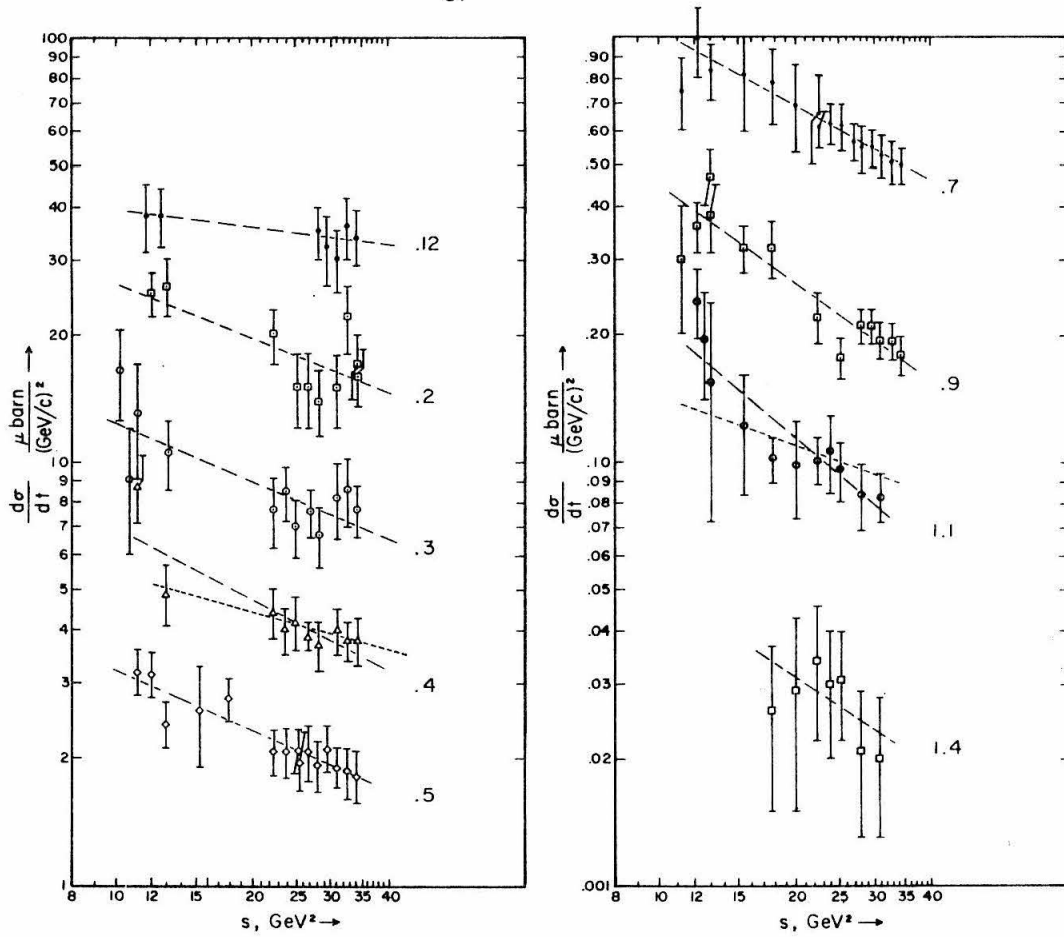
$$\frac{d\sigma}{dt}(\gamma+p \rightarrow \rho+p) \text{ vs. } s$$


FIGURE 18 Rho Cross Section vs. s

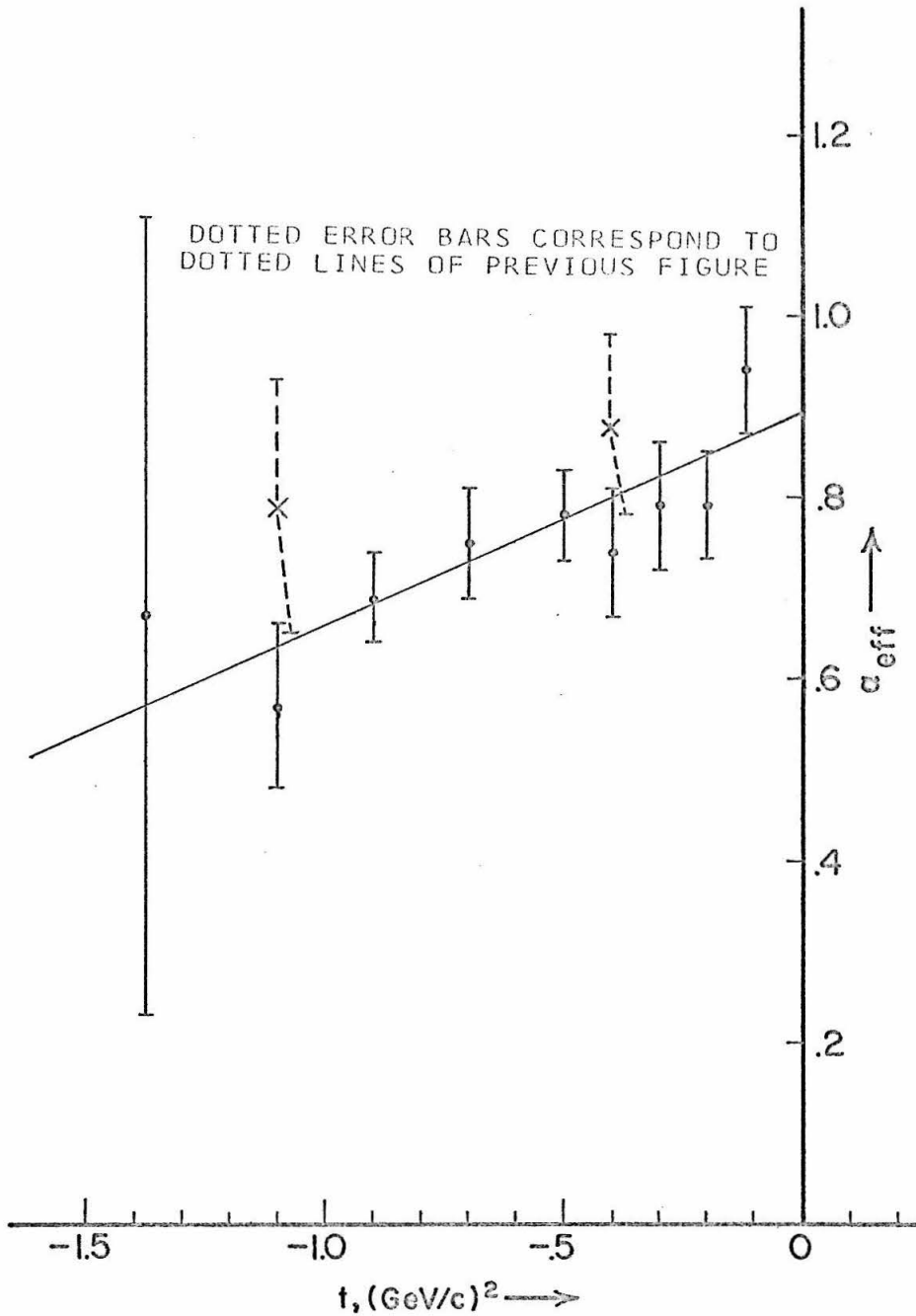


FIGURE 19 Rho Production Effective Regge Trajectory

TABLE 4 RHO PRODUCTION FORWARD AND TOTAL CROSS SECTIONS

E. GEV	$\frac{\gamma_\rho^2}{4\pi} = .61$		γ_ρ FREE PARAMETER	
	$\frac{d\sigma}{dt} _{t=0}$	σ_{TOT}	$\frac{d\sigma}{dt} _{t=0}$	σ_{TOT}
5.50	136.	16.1	167.	19.8
6.00	133.	15.8	152.	18.0
6.50	131.	15.5	138.	16.3
11.50	113.	13.4	113.	13.4
12.25	112.	23.2	111.	13.2
13.00	110.	13.0	109.	12.9
13.75	109.	12.9	110.	13.0
14.50	108.	12.7	101.	12.0
15.25	107.	12.7	107.	12.5
16.00	106.	12.6	103.	12.2
16.90	105.	12.5	105.	12.5
17.80	105.	12.4	101.	11.9

FORWARD CROSS SECTIONS ARE IN UBARN PER (GEV/C)² AND TOTAL CROSS SECTIONS ARE IN UBARN. CROSS SECTIONS ARE OBTAINED BY EXTRAPOLATING WITH EQUATIONS V-5 AND V-6. STATISTICAL ERRORS ARE ABOUT 11 PERCENT FOR ENERGIES BELOW 10 GEV, AND ABOUT 6 PERCENT AT HIGHER ENERGIES. THEY ARE THUS DOMINATED BY SYSTEMATIC NORMALIZATION UNCERTAINTIES OF 15 TO 20 PERCENT.

This effective Regge trajectory is very similar to those obtained in elastic pp , $\bar{p}p$, πp and Kp scattering⁽³⁵⁾, and in particular is nearly identical to the average of the effective trajectories for $\pi^+ p$ and $\pi^- p$ elastic scattering. It is also consistent with the trajectory for the Pomeron obtained by Rarita et al.⁽³⁶⁾ in a fit to hadron elastic scatterings.

The vector meson dominance model (VDM) appears to be helpful in understanding many of the qualitative features of rho photo-production. According to this hypothesis, the photon interaction with hadrons is mediated by the vector mesons, to which the photon couples with amplitudes $\frac{e}{2} \frac{m_V^2}{\gamma_V}$ (15). In this expression, V is rho, omega or phi, m_V is the vector meson mass, and γ_V is the coupling constant. The constants γ_V enter into many processes, including vector meson decay into electron-positron pairs, neutral pion decay into two photons, Compton scattering, and, as mentioned earlier in this chapter, pion and eta photoproduction.

Figure 20 shows how the VDM would view rho meson photo-production. Once VDM is applied, the problem reduces to a problem in strong interactions: $V + p \rightarrow \rho + p$. A well known feature of meson-baryon scattering is that elastic (or "quasi-elastic") total cross sections appear to approach a constant at high energies, whereas reactions requiring the exchange of non-vacuum quantum numbers have cross sections which apparently fall to zero at infinite energies. In Regge language, the Pomeron trajectory is the highest lying known trajectory for physical t . For this reason rho elastic scattering should be larger than rho production by phi or omega mesons at the energies of this experiment, and the V of figure 20 is assumed to be a rho. Using this and evaluating the propagator for the virtual rho meson, we obtain

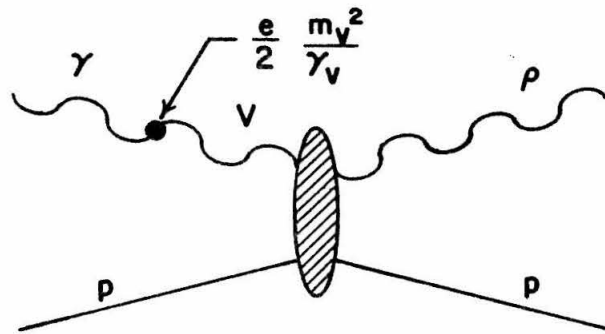


FIGURE 20 Feynman Graph for Rho Photoproduction

$$\frac{d\sigma}{dt}(\gamma + p \rightarrow \rho + p) = \frac{\alpha}{4} \left(\frac{4\pi}{2} \right) \frac{d\sigma}{dt}(\rho_{tr} + p \rightarrow \rho + p) \quad (V-5)$$

where ρ_{tr} indicates that only transversely polarized rhos are considered since photons are transversely polarized.

Margolis⁽¹⁶⁾ uses a simple additive quark model to relate the experimentally unmeasurable rho-proton elastic scattering to pion-proton elastic scattering:

$$\frac{d\sigma}{dt}(\rho p) = \left[\frac{1}{2} \sqrt{\frac{d\sigma}{dt}(\pi^+ p)} + \frac{1}{2} \sqrt{\frac{d\sigma}{dt}(\pi^- p)} \right]^2. \quad (V-6)$$

This equation comes from assuming quark forces are additive and spin-independent, and noticing that the quark structure for neutral pions is identical to that of neutral rhos, except for spin. Neutral pion cross sections are related to charged pions cross sections by isospin independence. By combining equations (V-5) and (V-6), taking the constant γ_ρ as a single free parameter, and using the pion-proton elastic scattering data of Foley et al.⁽³⁵⁾, the curves plotted in figure 16 are obtained. The agreement is remarkably good. The extrapolation to forward cross sections and total cross sections for rho production have been made with this theory. Table 4 lists cross sections obtained with one overall γ_ρ and with γ_ρ allowed to vary with photon energy; from these the quality of fits with a single γ_ρ can be evaluated.

The average γ_ρ obtained this way is given, in the conventional notation, by $\frac{\gamma_\rho}{4\pi} = 0.61$. Systematic errors in our data and in the elastic scattering data cause an uncertainty of about 20 percent

in this value. Other evaluations of this quantity can be made by comparing rho photoproduction to rho total cross sections. Assuming the entire forward rho elastic scattering cross section absorptive and applying the optical theorem to (V-5), we find

$$\left. \frac{d\sigma}{dt} \right|_{t=0} (\gamma + p \rightarrow \rho + p) = \frac{\alpha}{4} \left(\frac{4\pi}{\gamma_\rho} \right) \frac{[\sigma_{\text{TOT}}(\rho p)]^2}{16\pi}. \quad (\text{V-7})$$

Several groups have measured ρp total cross sections using rho photoproduction on heavy nuclei. Bulos et al. ⁽³⁷⁾ obtain a total cross section of 30 millibarns at 9 GeV, and McClellan et al. ⁽³⁸⁾ obtain 39 millibarns at 6 GeV. These values correspond to $\gamma_\rho^2/4\pi = 0.7$ and 1.09 respectively. The disagreement of these values from the generally accepted 0.5 is a difficulty of the VDM which has only showed up with the recent total rho-proton cross section measurements. ⁽¹²⁾

D. Phi

Differential cross sections obtained for phi photoproduction are listed in table 5, and plotted as functions of t for several energies in figure 21. Included in the plot at 6.5 GeV are data from Asbury et al. ⁽¹²⁾ and from the DESY bubble chamber collaboration. ⁽⁵⁾ The smooth curve is the same in all six parts of the figure; it comes from a quark model relation similar to the rho production relation, and will be discussed shortly. Good fits can be achieved with simple exponentials

$$\frac{d\sigma}{dt} = A \exp(Bt) \quad (\text{V-8})$$

TABLE 5 PHI PRODUCTION CROSS SECTION

-T (GEV/C) ²	ENERGY GEV	CROSS SECTION NANOBNR/(GEV/C) ²	-T (GEV/C) ²	ENERGY GEV	CROSS SECTION NANOBNR/(GEV/C) ²
0.30	6.50	130. +- 400.	0.70	6.50	180. +- 40.
0.30	6.50	370. +- 220.	0.70	6.50	160. +- 50.
0.30	13.00	530. +- 110.	0.70	11.50	85. +- 20.
0.30	13.00	610. +- 150.	0.70	13.00	80. +- 20.
0.30	14.50	370. +- 170.	0.70	13.00	98. +- 20.
0.30	14.50	510. +- 90.	0.70	14.50	70. +- 20.
0.30	16.00	260. +- 100.	0.70	14.50	98. +- 16.
0.30	17.80	310. +- 130.	0.70	16.00	56. +- 17.
0.40	6.50	410. +- 130.	0.70	17.80	63. +- 19.
0.40	11.50	360. +- 80.	0.90	6.50	59. +- 35.
0.40	13.00	240. +- 60.	0.90	11.50	37. +- 11.
0.40	13.00	340. +- 70.	0.90	13.00	34. +- 8.
0.40	14.50	210. +- 50.	0.90	14.50	35. +- 11.
0.40	14.50	350. +- 70.	0.90	16.00	30. +- 9.
0.40	16.00	210. +- 130.	0.90	17.80	26. +- 11.
0.50	5.50	190. +- 110.	1.10	6.00	40. +- 20.
0.50	6.00	320. +- 110.	1.10	13.00	29. +- 11.
0.50	6.00	310. +- 80.	1.10	16.00	27. +- 7.
0.50	6.50	460. +- 110.	1.38	16.00	7. +- 3.
0.50	6.50	290. +- 70.			
0.50	11.50	170. +- 40.			
0.50	13.00	120. +- 40.			
0.50	13.00	260. +- 70.			
0.50	14.50	150. +- 30.			
0.50	14.50	220. +- 40.			
0.50	16.00	130. +- 40.			
0.50	17.80	140. +- 40.			

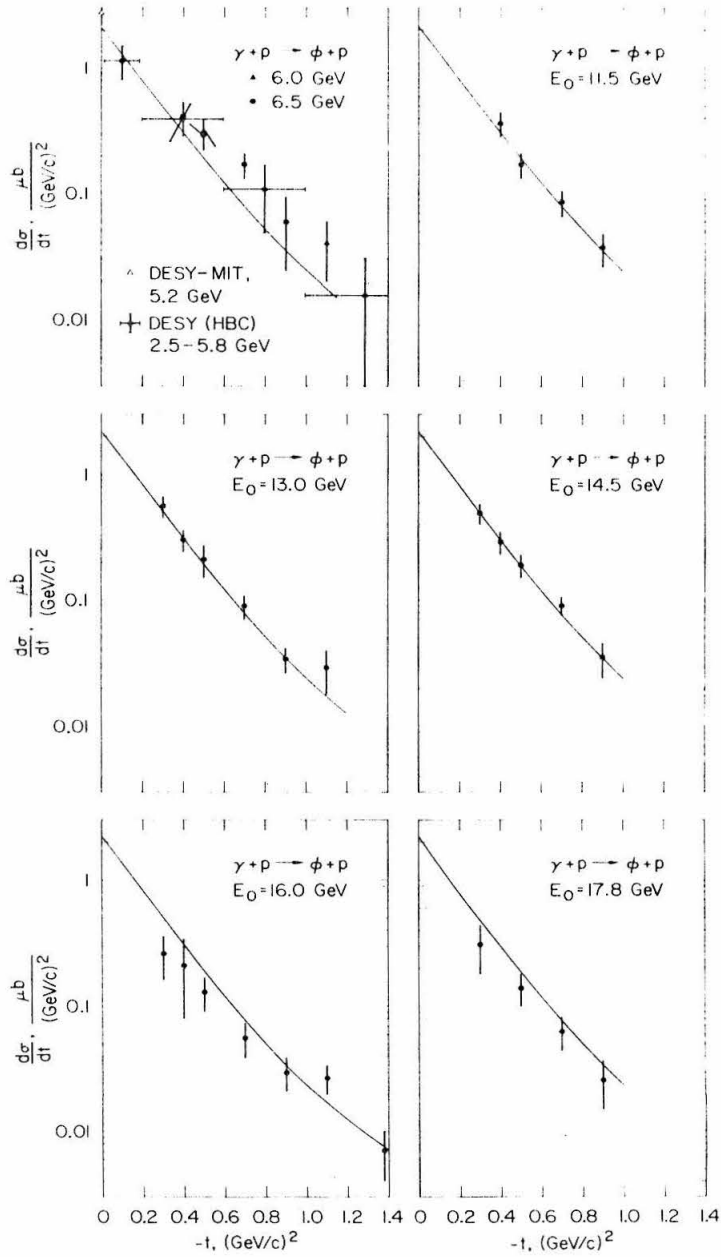


FIGURE 21 Phi Cross Section vs. t

with A and B typically $2 \mu\text{barn}/(\text{GeV}/c)^2$ and $4 (\text{GeV}/c)^{-2}$, respectively. Because the extrapolations involved are quite large, total cross sections are not reliably determined. However, extrapolations using equation (V-8) and using the quark model both yield total cross sections of $(.65 \pm .20) \mu\text{barn}$ at 6 GeV and $(.45 \pm .10) \mu\text{barn}$ averaged over the high energies. The ratio of the phi total photoproduction cross sections to the rho is roughly 1:25.

In figure 22 the phi cross sections are plotted against s on full logarithmic scales. There is some indication that the cross section falls with energy. The plotted straight line best fits determine an effective Regge trajectory

$$\frac{d\sigma}{dt} = C (s - M^2)^{2\alpha(t) - 2} . \quad (\text{V-10})$$

The effective Regge trajectory obtained in this way is plotted against t in figure 23. The data are not precise enough at high and low momentum transfers to make the calculation of a straight line effective trajectory significant.

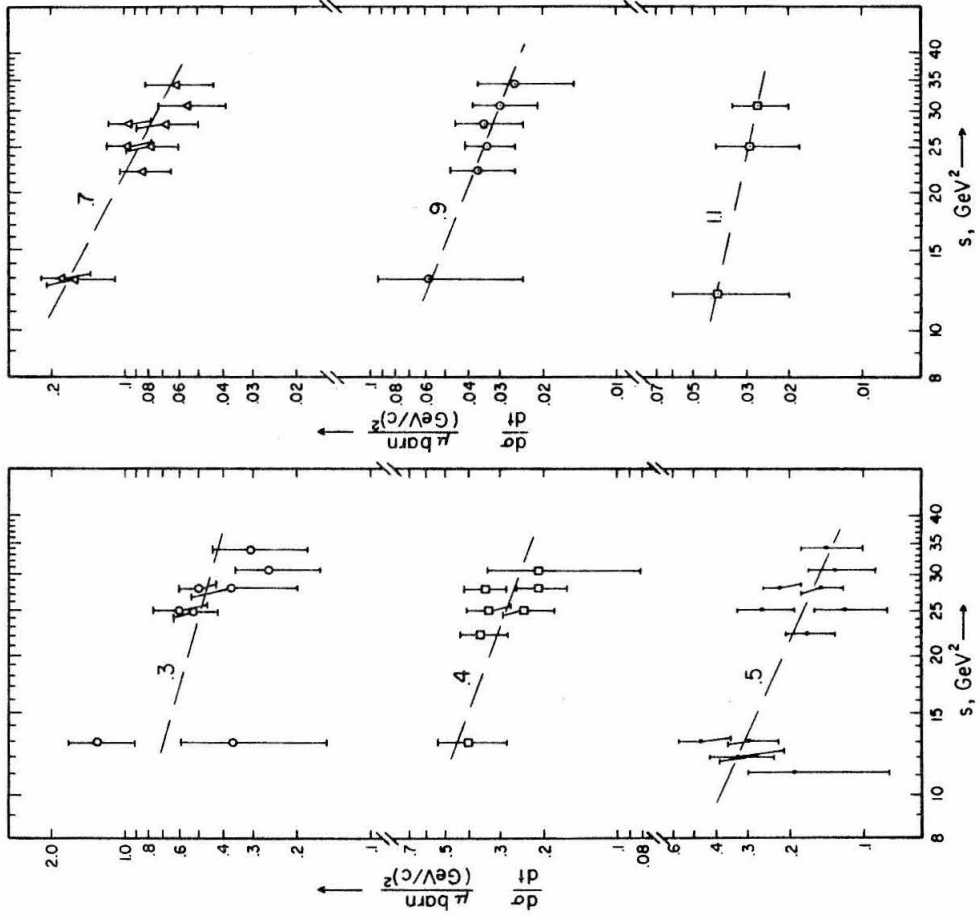
The cross section for phi photoproduction should be proportional to phi elastic scattering cross sections by the same VDM arguments used for the rho:

$$\frac{d\sigma}{dt} (\gamma + p \rightarrow \varphi + p) = \frac{\alpha}{4} \left(\frac{4\pi}{2} \right) \frac{d\sigma}{dt} (\varphi + p \rightarrow \varphi + p) . \quad (\text{V-11})$$

A quark model relation⁽¹⁸⁾ describes phi-proton elastic scattering in terms of measurable cross sections:

FIGURE 22 Phi Cross Section vs. s

$$\frac{d\sigma}{dt} (\gamma + p \rightarrow \phi + p) \text{ vs. } s$$



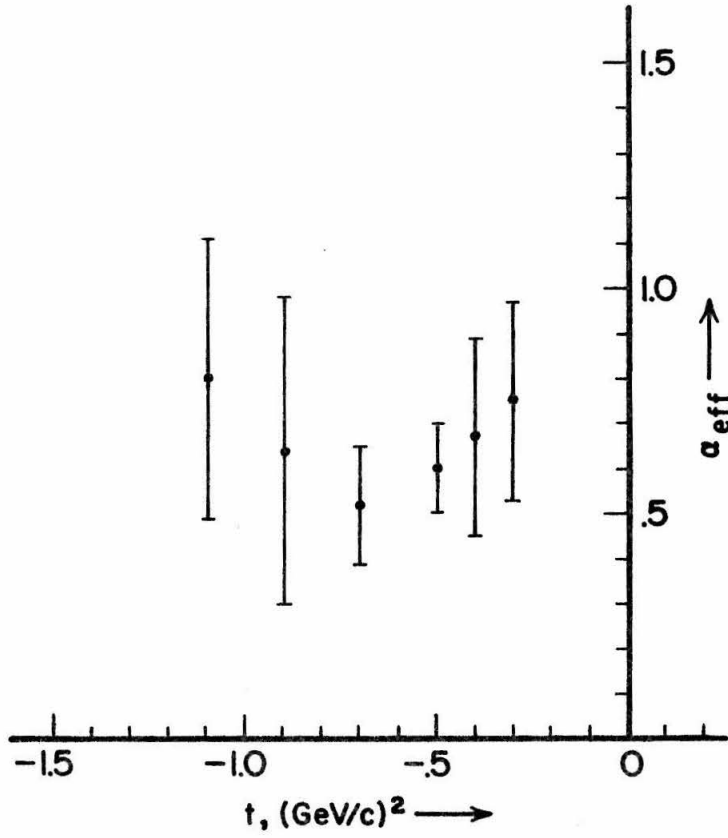


FIGURE 23 Phi Production Effective Regge Trajectory

$$\frac{d\sigma}{dt}(\varphi p) = \left[\sqrt{\frac{d\sigma}{dt}(K^+ p)} + \sqrt{\frac{d\sigma}{dt}(K^- p)} - \sqrt{\frac{d\sigma}{dt}(\pi^- p)} \right]^2. \quad (V-12)$$

All the cross sections in equation (V-12) are elastic. In this equation, Kp scattering is used to obtain the behavior of strange quark and strange antiquark scattering (the phi is made of a strange quark and a strange antiquark), and the πp scattering cross section subtracts off the non-strange quark part of Kp scattering. The smooth curve of figure 21 uses equations (V-11) and (V-12), with data from Foley et al. ⁽³⁵⁾, and $\gamma_\varphi^2/4\pi = 9.8$. This value is marginally consistent with predictions of $\frac{1}{\gamma_\rho} : \frac{1}{\gamma_\omega} : \frac{1}{\gamma_\varphi} = 9 :$

.65 : 1.33 using broken SU_3 . ⁽¹⁹⁾ Note that to obtain this consistency, a broken SU_3 model has also been used in evaluating phi-proton elastic scattering.

The quark model curve does not appear to fit data from all photon energies equally well. This is more likely to be a failure of the quark model, which involves data with considerable error bars and a rather large subtraction, than a failure of the VDM. Upon allowing the constant of proportionality between phi production and phi elastic scattering to vary with energy, the extrapolations to zero momentum transfer give the forward differential cross section $(3.2 \pm .4) \mu\text{barn}/(\text{GeV}/c)^2$ and total cross section $(.71 \pm .08) \mu\text{barn}$ at 6 GeV. The data from incident energies between 11.5 and 17.8 GeV do not differ significantly; the averages of the corresponding cross sections are $(2.1 \pm .2) \mu\text{barn}/(\text{GeV}/c)^2$ and $(.45 \pm .04) \mu\text{barn}$, respectively. These errors do not include an estimate for model

dependence. Anyone not trusting the quark model would do well to multiply the error bars by 2.5 in view of the large extrapolations involved.

E. $X^0(958)$

Dar and Weisskopf⁽⁸⁾ predict the cross section of X^0 production in the same paper where they successfully predict eta production. Although some data show a hint of such production (c f. figure 9f, the subtraction of 5.5 and 5.0 GeV, $t = -.3 (\text{GeV}/c)^2$ curves), in general this experiment is not sensitive enough to see production of the predicted size because of the large background from rho production.

F. "B"

Figure 24 depicts the subtracted yield from endpoint energies 14.5 and 13.0 GeV at $t = -.5 (\text{GeV}/c)^2$. In addition to peaks from pion, rho, and phi production, a distinct peak is visible at a mass of about 1240 MeV. Of 51 yield curves (counting subtractions) which covered this mass region, 8 showed peaks as unmistakable as this one, 13 had definite measurable peaks and the remainder were consistent with the presence of a peak with a cross section extrapolated from the measurable peaks. Peaks were most easily seen at about 14 GeV and for t between $-.3$ and $-.7 (\text{GeV}/c)^2$, where resolution and our data were best. No data in which this peak would have been visible were taken below 11.5 GeV photon energy.

All the observed peaks had a best fit mass value within 20 MeV of 1240 MeV. The width is hard to determine with poor resolution, but is roughly 100 MeV. Table 6 lists the cross sections

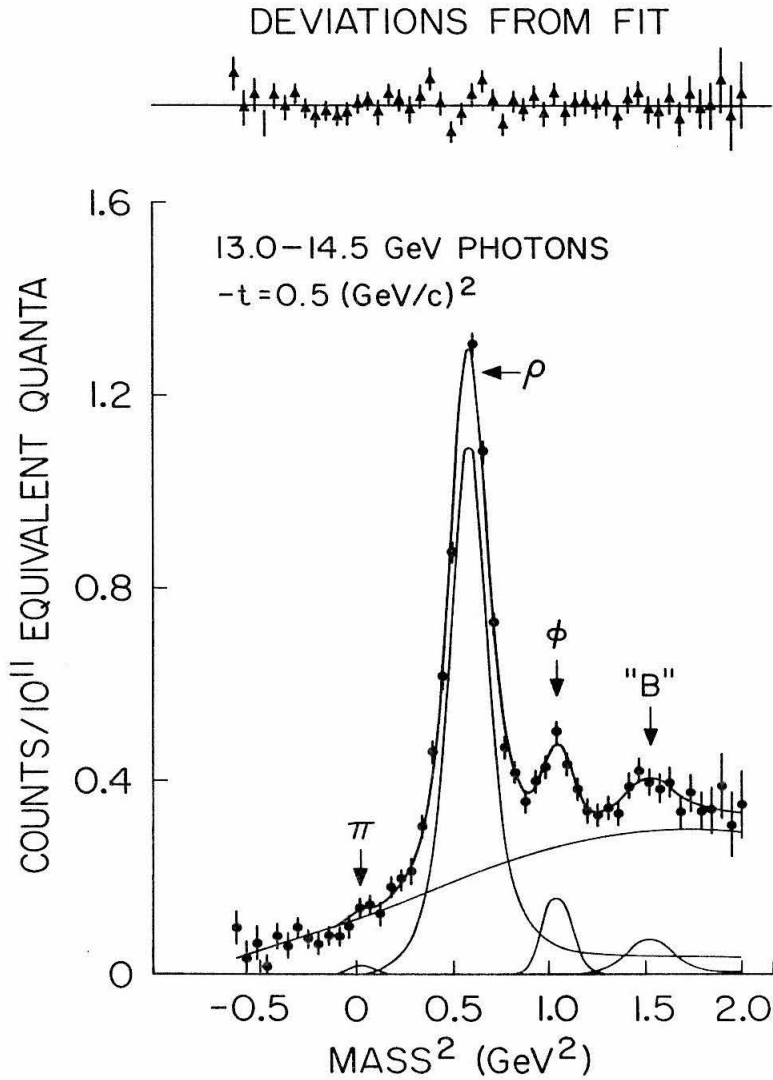


FIGURE 24 Subtracted Yield Curve Showing "B" Production

TABLE 6 "B" PRODUCTION CROSS SECTION

-T (GEV/C) ²	ENERGY* GEV		CROSS SECTION NANOBARN/(GEV/C) ²	
.30	13.00	Y	800.	+ - 400.
.30	13.00	Y	1000.	+ - 400.
.30	13.75	S	900.	+ - 300.
.30	13.75	S	450.	+ - 250.
.30	14.50	Y	400.	+ - 300.
.30	16.90	S	400.	+ - 300.
.40	13.75	S	350.	+ - 250.
.40	13.75	S	200.	+ - 100.
.40	14.50	Y	300.	+ - 250.
.40	14.50	Y	400.	+ - 300.
.50	12.25	S	400.	+ - 150.
.50	13.00	Y	400.	+ - 100.
.50	13.00	Y	300.	+ - 200.
.50	13.75	S	250.	+ - 100.
.50	13.75	S	180.	+ - 60.
.50	14.50	Y	250.	+ - 100.
.50	14.50	Y	300.	+ - 150.
.50	15.25	S	200.	+ - 150.
.50	16.00	Y	300.	+ - 100.
.70	12.25	S	60.	+ - 40.
.70	13.00	Y	100.	+ - 40.
.70	13.00	Y	70.	+ - 40.
.70	13.75	S	60.	+ - 30.
.70	14.50	Y	<50.	
.70	15.25	S	80.	+ - 50.
.70	17.80	Y	70.	+ - 40.
.90	ALL		<80.	

* Y IDENTIFIES DATA TAKEN FROM YIELD CURVE AT THE SPECIFIED ENDPOINT ENERGY. S IDENTIFIES DATA TAKEN FROM SUBTRACTION AT THE SPECIFIED AVERAGE ENERGY.

obtained for the measurable peaks, assuming a 100 MeV width. The cross sections are consistent with an $\exp(5t)$ dependence on t . No systematic dependence on photon energy is visible with the large errors and small range of energies of the data.

Possible identifications with known particles include the f^0 (mass 1264 MeV; width 145 MeV), the A_{2L} (1269; 26), the D (1285; 31) and the B (1221; 123). A disadvantage of the missing mass spectrometer technique is that only weak clues can be used to obtain the quantum numbers of any bumps observed. The large cross sections for production of this particle at high energy suggest that it may be diffraction produced, although the lack of data at low energies makes it impossible to prove this. Of the four possible particle identifications listed, only the B has the same charge conjugation (minus) as the photon, so only the B can be diffraction produced. This is why the particle is tentatively identified with the B. Speculations on Regge daughter trajectories and of the Veneziano representation⁽³⁹⁾ indicate there may be a vector meson near mass 1240 MeV, which may be the source of this bump. The question cannot be decided with the present data.

G. Mass Search

Systematic searches for production of particles with masses up to 2.0 GeV were performed at 16.0 and 17.8 GeV for $t = -.2$ and $-.3$ (GeV/c)². These searches were done with pairs of energies so that a bremsstrahlung subtraction technique could be used to eliminate s-channel resonances. The data can be seen in figures 25 and 26, taken at $t = -.2$ and $t = -.3$ (GeV/c)², respectively. Of these the data in figure 25 are the more reliable, being taken under more carefully controlled conditions and with greater statistical precision.

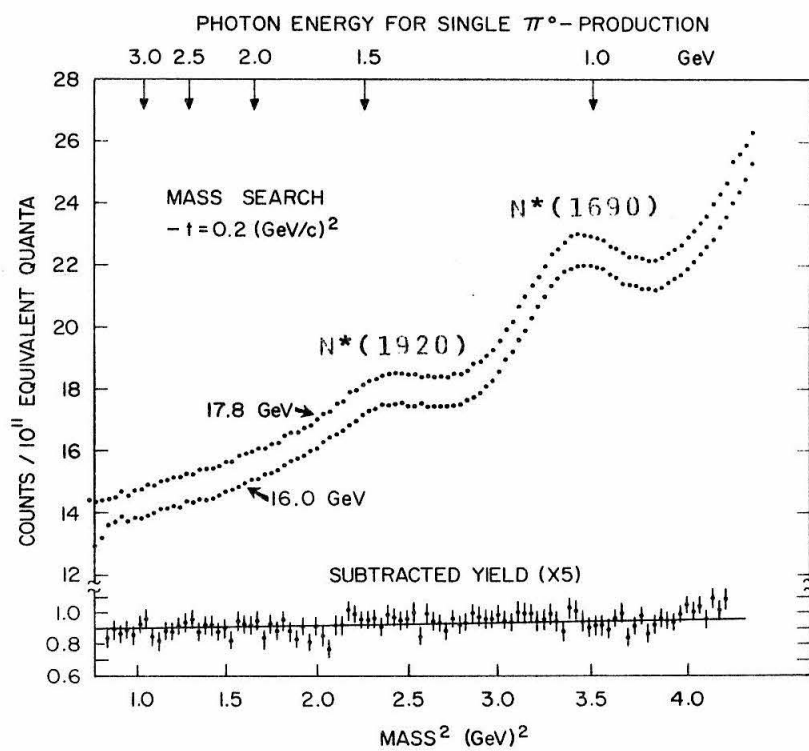
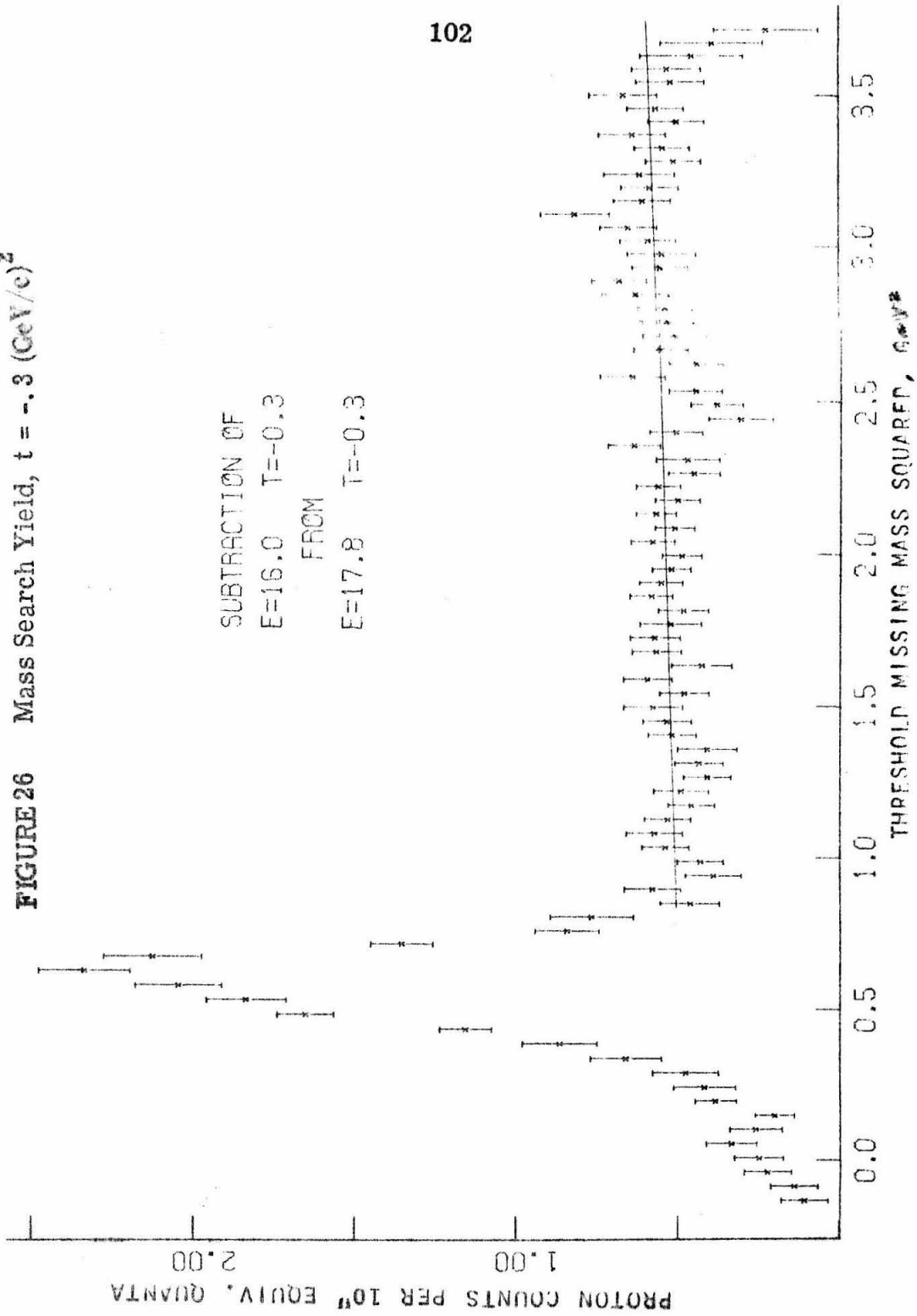


FIGURE 25 Mass Search Yield, $t = -.2 \text{ (GeV/c)}^2$

FIGURE 26 Mass Search Yield, $t = -0.3 \text{ (GeV/c)}^2$



It is clear to the eye that no significant peaks are visible. To make this observation quantitative, a straightforward statistical analysis was used. The subtracted data were fit with a straight line. This gives a surprisingly good fit; chi-squared is 103 for 102 degrees of freedom in the $-.2 \text{ (GeV/c)}^2$ search, and 56 for 59 degrees of freedom in the $-.3 \text{ (GeV/c)}^2$ search. The fit straight line was subtracted from the data. Production of a hypothesized particle was represented by a Gaussian peak, whose width, in three separate trials, was given by resolution alone, by resolution and a 100 MeV decay width, and by resolution and a 200 MeV decay width. The position of this peak was stepped one angle bin at a time over the entire range of the search, and its best-fit height determined with a least squares fitting program at each bin. The significance of the peak in "standard deviations" ("s. d.") was determined at each bin assuming random errors from counting statistics only. "Standard deviation" is put in quotation marks because significant errors, e.g., in the beam monitors, have been ignored. We estimate that a 5 "s. d." peak would be required for statistical significance. No peaks were found of more than 3.5 "s. d." For example, the $-.2 \text{ (GeV/c)}^2$ search for zero-width particles found two negative peaks, or valleys, of 3.1 and 2.6 "s. d.", and one peak of 1.9 "s. d.," with the remaining structure smaller than 1 "s. d." No apparent correlation between the structures in the two mass searches was observable. A 5 "s. d." peak corresponds to about 10 percent of the rho cross section, depending on effective missing mass (see table 7). Thus with 90 percent confidence, no new particles are seen which have mass between 1300 and 2000 MeV and cross sections greater than 15 percent of the rho's.

The high energy, low momentum transfer mass searches are sensitive primarily to diffraction-produced resonances, since other

TABLE 7 MASS SEARCH UPPER LIMITS

MASS MEV	100 MEV WIDTH ASSUMED		200 MEV WIDTH ASSUMED	
	$\frac{d\sigma}{dt}$ UBARN/(GEV/C) ²	RATIO TO RHO CROSS SECTION	$\frac{d\sigma}{dt}$ UBARN/(GEV/C) ²	RATIO TO RHO CROSS SECTION
1300	1.0	.06	1.4	.08
1450	1.1	.06	1.6	.09
1600	1.4	.08	1.9	.11
1750	1.6	.09	2.2	.12
1900	1.7	.10	2.4	.13

90 PERCENT CONFIDENCE LIMITS TO CROSS SECTIONS FOR THE MASS SEARCH

OF $-.2$ (GEV/C)². AVERAGE ENERGY 16.9 GEV.

particles' productions should fall rapidly with s . In particular, a vector meson with mass between 1500 and 2000 MeV and production cross sections comparable to the rho meson's should have been visible. The first "daughter" to the rho Regge trajectory, if parallel to the rho trajectory, would have produced a particle of mass approximately 1750 MeV.

An attempt at a mass search at 6.5 GeV, $t = -.9 (\text{GeV}/c)^2$ was cut short by equipment failure, and extended only to 1550 MeV. The yield curve is shown in figure 9t. No new particles are observed. Particles with production cross sections more than about one third of the rho's should have been visible.

APPENDIX A

This appendix will be devoted to describing experimental apparatus in more detail than was convenient in chapter II.

1. The SLAC Accelerator

The SLAC accelerator has been described in great detail elsewhere⁽⁴⁰⁾. Only those properties which influenced this experiment directly will be mentioned here.

The accelerator is uniquely well suited to a survey experiment using a missing mass spectrometer. Its maximum output energy, 20 GeV, is twice that of the next most energetic electron machine, the Cornell synchrotron, and over three times that of CEA and DESY. This permits surveying over a wide range of energies for which Regge theory is expected to work. SLAC's maximum current, 25 microamperes, is an order of magnitude greater than that of any other electron machine in the world. High current permits surveying a large range of energies and momentum transfers with good statistics in a relatively short time.

The high energy and current lead to a major problem with power dissipation and radiation. Beam monitors and targets have to be carefully designed to dissipate heat rapidly. Beam steering has to be watched carefully to prevent equipment damage; for example, once during this experiment the beam drilled a hole through the beam vacuum pipe. Common-sense radiation safety precautions make entry to the experimental floor slow and reduce the experimenter's interaction with his apparatus to what he can do with remote control and television. Sometimes the amount of beam delivered has to be reduced to protect people.

The most serious experimental nuisance at SLAC is the duty cycle, about .06 percent at maximum repetition rate. Because the klystrons which supply the accelerating power cannot be run continuously at peak output, electrons are accelerated in 1.6 microsecond long pulses, 360 per second. In typical running conditions an experimenter receives about 10^8 electrons per nanosecond while the beam is actually on. An unshielded counter exposed to room background simply turns on for the length of a beam pulse. In order to make full use of the possible counting rate, an experimenter is forced to separate out genuine events from background mechanically before using scintillation counters. In practise this means using a well shielded, very expensive spectrometer. Even so, the experimenter is plagued by accidental coincidences due to the resolving time of his electronics and must make corrections. In this experiment the maximum usable beam current was frequently set by the resolving time of the electronics.

Another problem was instability of the beam. About once every ten minutes, a klystron would overload and shut itself off, and there was a chance of a steering change. Sometimes steering would change for no apparent reason. The experimenter had to keep an eye on the beam position monitors continually. Steering changes were a major source of beam monitor instability for this experiment.

The energy of the beam transmitted to the experimenter is determined by a series of bending magnets in the switchyard at the end of the accelerator. Beam energy is measured by measuring the magnetic field in a bending magnet which is identical to the ones in the switchyard and wired in series with them. A variable slit determines the energy resolution. For this experiment it was set to require one percent resolution, allowing almost all the beam to be

transmitted, since the spread of energies from the machine is typically .5 percent.

Several times during the running of the experiment the beam was "chopped" so that time of flight could be used to distinguish particles.⁽⁴¹⁾ The chopping was accomplished near the electron gun by deflecting the beam electrostatically with a 20 MHz. sine wave voltage. A slit allowed the beam through only when the chopping voltage passed through zero, thus dividing the beam into one nano-second long bunches spaced every 25 nanoseconds. To distinguish particles of different velocity the experimenter measured the phase of the 20 MHz. chopping voltage at the time of the particles' arrival. With this method, protons were distinguishable from pions easily at even the highest momentum measurable in the 1.6 GeV/c spectrometer. Unfortunately, chopping reduced beam current by about a factor of five, so time of flight was used only for testing.

2. The Photon Beam

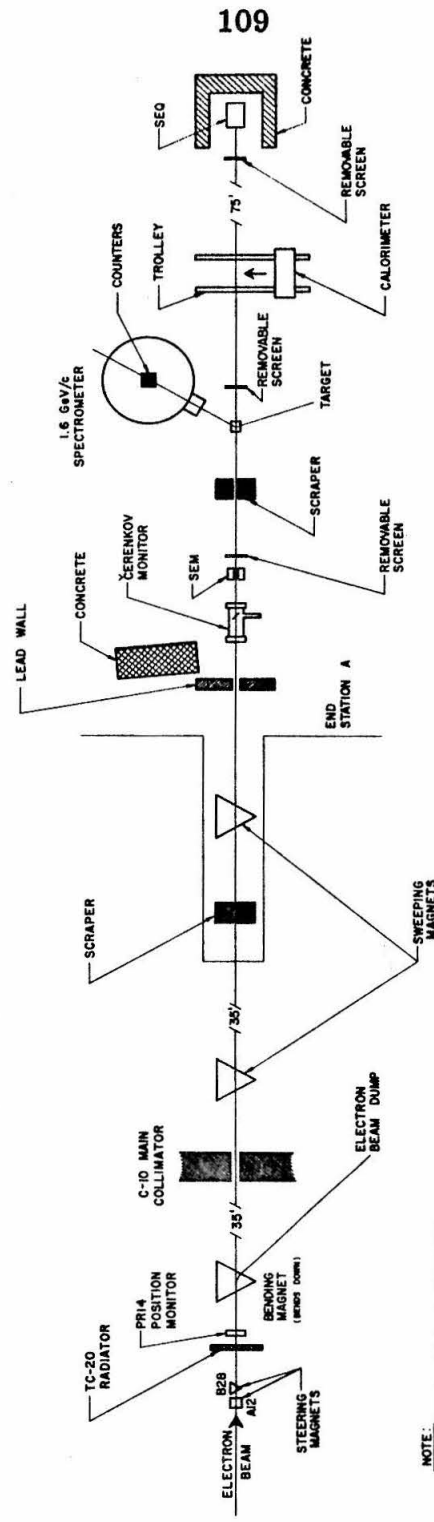
The beam line is diagrammed in figure A-1.

Fifty meters before the hydrogen target, the SLAC electron beam hit a .1 inch (.03 radiation lengths) aluminum radiator. Electrons were then bent out of the beam and dumped. A television camera viewing the position monitor, a gas Cerenkov cell just behind the radiator, allowed the experimenter to keep track of beam size, shape, and position.

The bremsstrahlung photon beam was reduced to the desired dimensions by the main collimator. Secondary collimators reduced beam halo, and sweep magnets removed electrons produced on the collimators. After traversing the target the beam was stopped and

FIGURE A-1 Photon Beam

PHOTON BEAM, SIMPLIFIED.
 APPROXIMATE SCALE:

NOTE:
 ALTHOUGH RELATIVE POSITIONS
 OF COMPONENTS ARE TO SCALE,
 COMPONENT SIZE IS EXAGGERATED
 FOR CLARITY.

monitored in the secondary emission quantameter (SEQ). Typical beam size at the target was 2 cm. by 2 cm. Photon beam power was adjusted to keep accidental rates in the electronics at a reasonable level, and varied between 200 and 1500 watts, about 5×10^{11} equivalent quanta per second.

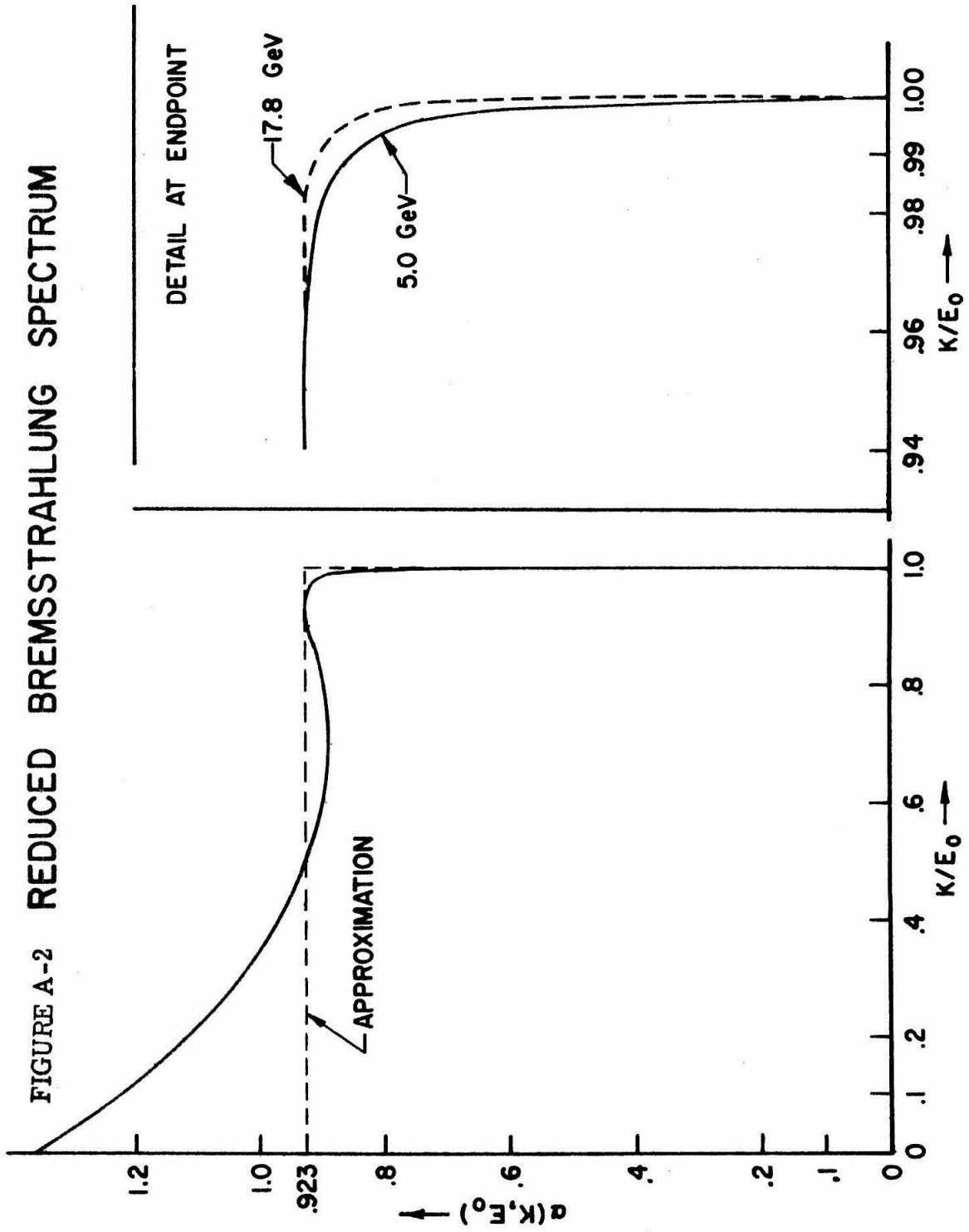
The beam was steered using four screens viewed by television. Three zinc sulphide screens were located in front of and just behind the target and just in front of the SEQ. These screens could only be in the beam when data were not being taken, so only the gas Cerenkov cell just behind the radiator was usable as a continuous check on the beam steering.

The Cerenkov monitor, the SEM and the SEQ were used to monitor the beam. The calorimeter was occasionally moved into the beam line for calibrations of the SEQ. Monitoring will be discussed in the next section.

The distribution of photon energies in this bremsstrahlung beam has never been measured experimentally. The spectrum was therefore calculated using the Caltech program BPAKI⁽⁴²⁾ and the SLAC program BREM⁽⁴³⁾. The former has provisions for simulating beam collimation, and the latter is specifically designed for high energies. The programs agreed within .5 percent, once the SLAC program was properly normalized⁽⁴³⁾. Both also indicated that details of the energy spectrum near the endpoint would produce no effects visible within the experimental resolution. The calculated shape of the reduced bremsstrahlung spectrum factor $\alpha(k, E_0)$ is shown in figure A-2. This factor is defined by

$$N(k) dk = N_{\gamma} \alpha(k, E_0) \frac{dk}{k}$$

FIGURE A-2 REDUCED BREMSSTRAHLUNG SPECTRUM



where $N(k)$ is the number of photons per unit energy at photon energy k , N_γ is the number of equivalent quanta and E_0 is the endpoint energy. The integral of α over all k is normalized to E_0 . For narrow particles, the pion, eta and phi, only the value of α near the endpoint energy is vital, and the approximation indicated with a dashed line in figure A-2 was used (the change in normalization was, of course, corrected for).

3. Beam Monitors

The secondary emission quantameter (SEQ) was the primary beam monitor and the beam dump. This device is described elsewhere⁽⁴⁴⁾, and will be discussed only briefly here. It consists of twenty .5-inch thick water-cooled copper plates alternating with nineteen .0005-inch gold plated aluminum foils. The assembly is inside an evacuated steel enclosure. The copper plates are at high voltage, typically -300 volts. An incoming photon or electron starts a shower in the copper plates. As the charged particles of the shower leave the negatively charged plates, electrons from the ionization of atoms near the rear surface of the plate can be thrown from the plate (secondary emission). These electrons are collected by the foils, and charge is integrated on a capacitor. The charge collected is ideally proportional to the energy in the incident beam.

The SEQ is not an absolute device and must be calibrated periodically. The SLAC silver calorimeter⁽⁴⁵⁾ was used for this purpose. The Cerenkov monitor (to be described below) was used as an intermediate standard, since the calorimeter and the SEQ cannot be used simultaneously. Calibrations generally were consistent within one percent. The calibration value obtained was 2.11×10^6

GeV/ μ coul (incident beam energy per unit charge collected). Absolute calibration was also tested against the SLAC precision toroid using a positron* beam. Agreement with calorimeter calibrations was within two percent.

The SEQ is designed to handle up to ten kilowatts incident beam power, the limit being set by heat transfer rate in the copper plates. Its useful aperture is about 8 inches by 8 inches, far more than adequate for the beam of this experiment. Dependence of the SEQ's response on beam intensity and steering was tested with a positron beam and found to be negligible for this experiment.

Short term stability of the beam monitor is important to the validity of a yield curve, which is constructed out of about twenty individual runs taken over a two hour period. The SEQ was therefore continuously checked with two supplementary monitors and also verified against pion and proton counting rates.

The more reliable auxillary monitor was the Cerenkov monitor⁽⁴⁵⁾. This consists of a tube filled with Helium gas. Cerenkov light from pairs produced in a thin foil intercepting the beam is reflected onto a photomultiplier tube whose output is integrated. The ratio of SEQ charge to charge on the Cerenkov monitor generally stayed constant to within .5 percent, though the Cerenkov monitor was sensitive to beam steering. The SEM (secondary emission monitor) was very sensitive to beam steering, and in general only tracked well under unusually stable beam conditions.

* For technical reasons, a positron beam was available to us for testing purposes, but not an electron beam. Because the SEQ measures a shower from the primary particle, it responds to electrons, photons and positrons in very nearly identical manners.

If one divides pion counts by the charge accumulated on the SEQ, he should observe a smooth variation with spectrometer angle. This was a useful technique for diagnosing SEQ behavior when analyzing data offline. Where data were redundant enough the proton counting rate could also be used. The details of this relatively complex method are described in appendix B, section 1. These checks showed the SEQ's short term stability to be about $\pm .2$ percent under steady beam conditions.

4. Hydrogen Target

A diagram of the liquid hydrogen target assembly⁽⁴⁶⁾ is shown in figure A-3.

The target cell was a cylinder 12 inches long and 2 inches in diameter, with the axis parallel to the beam direction. Its walls were of .005 inch mylar and the beam entrance and exit windows of .005 inch aluminum. The cell was long enough that its end windows were not visible to the spectrometer. Its diameter was kept small and its walls made of thin mylar to reduce the amount of material protons had to go through before being analyzed.

A supply of gaseous hydrogen under 8 to 10 p. s. i. pressure kept the target cell filled. A large reservoir, filled from an independent liquid hydrogen source, served as a heat sink both to condense the hydrogen supply and to carry off heat left in the cell by the beam. As the beam traversed the target and heated the liquid hydrogen locally, convection currents were generated which carried the warm hydrogen upward to thermal contact with the reservoir. The hydrogen in the target, thus being kept at the temperature of boiling hydrogen at one atmosphere pressure, had density .070

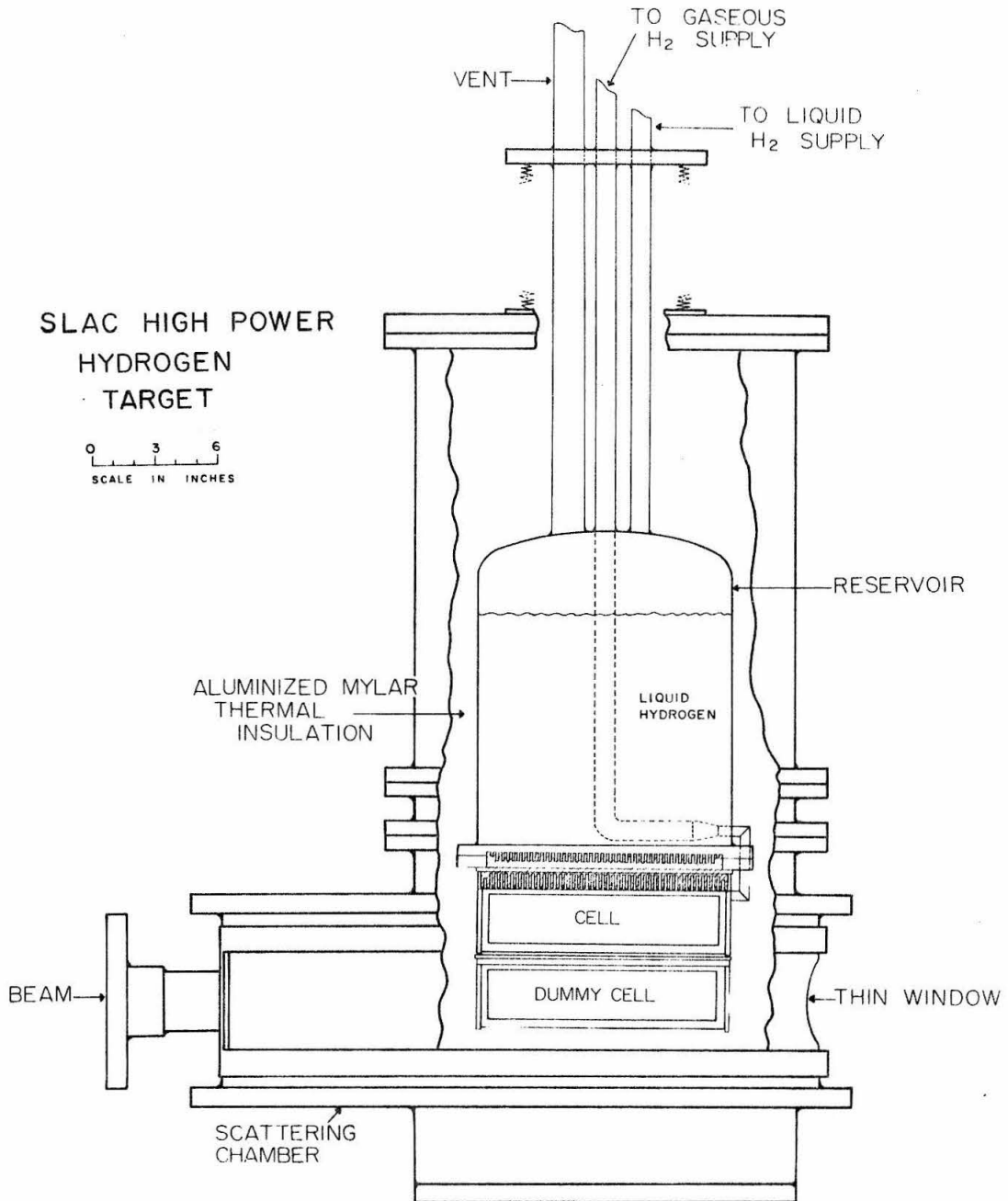


FIGURE A-3

Hydrogen Target

gm/cm³. Since the target was designed to keep a well-focussed electron beam from causing local boiling, the 2 cm. by 2 cm. photon beam used in this experiment was easily handled.

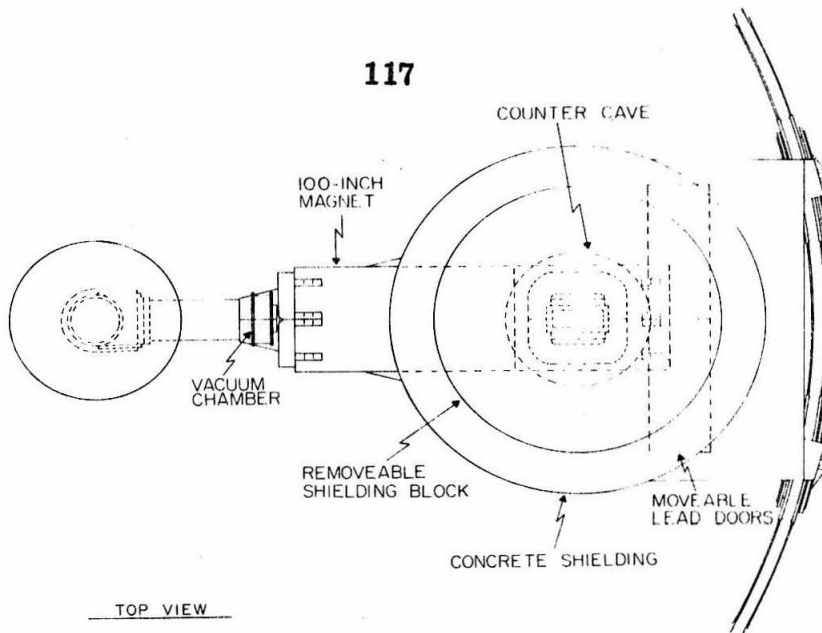
The entire target and reservoir assembly could be raised pneumatically to replace the hydrogen target with an identical but empty "dummy" cell for empty target runs. This provision is necessary because emptying the target and refilling it takes hours. The equality of counting rates for dummy target and an emptied real target was verified.

The spectrometer viewed the target through a two inch high slit, which masked out all of the target assembly but the liquid hydrogen cell. A second slit with its jaws perpendicular to the beam line determined the length of the hydrogen target visible to the spectrometer. This aperture was kept open 6.0 inches, making the effective target length $(6/\sin \theta)$ inches, where θ is the angle between the spectrometer and the beam.

5. The Spectrometer

The SLAC 1.6 GeV/c spectrometer⁽⁴⁷⁾, illustrated in figure A-4, analyses the momentum and angle of a particle emerging from the target. The angle θ between the spectrometer and the beam can be set to within .001 degrees by remotely rotating the spectrometer around the target. The weak focusing magnet bends particles upwards ninety degrees on a 100 inch radius. Particles travel through the magnet in an airtight chamber which, for this experiment, was filled with helium. At the top of the spectrometer a three foot thick concrete cave with lead access doors shields the counters from room background.

117



TOP VIEW

SLAC 1.6 GeV/c SPECTROMETER

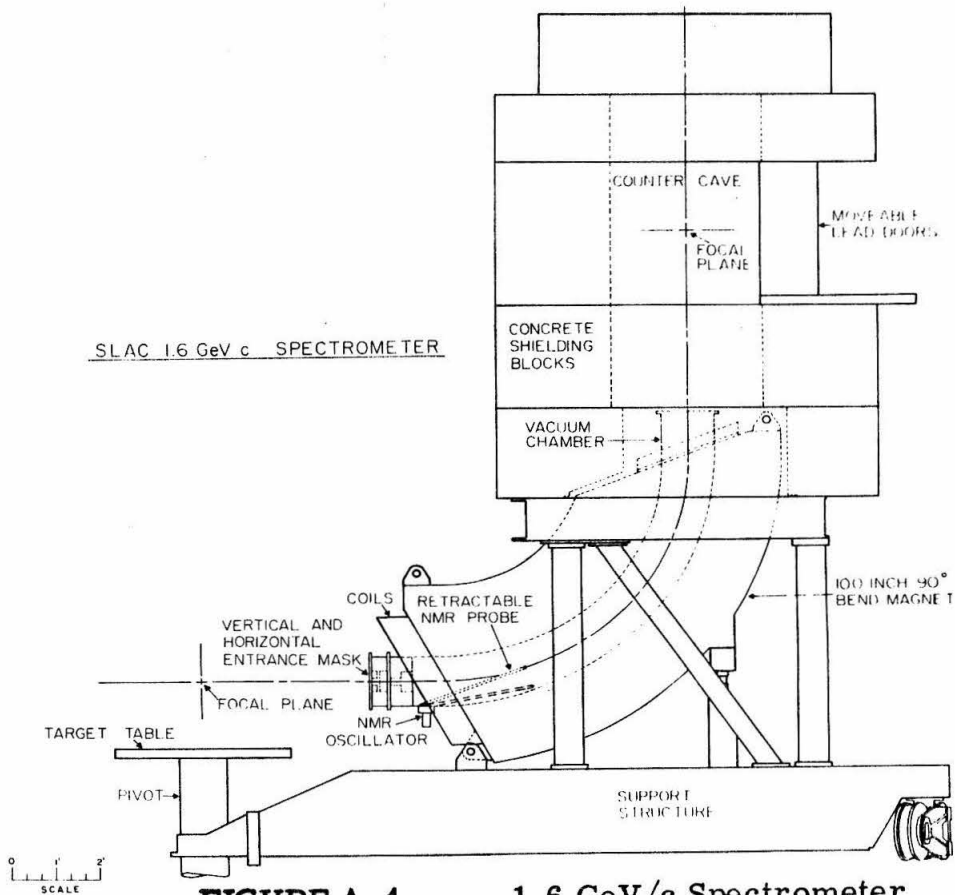


FIGURE A-4

1.6 GeV/c Spectrometer

The magnet is second-order corrected. Ideally, a particle of momentum p and angle θ is focused to a point on a p - θ plane regardless of where along the length of the target it was produced. Both p and θ focus in a single plane, and this plane is perpendicular to the central ray. Because the focal properties are not affected if the counter telescope is rotated about the direction of incoming particles, a hodoscope can be oriented along interesting kinematic lines. In this experiment, for example, different hodoscope counters corresponded to different missing mass.

The optical properties of the magnet, measured with a floating wire technique⁽⁴⁸⁾ and with an electron beam directly from the accelerator, agreed with design parameters within experimental errors. The momentum dispersion is $1.65 \pm .02$ inches per percent (the error is the uncertainty in the experimental measurement), and resolution .08 percent. Angle dispersion is $.323 \pm .015$ inches per milliradian, with resolution 0.4 milliradian. The magnet's resolution was good enough to be neglected as a contribution to mass uncertainty. The usable vertical (ϕ) angle acceptance is 60 milliradian, and is defined by a fixed mask. The magnet momentum and horizontal (θ) angle acceptances are ± 5 percent and ± 17 milliradian, respectively, but in this experiment p and θ apertures were limited by the area of the hodoscope in the focal plane, 6 inches by 10 inches. These dimensions would correspond to ± 3 percent in momentum and 18.5 milliradian in angle if the hodoscope counters were aligned with their long edges parallel to the momentum axis. The product of the acceptances, $(\frac{\Delta p}{p}) \Delta \Omega$, for each of the eight hodoscope counters is $(8.5 \pm 0.4) \times 10^{-4}$ steradian-percent.

Nuclear magnetic resonance (NMR) was used to determine magnetic field strength. The NMR probe was swung into the center

of the vacuum chamber on a boom when readings were taken. The NMR system was extremely sensitive; changes of one part in 10^5 were easily visible. Stability of the power supply and NMR system were such that readings taken several hours apart agreed to this accuracy, once the magnet was allowed to warm up. A precision current shunt on the power supply was calibrated to provide a second magnetic field measurement.

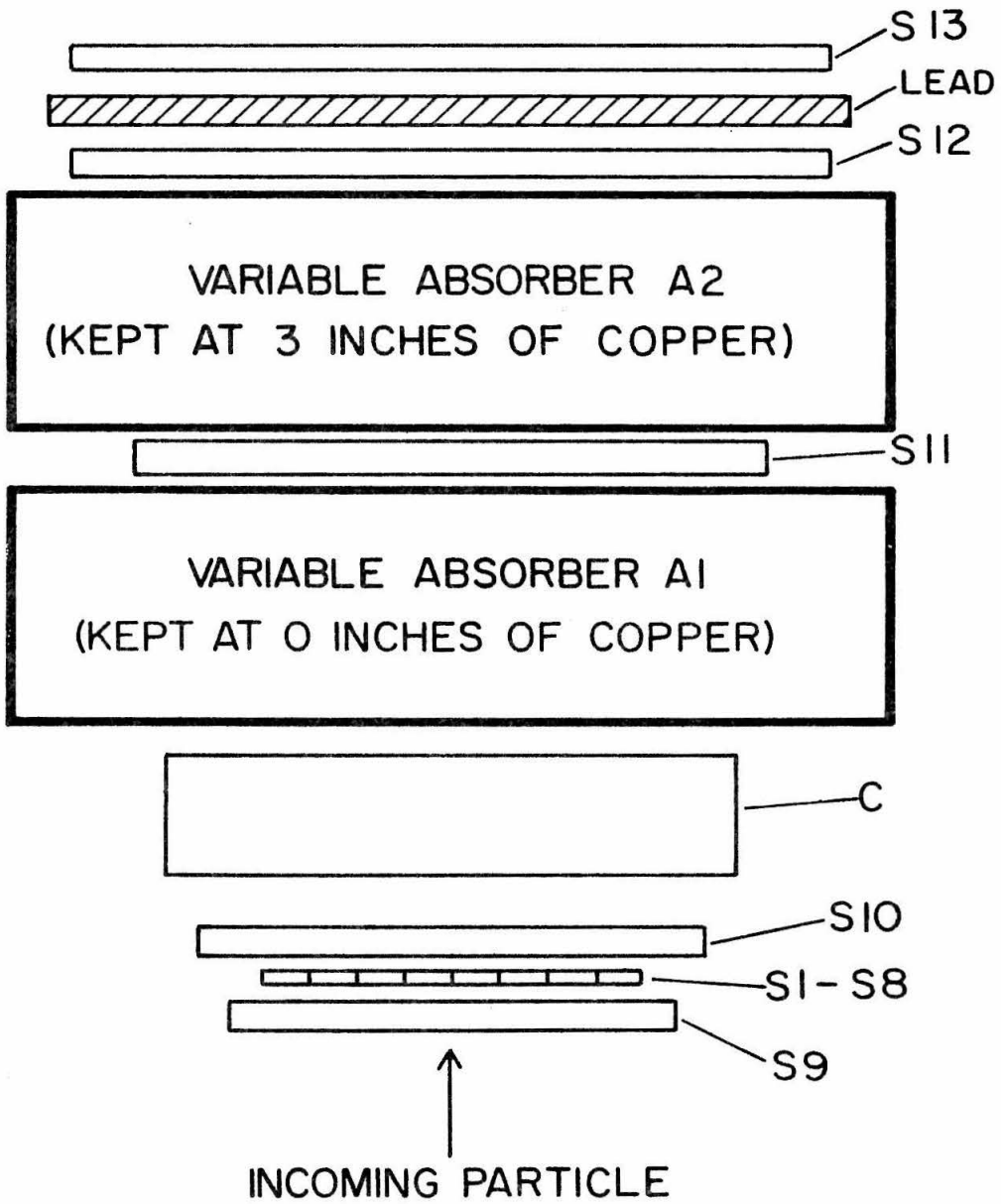
Estimated errors in the momentum and spectrometer angle calibrations are $\pm .2$ percent and $\pm .3$ milliradians, respectively. The calibration of momentum and spectrometer angle measurements was verified by observing the recoil proton from elastic positron-proton scattering. The calculated acceptance of the magnet was also crudely verified in this way.

6. Counters

The counter telescope is illustrated in figure A-5. The two main trigger counters S9 and S10 sandwich the eight-counter hodoscope, which lies in the focal plane of the magnet. The remainder of the telescope is used to separate the protons from other incoming particles. It consists of a Lucite Cerenkov counter C, an unused variable absorber A1, a third trigger counter S11, a second variable absorber A2 set to three inches of copper, and finally two counters S12 and S13, separated by a lead absorber. The entire telescope assembly can be rotated about an axis through its middle and parallel to the path of incoming particles.

The large scintillation counters S9, S10, S11, S12 and S13 are made of .5 inch thick Pilot B scintillator. Counter area increases with distance along the incoming particles' path to

COUNTER TELESCOPE



SCALE: 1/3

FIGURE A-5

Counter Telescope

accommodate the beam's angular dispersion: S9 is 7 inches by 11 inches, and S12 is 10 inches by 14 inches. The eight hodoscope counters S1 through S8 are made of quarter inch Pilot B scintillator, and are each 10 inches long and .75 inches wide. RCA 7850 photomultiplier tubes are used on all counters S1 through S13 except S9 and S10, where Amperex XP1020 tubes were used.

The Cerenkov counter has four RCA 8575 photomultiplier tubes viewing a 9- by 13- by 2-inch active volume of UVT Lucite. It relies on total internal reflection to conduct Cerenkov light from highly relativistic particles to the photomultipliers, and is wrapped in black paper to absorb light which is not reflected. Thus even 1400 MeV/c protons, which are above the threshold for producing Cerenkov radiation (850 MeV/c), are not counted; their Cerenkov light is produced at too small an angle for internal reflection. Pions are counted with better than 98 percent efficiency at all momenta used in this experiment. The counting efficiency for protons varies with momentum, and is shown in table A-1. The numbers at high momentum were determined using time of flight to separate protons from pions. At the lower momenta, range requirements were used to identify protons for the test.

The flux of pions was roughly equal to the proton flux, with no other particles counting significantly. Good pion rejection was not vital because pion counting rate varies smoothly with angle. Since cross sections are determined by separating steps from smooth background, additional smooth background from pion leakage affects the statistical quality of the data, but not cross sections. A pion rejection factor of ten would have been adequate for most data.

At the lowest momenta (t of $-.12$ and $-.2$ (GeV/c)²) protons stopped in the Cerenkov counter. Protons ionize at several times

TABLE A-1
Cerenkov Counter Efficiency for Protons

<u>- T</u>	<u>Proton Momentum</u>	<u>C Efficiency</u>
$< .9 \text{ (GeV/c)}^2$	under 1000 MeV/c	1 \pm .5 percent
.9	1060	1.5 \pm .5
1.1	1200	2.8 \pm 1.0
1.38	1400	5.8 \pm 1.5

the minimum rate at these momenta, so pulse height requirements in S9 and S10 separated pions from protons cleanly. The high voltages to the photomultiplier tubes of the hodoscope counters were reduced so that only protons would produce detectable signals. For intermediate momenta, t between $-.3$ and $-.7$ $(\text{GeV}/c)^2$, protons were stopped in A2. Pulse height in counters S9, S10, and S11 was again useful, but more nearly marginal than when the proton ionized heavily. In fact, at t of $-.5$ and $-.7$ $(\text{GeV}/c)^2$ it was necessary to use the Cerenkov counter to veto pions. At these momentum transfers counting rates had fallen enough that dead time loss was not too large. At momentum transfers corresponding to t of $-.9$ $(\text{GeV}/c)^2$ and greater proton range and ionization criteria became useless, and only the Cerenkov veto was left to reject pions. Fortunately the ratio of pions to protons incident was favorable, one to two or better, even in the region of low proton counting rate.

During the early running at intermediate momenta, complex triggering logic was used to perform a better separation. For each momentum transfer a thickness of copper for absorber A1 was chosen to increase proton ionization in S11, and pulse height requirements were made on that counter. Absorber A2 was adjusted so that protons just stopped in it, and S12 used in anticoincidence in the proton signal. These refinements were later dropped as unnecessary, inconvenient and conducive to errors in setting the absorbers. Furthermore, the S12 anticoincidence forced a decrease in data taking rate as it increased dead time losses.

Throughout the experiment pions were counted in addition to protons in order to check counter stability and beam monitors, as well as to keep an eye on pion background. A coincidence between the Cerenkov counter and S12 and S13 was required, so that both

range and velocity were used as separation criteria. Many pions were absorbed in the three inches of copper in A2, so a neat division of all incident particles into protons and pions was not made.

7. Electronics

The electronics used in making the "PROTON" and "PION" logic pulses is diagrammed in figure A-6. In this figure horizontal distance is proportional to time. The basic requirements for identifying a particle as a proton or a pion have already been described. Changes in coincidence logic at different momenta were accomplished by switching inputs to coincidence circuits on or off. Timing and discriminator threshold in counters S9, S10 and S11 also changed as proton flight time and ionization varied from momentum to momentum. These variations were accommodated with the variable delays and with variable attenuators in front of the fixed threshold discriminators. All fast logic was done with Chronetics 100 MHz. logic units.

Hodoscope trigger logic is shown in figure A-7 for counter S4 as an example. Other hodoscope counters lacked the singles scaler and the accidental channel 4.(PROTON). Switches on the circuit "CHOICE" could be set to demand coincidences with a "PROTON" pulse, a "PION" pulse, a time of flight window, or any combination of these. In normal running only the "PROTON" coincidence was required.

The coincidence units 9.(10), 9.10.(C), 12.(13), and 4.(PROTON) monitor accidental coincidences in the basic proton trigger, the Cerenkov counter veto, the pion trigger and hodoscope counters, respectively. To accomplish this signals are deliberately

FIGURE A-6
PROTON AND PION
TRIGGER LOGIC

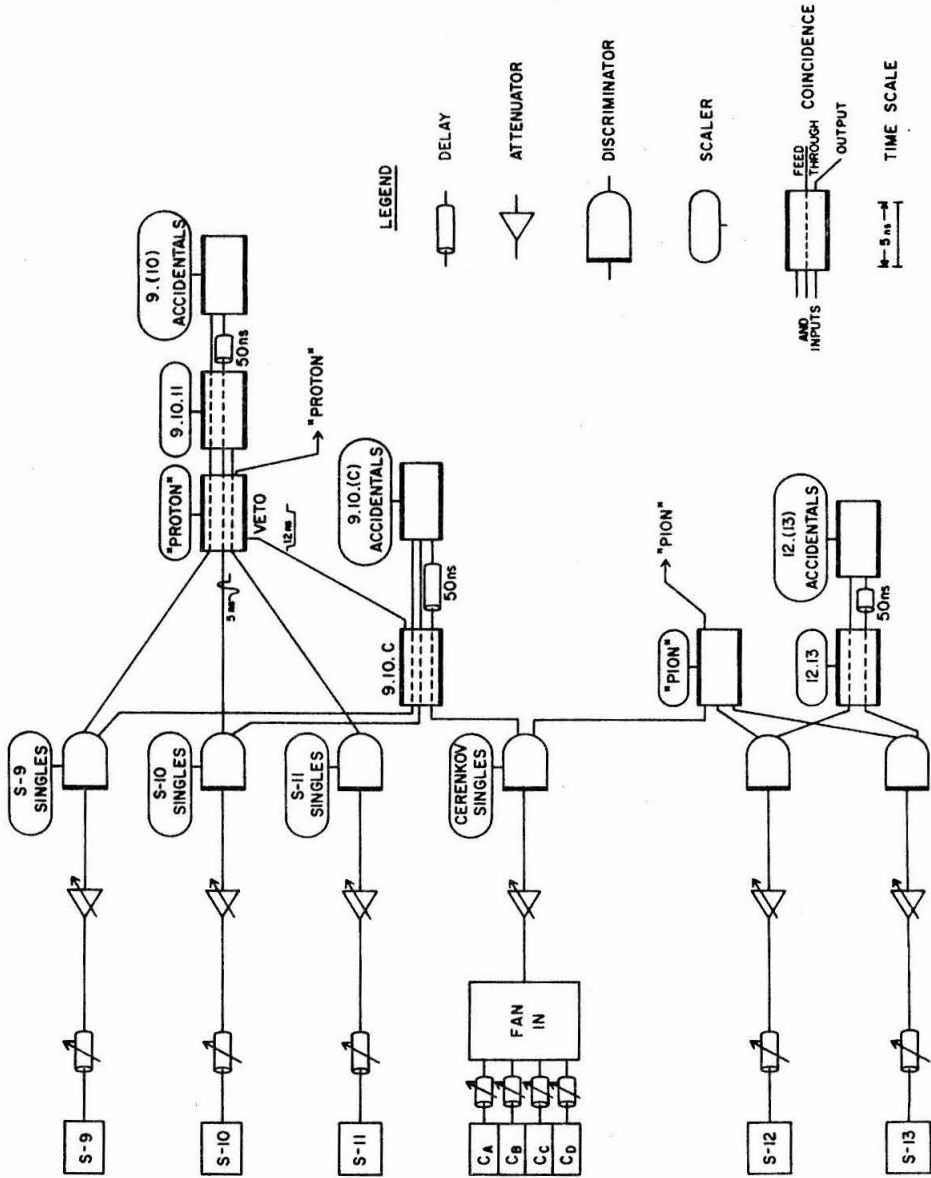
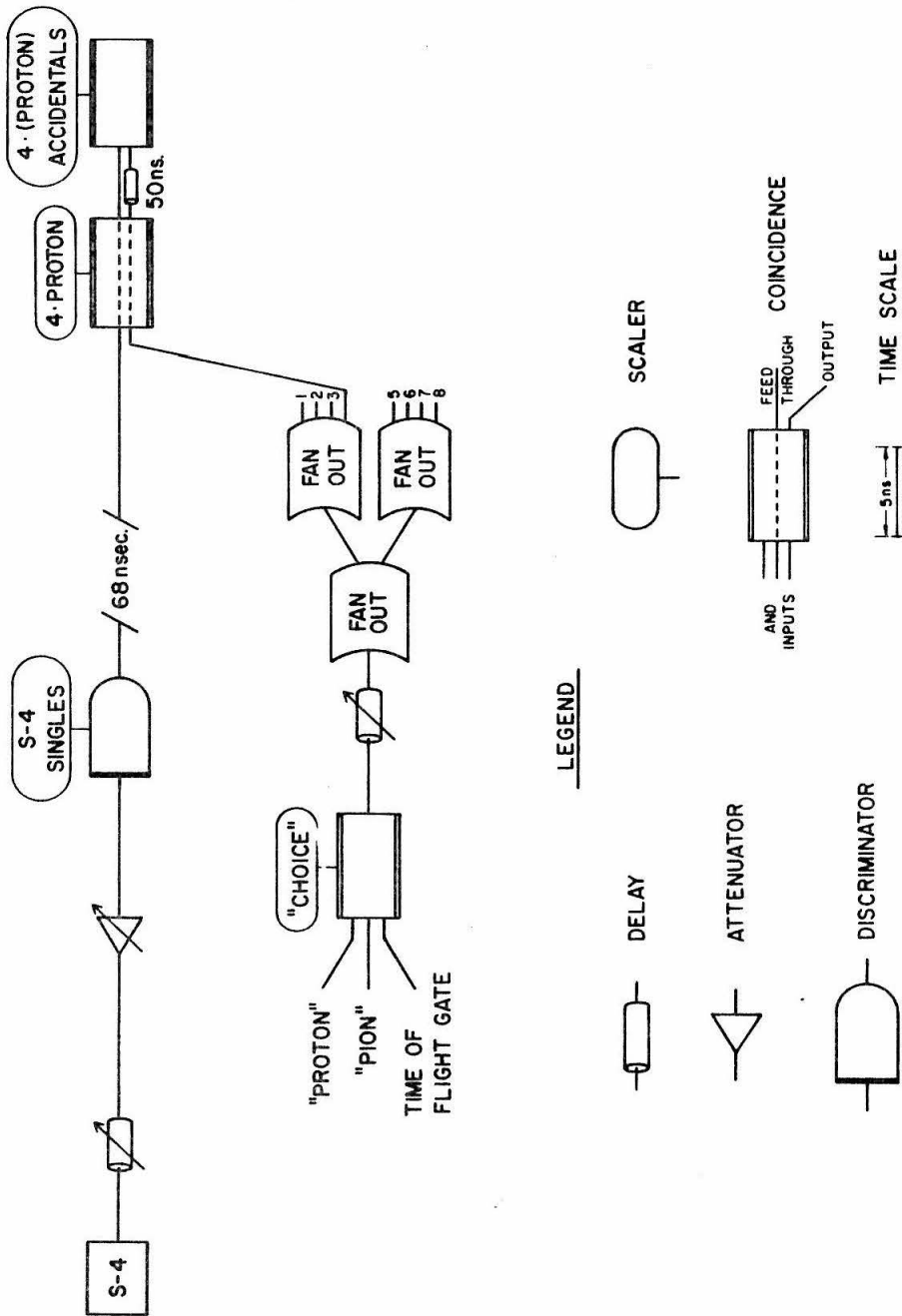


FIGURE A-7
HODOSCOPE TRIGGER LOGIC



mistimed by 50 nanoseconds before coincidences between them are measured. These "delayed coincidences" are guaranteed to be accidentals, and thus are proportional (within statistics) to accidental rates in the corresponding important coincidence circuits. The accidentals monitors are calibrated by varying beam intensity. Their usage in computing corrections is described in appendix B, section 1.

In order to improve timing resolution and decrease double pulsing in the discriminators, signals from all counters were clipped at the photomultiplier tube base with a two nanosecond long cable terminated in 10 ohms resistance. Logic pulses in the electronics were 5 nanoseconds wide, except the veto pulse from 9.10.C to "PROTON", which was 12 nanoseconds wide. The overall speed of the electronics is about 40 MHz. Desire to keep corrections for accidentals and dead time below five percent frequently forced a reduction in beam at low momentum transfers. This limit corresponds to an average data rate of about three events per 1.6 microsecond long beam pulse.

Counts in almost all electronic units were scaled on Transistor Specialties, Inc. 100 MHz. scalars. At the end of each data run, the computer read these scalars. This was the only counting information of the experiment.

To simplify trouble-shooting, signals from all counters were split just before attenuation (the splitter has been suppressed on the electronics diagrams for simplicity). All signals and all triggers were brought, properly timed, to one panel. By plugging in cables, the experimenter could display the pulse height spectrum of any counter gated by any trigger.

During the first half of the experiment the electronics was considerably more complex. S9, S10, and S11 each had two discriminators, one biased to reject minimum ionizing particles, which was used for the proton logic, and the other set to count all particles going through the counter, used in the pion trigger. The hodoscope logic was also doubled so that coincidences on both pions and protons could be scaled simultaneously. The pion counts in the hodoscope were supposed to provide a sensitive index to each counter's performance. It was found that plotting proton rate against angle gave all the necessary diagnostic information. Eliminating the double accounting made the electronics simpler, faster and more easily modified.

8. The Computer

The SDS 9300 computer at SLAC has a 32K memory of 24 bit words, and is roughly equivalent to an IBM 7094 in performance. Its priority interrupt system allows it to break off in the middle of one task to execute a more urgent task immediately, with the priorities of up to 32 subprograms being assigned by the programmer. The system software allows an experimenter to program in FORTRAN in almost all applications.

At the beginning of a run beam monitors and scalers are zeroed, and the run number counter incremented. The computer then reads various multiplexers and a digital voltmeter to determine important experimental variables, such as the spectrometer angle and momentum, hodoscope angle, settings of the various slit openings and the target position. Warning messages will be issued if, for example, the experimenter has left a screen in the beam or if the momentum has changed more than .1 percent from the previous run.

During a run, the computer functions as several pulse height analysers. When an event occurs the fast electronics interrupts the computer and the computer reads six analog to digital converters, updating the appropriate histograms. The histograms (e. g., a counter's pulse height spectrum) can be displayed on an oscilloscope or the line printer. During a run, the computer can also perform on-line data analysis on runs already completed, as will be discussed shortly.

At the end of a run, the electronics and beam monitors are stopped. The computer then reads the scalers and the charges accumulated on the beam monitors. Diagnostic summaries, such as ratios of beam monitors, are printed. The data, besides being printed, are written on magnetic tape, which can then be used to do on-line analysis.

Some data analysis is usually done during the next run at a low priority level. The counting rates of any desired past run can be plotted against angle with the on-line Calcomp plotter. Most frequently, the run just completed is plotted so that physicists can see their data and look for possible trouble. At the same time data from any desired set of runs can be accumulated into a composite counting rate vs. angle array. Any run can be added to or deleted from the accumulation at any time. Plots and printouts of the accumulation can be made at any time so that eager physicists can calculate cross sections and search for steps. Besides plotting, the computer was programmed to print out data from any block of consecutive runs upon request. Without the computer's on-line data analysis it would have been almost impossible to keep up with the flow of data.

Nearly all the programs for this experiment were adaptations of programs for a previous experiment on backward pi-plus photo-production. A more detailed account of programming considerations for that experiment exists in the Ph. D. thesis of David B. Gustavson. (48)

9. Resolution

Angle resolution was dominated by the effects of proton multiple scattering. The magnitude of these effects was calculated with a Gaussian approximation to the theoretical form of Bethe. (49) These calculated numbers agree within errors to observed widths of the spectrum of recoil protons from elastic positron-proton scattering at t of $-.2$, $-.3$ and $-.4$ $(\text{GeV}/c)^2$.

Other causes of poor resolution were usually less important. The spread of energies in the initial electron beam varied, but was typically $\pm .5$ percent. The width of the bremsstrahlung endpoint region is about 25 MeV. The .75 inch width of the hodoscope counters limits the resolution in the p - θ plane (intrinsic spectrometer resolution is about one quarter of a counter width). Spreading of proton momentum can be caused both by differing flight paths out of the target and by the random uncertainty of the energy loss. The convenience of changing hodoscope angle only with t and not with endpoint energy or spectrometer angle costs some resolution. To compare these effects to that of multiple scattering, each source of error can be converted to an effective mass resolution by multiplying with the appropriate partial derivatives. The results at the rho mass and the phi mass for two energies and several momentum transfers are in table A-2.

TABLE A-2 CONTRIBUTIONS TO MASS UNCERTAINTY

T	ENDPOINT ENERGY	MULTIPLE SCATTERING	ELECTRON ENERGY	ENDPOINT SPREAD	COUNTER WIDTH	MOMENTUM SPREAD	HODO. ANGLE
AT RHO MASS							
.2	5 GEV	16 MEV	3 MEV	3 MEV	3 MEV	2 MEV	2 MEV
.5	5	11	4	4	5	2	0
.9	5	8	5	5	7	1	1
1.38	5	7	7	6	8	1	3
.2	15	50	3	1	10	9	1
.5	15	34	4	1	16	5	1
.9	15	27	5	2	21	4	2
1.38	15	23	7	2	26	3	4
AT PHI MASS							
.2	5	11	3	3	3	0	5
.5	5	8	4	4	4	1	3
.9	5	6	5	5	5	1	1
1.38	5	5	6	6	6	1	1
.2	15	37	3	1	7	5	4
.5	15	25	4	1	12	4	2
.9	15	20	5	2	16	3	3
1.38	15	17	6	2	19	2	5

The effect of assumed resolution on derived cross sections was investigated by varying the input multiple scattering angle to the fitting program. Derived cross sections remained well within errors for any reasonable assumed resolution.

It might be thought that some error is introduced because two different hodoscope elements in the same angle bin do not have identical average momenta. This was not a serious problem because the data were taken so that, upon consolidation, these effects cancelled to first order. Occasionally, however, the effect can be seen as discontinuities in the steep rise of the yield from rho production.

APPENDIX B

1. Data Consolidation

Data were taken in about 3000 five- to ten-minute runs. The fundamental quantities measured in each run were photon energy, spectrometer momentum and angle, total photon flux and the counts in each of the eight hodoscope counters. Before fitting could begin the data at each endpoint energy and t had to be organized into a yield curve. This section describes the organization process.

The spectrometer angle settings for each endpoint energy and t were programmed to obtain as many internal consistency checks as possible, since great demands are made of the beam monitors in detecting steps containing only a few percent of the total counting rate. For each t the hodoscope angle in the p - θ plane (calculated from kinematics) and the .75 inch width of the hodoscope counters determine the angular width subtended by a counter, typically 2.6 milliradian. The interesting range of spectrometer angles was divided into bins of this width. A normal data taking pattern called for the spectrometer to move six bins between runs, so that the two counters on one end of the hodoscope fell into the same angle bins as the two counters on the opposite end had occupied during the previous run. The entire angle range of interest was swept back and forth, offsetting the spectrometer angle a few bins at each reversal of direction, until the desired number of counts had been accumulated. In many sweeps each bin was sampled by each of the eight hodoscope counters.

The resulting data can be imagined as being in a matrix with indices of bin number and hodoscope counter number, as illustrated

in figure B-1. In this figure the eight columns numbered 1 through 8 correspond to the hodoscope elements, and bin number increases down the page. The elements of the matrix are the counts observed in the counter during a run divided by the number of equivalent quanta (in units of 10^{11}) for the run. The data from any one run slant diagonally, e. g., for run 6046 counter 1 is in bin -7, counter 2 in bin -6, etc. Before the data can be legitimately consolidated to counting rate vs. bin (the "ACCUM--ERROR" columns) several corrections must be made. These include adjusting the hodoscope counting rates for individual differences in detection efficiency, accounting for dead time and accidentals in the electronics in each run, verifying the performance of the beam monitor for each run, and correcting or discarding runs having procedural errors. These corrections will now be discussed in detail.

Obtaining relative hodoscope efficiencies is easy when a range of angle bins has been sampled by all eight counters e. g., bins 4 through 18 in figure B-1. For each counter one simply adds the rates over that range of bins and divides by the sum of the average rates for the same bins to obtain relative efficiency directly. When the data are more sparse, a smooth fit is made to the rates, and efficiencies obtained by comparing to the fit.

Because photon energy does not affect proton transport or counter performance, relative efficiency should be independent of endpoint energy. The stability of the derived efficiencies thus gives an index to their reliability. Table B-1 lists efficiencies at t of $-.7 \text{ (GeV/c)}^2$. (Average efficiencies were used in computing the rates shown in figure B-1. This is why the "computed efficiencies" are so nearly 1.) Relative efficiency ought to change with t for

FIGURE B-1 Data Matrix

MATRIX FOR E=11.5, I= .70, 23 RUNS IN SNEEP

BIN	RUN	1	2	3	4	5	6	7	8	MMASS	ACCUM--ERRR	CHIS	N	SATIP--ERRR	SD		
-7	6046	.2882	.0000	.0000	.0000	.0000	.0000	.0000	.0000	.915+8	.2282	.0093	.0	1	.9962	.0123	.3
-6	0	.0000	.2286	.0000	.0000	.0000	.0000	.0000	.0000	.883+9	.5286	.0093	.0	1	.0000	.0000	.0
-5	0	.0000	.0000	.2426	.0000	.0000	.0000	.0000	.0000	.842+8	.2426	.0093	.0	1	.0000	.0000	.0
-4	0	.0000	.0000	.0000	.2446	.0000	.0000	.0000	.0000	.816+4	.2446	.0086	.0	1	.0000	.0000	.0
-3	6045	.2427	.0000	.0000	.0000	.2648	.0000	.0000	.0000	.780+6	.2537	.0062	3	2	.9928	.0117	.6
-2	6044	.2604	.2529	.0000	.0000	.0000	.2617	.0000	.0000	.753+0	.2584	.0051	.6	3	.9982	.0114	.2
-1	6043	.2560	.2674	.2689	.0000	.0000	.0000	.2551	.0000	.703+6	.2618	.0044	2	0	.9984	.0112	.1
0	6042	.2667	.2677	.2829	.0000	.0000	.0000	.2551	.0000	.661+8	.2700	.0040	5	8	.9917	.0112	.8
1	6031	.2701	.2846	.2892	.2785	.2876	.0000	.0000	.0000	.617+3	.2821	.0041	2	8	.9996	.0105	.0
2	6026	.2873	.2806	.2858	.3037	.2885	.0000	.0000	.0000	.569+4	.2889	.0038	3	5	1.0081	.0100	.8
3	6041	.2997	.3006	.3073	.2940	.2971	.2953	.2874	.0000	.517+1	.2973	.0036	2	6	.9915	.0097	.9
4	6037	.3093	.3063	.3063	.3121	.3095	.3003	.3124	.2944	.459+0	.3092	.0034	6	5	1.0067	.0093	.7
5	6033	.3451	.3365	.3136	.3340	.3142	.3253	.3110	.392+5	.3110	.3270	.0035	11	7	1.0280	.0088	3
6	6028	.3382	.3536	.3397	.3470	.3450	.3469	.3306	.3352	.312+2	.3419	.0034	3	9	1.0013	.0085	.2
7	6040	.3848	.4015	.4183	.3994	.3930	.3988	.4050	.4122	.202+5	.4022	.0039	6	7	.9919	.0082	1
8	6036	.4708	.4621	.4678	.4781	.4517	.4862	.4830	.4607	.123+5	.4763	.0042	9	4	.9897	.0078	1
9	6030	.5081	.4962	.4960	.5189	.5311	.5086	.5016	.4978	.267+7	.5060	.0044	9	1	1.1147	.0074	2
10	6025	.5257	.5241	.5440	.5308	.5508	.5263	.5290	.5138	.357+6	.5318	.0045	5	7	1.0064	.0070	.9
11	6039	.5724	.5649	.5658	.5485	.5959	.5914	.6054	.5720	.429+0	.5767	.0047	15	5	.9981	.0066	.3
12	6035	.6093	.6020	.6424	.6271	.6308	.6184	.6538	.6320	.490+0	.6220	.0048	8	5	1.0012	.0061	.2
13	6032	.6589	.6513	.6482	.6853	.6740	.6840	.6662	.6676	.544+1	.6682	.0050	5	6	.9908	.0058	1
14	6027	.7405	.7176	.7618	.7176	.7460	.7404	.7307	.7439	.593+2	.7413	.0053	5	4	1.0097	.0054	1
15	6038	.8091	.8029	.8296	.8284	.8153	.8467	.8577	.8278	.538+5	.8285	.0056	11	5	1.0097	.0051	.5
16	6034	.9846	.9837	.9271	.9483	.9607	.9667	.9494	.10057	.680+7	.9588	.0060	15	4	1.0080	.0049	1
17	6029	1.1359	1.1497	1.1663	1.1923	1.1314	1.1552	1.1638	1.1629	.720+4	1.1572	.0066	7	4	.9976	.0047	.5
18	6024	1.3492	1.3544	1.4071	1.3848	1.4050	1.3567	1.4096	1.4280	.758+0	1.3893	.0072	12	4	.9887	.0046	2
19	0	.0000	1.6123	1.6123	1.6373	1.5958	1.5958	1.5765	1.6170	.793+7	1.6158	.0083	8	9	.0000	.0000	.0
20	0	.0000	1.6886	1.6886	1.7091	1.6969	1.7483	1.7528	1.7528	.827+9	1.7207	.0093	6	9	.0000	.0000	.0
21	0	.0000	.0000	.0000	1.7722	1.8336	1.7982	1.7867	1.8174	.860+6	1.8016	.0104	4	4	.0000	.0000	.0
22	0	.0000	.0000	.0000	.0000	1.8348	1.8703	1.9034	1.8699	.892+1	1.8496	.0118	4	5	.0000	.0000	.0
23	0	.0000	.0000	.0000	.0000	1.8846	1.9053	1.9053	1.8982	.922+5	1.9127	.0138	3	7	.0000	.0000	.0
24	0	.0000	.0000	.0000	.0000	.0000	.0000	1.9492	1.9770	.951+8	1.9631	.0172	7	2	.0000	.0000	.0
25	0	.0000	.0000	.0000	.0000	.0000	.0000	.0000	2.0763	.980+2	2.0763	.0250	0	1	.0000	.0000	.0

COMPLETED EFFICIENCIES
 .992+30 .995+37 1.000679 1.000591 1.000026 .999838 1.003155 .999842
 STANDARD DEVIATION OF RATIO * .00881 RMS NON-STATISTICAL DEVIATION * .00527

NCNTR	SUMCH12	NCN12	S/N
1	.000	5	1.000
2	3.868	2	1.934
3	4.267	2	2.133
4	6.423	2	3.122
5	13.022	3	4.341
6	10.414	2	5.207
7	11.493	2	5.746
8	13.477	15	8.985
SUP	18.4083	151	1.219

TABLE B-1 HODOSCOPE COUNTER EFFICIENCY AT $T = -.7$ (GEV/C)²

ENDPOINT ENERGY	HODOSCOPE COUNTER NUMBER							
	1	2	3	4	5	6	7	8
6.5 GEV	.978	.975	.990	.994	1.008	1.018	1.017	1.020
6.5	.965	.981	.991	1.001	1.010	1.018	1.025	1.009
9.0	.969	.962	.992	1.001	1.021	1.018	1.022	1.016
11.5	.965	.969	.992	.996	1.021	1.017	1.024	1.016
13.0	.975	.972	.990	.991	1.011	1.019	1.022	1.021
14.5	.984	.982	.994	.996	1.006	1.010	1.015	1.013
AVERAGE	.973	.974	.992	.996	1.013	1.017	1.021	1.016

several reasons: pulse heights vary with proton momentum, so discriminator thresholds have to be set for different t , and the error in the standard values will vary for different t ; timings have to be reset because proton flight time changes, and quantized delay values introduce varying errors; the location of one counter is not quite identical to that of a different counter in the same angle bin, and the error due to this varies with t . Thus it is necessary to have a set of relative hodoscope efficiencies for each t . These are listed in table B-2.

Accidental coincidences and dead time losses are both proportional to average instantaneous photon flux to first order. Thus for any reasonable data rate they should be proportional to one another, and accidental coincidences can be used to measure both. As described in appendix A, accidental rates are measured by deliberately mistiming input signals to certain coincidence units, the accidentals monitors. These monitors are calibrated by varying beam intensity.

The empirical correction formula used (for the latest data) was

$$\text{Correction factor} = 1 + a_B \cdot \frac{9 \cdot (10)}{9 \cdot 10 \cdot 11} + a_C \frac{9 \cdot 10 \cdot (C)}{9 \cdot 10 \cdot 11} - a_H \frac{4 \cdot (P)}{4 \cdot P} \quad (\text{B-1})$$

where

X.Y indicates the number of genuine coincidences between X and Y,

X.(Y) is the number of accidental coincidences between X and Y; Y is delayed,

9 represents counts in S9, the first trigger counter,

TABLE B-2 HODSCOPE COUNTER EFFICIENCIES VS. T

-T (GEV/C) ²	HODSCOPE COUNTER NUMBER							
	1	2	3	4	5	6	7	8
.12	.975	1.005	1.004	1.030	1.009	1.007	.991	.979
.2	.997	.996	1.007	1.010	1.008	.999	1.001	.982
.3	1.005	.989	.999	.997	1.000	1.002	1.007	1.001
.4	.982	.979	.992	.996	1.008	1.014	1.016	1.012
.5	.975	.978	.992	.997	1.013	1.017	1.019	1.008
.7	.973	.974	.992	.996	1.013	1.017	1.021	1.016
.9	.990	.973	.992	.994	1.007	1.014	1.019	1.011
1.1	.970	.967	.984	.992	1.016	1.023	1.027	1.021
1.38	.938	.952	.980	.980	1.022	1.042	1.052	1.033

10 represents counts in S10,

11 represents counts in S11,

C represents counts in the Cerenkov counter which vetoes pions,

P is the proton trigger $9.10.11.\bar{C}$,

4 represents counts in S4, one of the hodoscope counters,

and the a's are parameters to be evaluated experimentally. The justification for this formula is as follows. There will be no accidentals in the proton trigger because it is threefold. Thus the $9.(10)$ rate is proportional to dead time losses in the proton trigger. At high momentum transfer, when $9.10.C$ is used to veto pions from the proton trigger, accidental coincidences are an additional source of dead time. The $4.(P)$ rate is supposed to represent accidentals between the hodoscope counters and the proton trigger.

The coefficients a were determined by comparing counting rates at high and low photon fluxes. There were difficulties in the determination; some data were inconsistent, and the eventual fit did not work very well. The dead time estimate is therefore reliable only to about 25 percent. Fortunately the corrections themselves are only a few percent, so the error of the corrections does little harm. Values used in correcting the latest data were

$$a_B = 1,$$

$$a_C = 1.3 \text{ when the Cerenkov counter is used in veto,}$$

$$a_H = 0.8.$$

For the data taken without the Cerenkov counter veto ($-t$ less than $.5 \text{ (GeV/c)}^2$), the corrections were not significantly different from zero, and were therefore set to zero. This indicates that dead time and accidental rates approximately cancelled. At the two largest momentum transfers, counting statistics were so poor on 9.10. (C) and 4. (P) that the formula was modified to $a_B = 3.5$, $a_C = a_H = 0$.

For the early data, each run was corrected individually according to equation (B-1). In the latest data it was found that counting statistics on the accidentals monitors caused a perceptible degrading of the data, and an average correction as a function of angle was employed. Unusually steady beam conditions made this procedure feasible.

Several methods were used to test the SEQ's performance run by run. One is to compare the photon flux as measured by the SEQ to that measured by the two backup monitors. However, the SEQ is less sensitive to beam steering and structure than the others, so a disagreement is likely to be an error in the secondaries. A more reliable check is to divide the observed pion counts by the SEQ charge for each run, and plot the result as a function of angle. If a point deviates widely from a smooth curve, the corresponding run's SEQ reading is suspect, particularly if the backup monitors also disagree.

The redundancy of the data make possible a final test -- the smoothness of the proton counting rate itself. The sum of the eight hodoscope counter rates in a run (i.e., the sum along a diagonal in figure B-1) should equal the sum of the average rates for the corresponding bins. Thus the ratio of these numbers should be 1 within counting statistics if the SEQ behaves perfectly. In figure B-1 the ratio, its error and its deviation from 1 in sigma units is listed on

the same line as the run number in columns headed "RATIO", "ERROR", and "SD", respectively. The r. m. s. deviation of the ratios from 1 is a figure of merit for the SEQ's performance during data taking. If we assume that this deviation can be accounted for by adding in quadrature the error from counting statistics and a random error for the SEQ, the SEQ error needed is usually about .2 percent.

Monitor drifts and jumps were detected by plotting this ratio as a function of run number. A monitor drift shows up as a non-zero average slope. Individual bad runs have deviant ratios. Usually the pion rate and backup monitors also indicate trouble. In such a case the SEQ reading is modified to make the ratio 1, and a consistency check is performed. In each angle bin the χ^2 was computed under the expectation that the rate measured in each run was the same within statistics (the "CHISQ" column in figure B-1). For a corrected SEQ reading to be kept, the sum of these bin χ^2 's had to decrease significantly (the summed χ^2 , total degrees of freedom and the ratio of these numbers is at the very bottom of figure B-1). The major source of bad SEQ readings was unnoticed gross steering changes in midrun. About one third of the data sweeps required SEQ corrections in one or more runs. Only a handful of runs had to be discarded entirely.

2. Fitting Procedure

The basic operation of the fitting program has already been described in chapter IV. Here the background polynomial and the partial yield curves y in the fitting function of equation (IV-1)

$$Y(\theta) = \left[\frac{J}{\sin \theta} \right] [a_{\pi} y_{\pi} + a_{\eta} y_{\eta} + a_{\rho} y_{\rho} + \dots] \\ + b_0 + b_1 (\theta - \theta_0) + b_2 (m - 2m_{\pi})^2 + b_4 (m - 2m_{\pi})^4 + \dots \quad (\text{B-2})$$

will be described in detail. The special problems encountered in fitting for each particle's cross sections will also be discussed.

a) Background. The terms containing parameters b_0, b_1, \dots of equation (B-2) are elements of a polynomial intended to fit all sources of background. A polynomial is used simply because the yield of protons from background is expected to be a smooth function of angle. Justification for this approximation has been presented in chapter III, section C. Parameters b_0 and b_1 determine a straight line in angle, intended to describe the proton yield in the kinematically forbidden region. A second-, third- or fourth-order polynomial in mass squared, beginning at the threshold for production of two pions, represents proton yield from production of many-body final states. The order of the background polynomial was taken as low as possible consistent with a reasonable fit. Increasing the order of the polynomial tended to produce unrealistically shaped "backgrounds." The effect of imperfect resolution on the form of the background should be small everywhere except at the two-pion threshold, where some sharp change in background slope is possible. To account for this the most rapidly varying (b_2) term is modified to mimic the effects of proton multiple scattering.

b) Eta and Phi. Because the eta and phi theoretical yield curves were extremely simple, they will be described first. Both particles appear as sharp steps on a relatively large background, so the signal from photoproduction by photons with energy near the end-

point is all that must be described well by the fitting functions y_η and y_φ . It is simplest to assume the cross sections are independent of photon energy, and that the reduced bremsstrahlung spectrum factor $\alpha(k, E_0)$ is a constant for k less than E_0 . These approximations misrepresent the signal from production by low energy photons, but the errors are absorbed in the already phenomenologically fit background. With these approximations, $y_\eta(\theta)$ and $y_\varphi(\theta)$ are simple step functions, 0 below threshold and 1 above. Near the threshold angle, where the yield is changing rapidly, the shape of the experimental yield curve is determined by the resolution of the apparatus. The fitting program uses the known resolution to spread the step rise of y_η and y_φ appropriately.

The fitting program makes unreliable error assignments because it does not properly account for the correlations between background and step errors. Therefore, errors were estimated using such information as the sensitivity of derived cross sections to input parameters, and the estimation by eye of reasonable limits for the background function.

For particles whose steps are sharp, including the eta and phi, and also the pion, two other procedures were used to verify cross sections. One was to estimate step size by eye, demanding a smoothly varying background and taking into account the known resolution. In figures B-2 and B-3 sample steps for eta and phi respectively are shown to prove that fitting by eye is quite feasible. First difference curves help to locate the steps, estimate resolution and evaluate errors.

The second method exploits the symmetry of the step about its center. The difference in yield at angle bins equally distant but on opposite sides of the step is plotted against distance from the

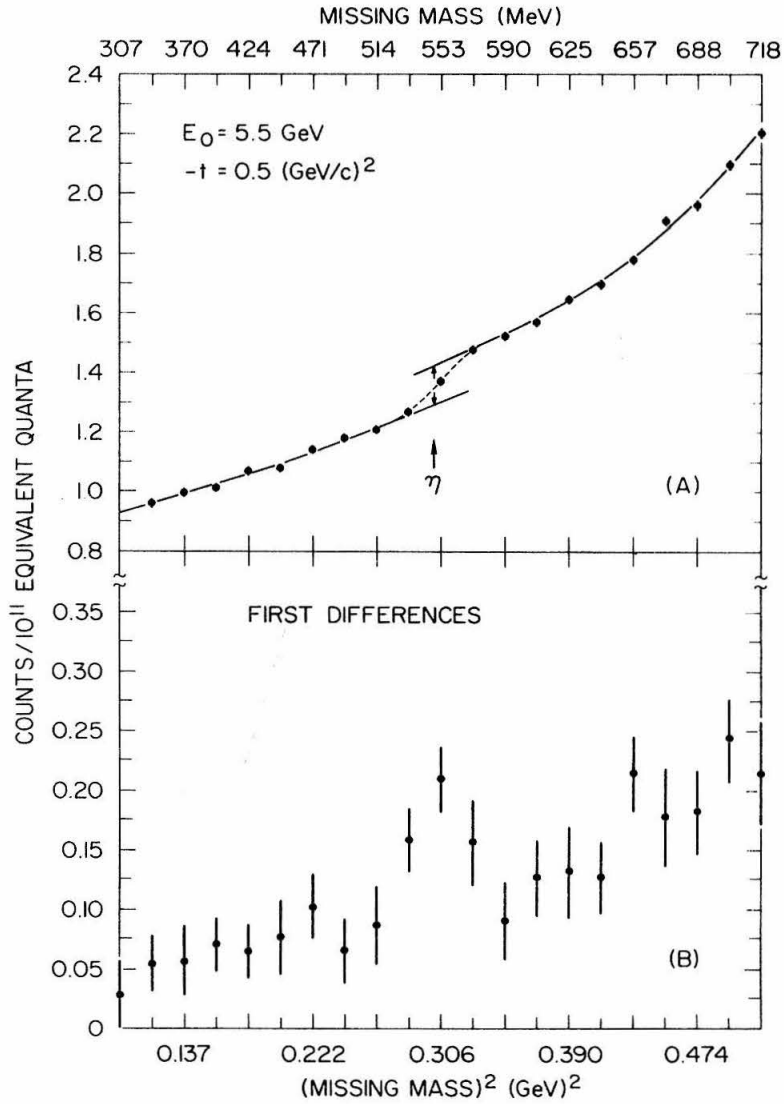


FIGURE B-2

Eta Step

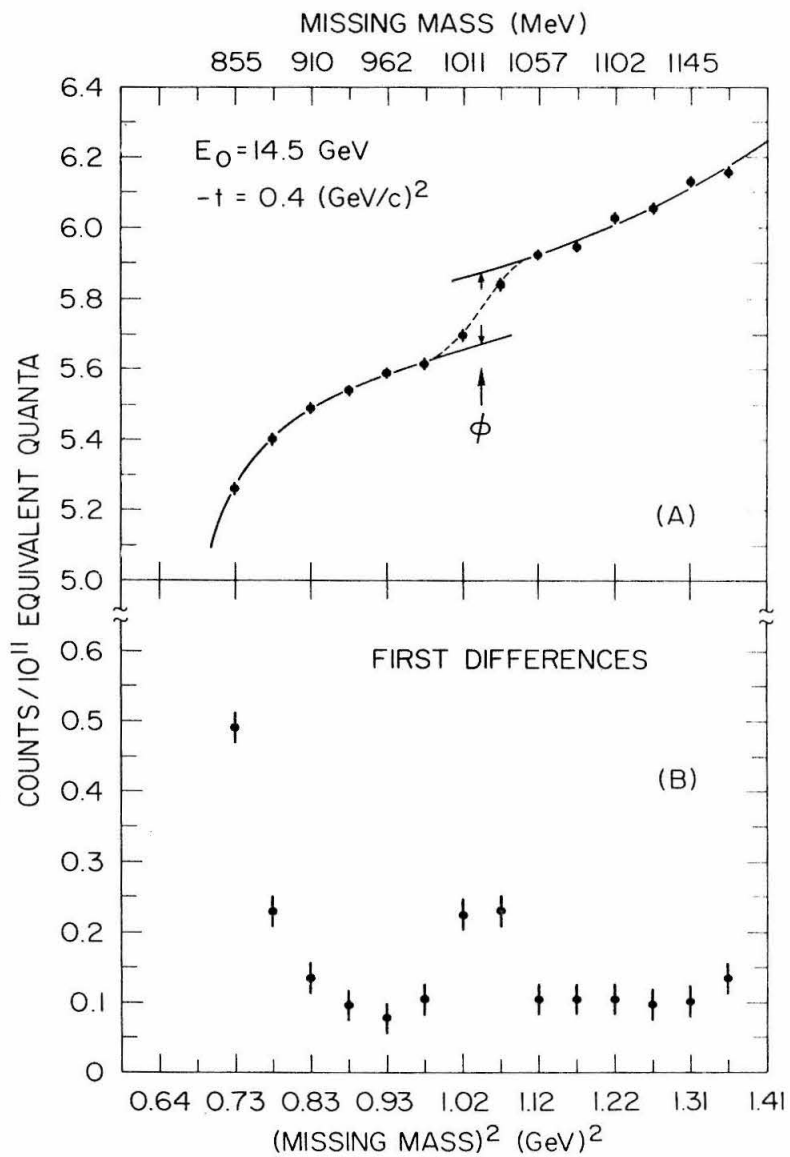


FIGURE B-3

Phi Step

step. If this yield difference is extrapolated to zero distance from the step, and resolution is properly accounted for, the result is the step size. This method has the advantage of giving a reasonable error estimate directly, as well as having a computer's objectivity.

The three methods of fitting sharp steps generally agreed within errors. Disagreements were found to be due to differing, but equally valid, assumptions about the behavior of the background. A compromise value was then chosen, and error estimates expanded to account for the interpretational ambiguity. Problems of this type were more frequent at low momentum transfer, where poor resolution makes steps less sharp so that the background estimate is more critical.

Background was the chief source of difficulty in extracting eta and phi cross sections. Eta production competes with two imperfectly known sources of background, multipion production and the low mass tail of the rho distribution. As energy increases, a kinematical compression of the variation of missing mass with angle aggravates the problem. This, coupled with the rapid decrease of eta cross sections with energy, made it impossible to obtain information above a photon energy of 11.5 GeV. For the phi, the major problem is separating the 3 percent step from the large rho-production background. In some cases interaction with the high mass end of the rho distribution also causes trouble.

c) Pion. Obtaining cross sections was more difficult for the pion than for the eta and phi because of three complications. The rapid variation of cross section with photon energy cannot be ignored. Rapid variation with angle of the photon energy effective in producing pions and poor angle resolution combine to cause confusion at low momentum transfers. Compton scattering cannot be resolved from

pion production, so corrections must be made. Each of these complications will now be discussed.

In preliminary analysis, the pion production cross section was assumed independent of photon energy, like the eta and phi. The cross sections obtained on this assumption showed strong dependence on photon energy. To obtain a better theoretical yield curve, the first round results were used to correct the energy dependence of the pion cross section. The theoretical yield function finally used was thus

$$\begin{aligned} y(\theta) &= 0 \text{ below threshold} \\ &= s^{2\alpha(t) - 2} \text{ above threshold,} \end{aligned}$$

where s is the square of the total center-of-mass energy, calculated from p , θ and the pion mass. $\alpha(t)$ is the effective Regge trajectory, a function evaluated from the first stage analysis. Because of this s -dependence $y_{\pi}(\theta)$ does not have a simple step shape, but rises continually with θ beyond threshold.

The photon energy effective in producing pions must be known in order to unfold the introduced s -dependence from the yield curve in obtaining a cross section, as well as to quote the measured cross section at the right energy. Unfortunately, this is not easily done. Effective photon energy varies rapidly with angle at low momentum transfer, as can be seen by differentiating equation (III-1) with respect to θ :

$$\frac{dk}{d\theta} = \frac{p k \sin \theta}{p \cos \theta - T} = \frac{p k E_0 \sin \theta}{|t| + m_{\pi}^2} . \quad (\text{B-3})$$

Notation is the same as in equation (III-1). For low momentum transfer the denominator is small, since the square of the pion mass is small. Confusion arises because of poor angle resolution, which also becomes worse at low momentum transfer. The combined effect can be large. As an extreme example, at an endpoint energy of 16 GeV and a t of $-.2 \text{ (GeV/c)}^2$, the range of energies lumped together within angle resolution, $\frac{dk}{d\theta} \Delta\theta$, is about 3 GeV. As can be seen from figure B-4, the step shape degenerates almost to the shape of a ramp. The data of figure B-4 were so equivocal that a reliable cross section could not be obtained. For some subtractions the problem is severe enough that no pion peak can be seen within statistics. For momentum transfers greater than $-t = .7 \text{ (GeV/c)}^2$ angle resolution is good, and the problem disappears.

A general rule is needed for deciding what photon energy to specify when quoting cross sections. This energy is taken to be the photon energy producing pions at an angle $\Delta\theta$ smaller than the threshold angle, where $\Delta\theta$ is the angle resolution. The rule is reasonable because a determination of step height is most sensitive to the region near the top of the step, where its curvature is greatest, and not very sensitive at all to the middle of the step, which corresponds to the endpoint energy.

The energy dependence assumed for the cross section is unfolded at the effective energy, and the cross section quoted at this energy. Since both the assumed yield curve shape and the unfolding procedure depend on the assumed behavior of the cross section with s , the derived cross section and effective energy are slightly model dependent. But, amusingly, the cross sections obtained this way generally agree within errors with the more naive preliminary ones.

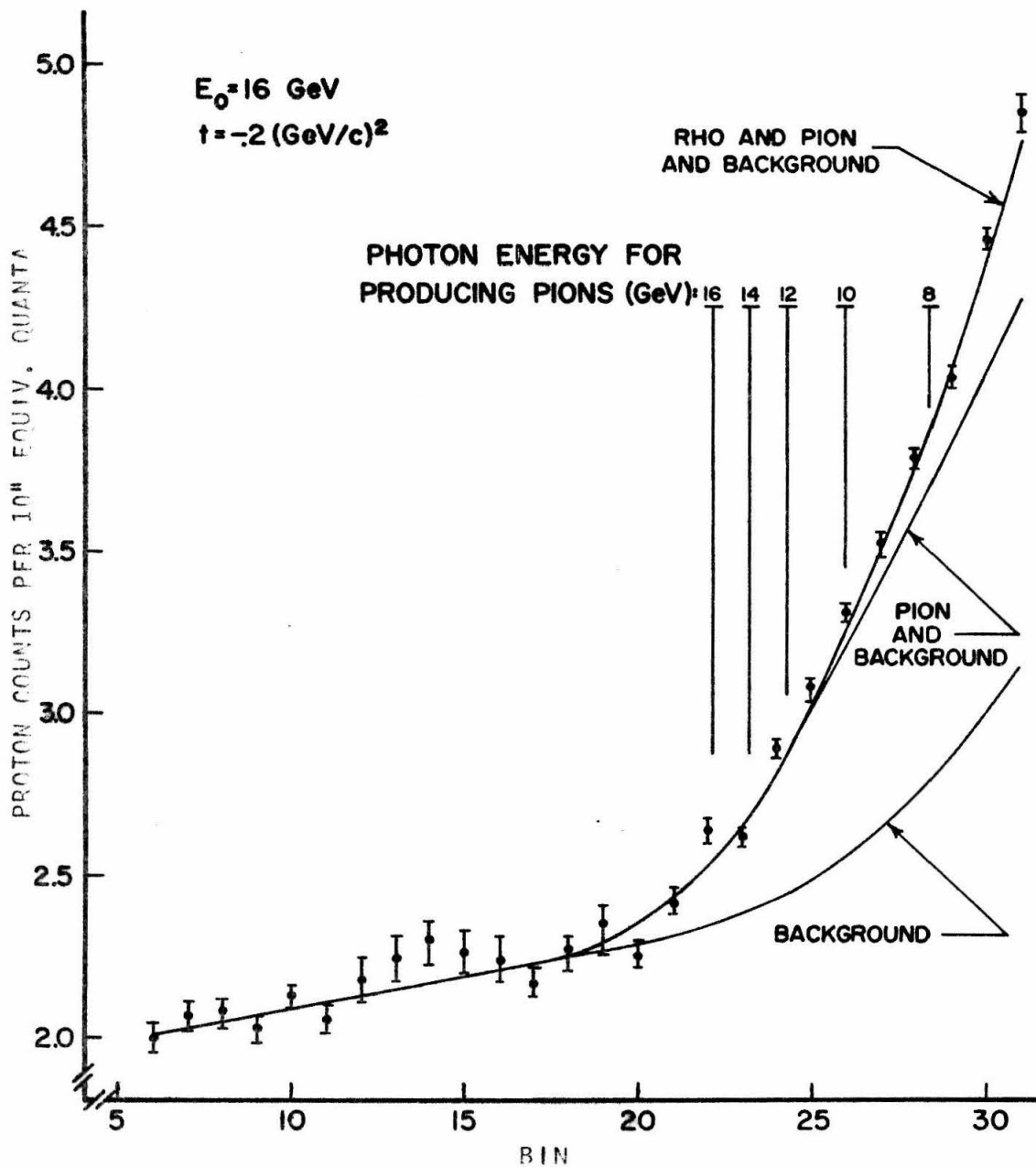


FIGURE B-4

Pion Step Showing Energy Resolution Problem

Because Compton scattering cannot be resolved from pion photoproduction this contribution must be subtracted off to obtain pion cross sections. An estimate has been made using the optical theorem applied to the measured total photon cross section⁽²⁴⁾ to obtain the differential cross section at zero momentum transfer and the vector dominance model applied to this experiment's rho production data to obtain t dependence.

Recent experiments measuring the total hadronic photon-proton cross section seem to agree on a value of $115 \mu\text{barn}$ ⁽²⁴⁾, roughly constant above 6 GeV photon energy. Applications of the optical theorem gives

$$\left. \frac{d\sigma}{dt} \right|_{t=0} (\text{Compton}) = .68 \mu\text{barn}/(\text{GeV}/c)^2 .$$

The vector dominance model suggests that Compton scattering cross sections should be similar in t dependence to rho photoproduction cross sections. Assuming a behavior of $\exp(8.5 t)$, the Compton cross section is taken to be

$$\frac{d\sigma}{dt} (\text{Compton}) = .68 \exp(8.5 t) \frac{\mu\text{barn}}{(\text{GeV}/c)^2} . \quad (\text{B-4})$$

This correction can be very large, up to 50 percent at low momentum transfers and high photon energies, but is negligible above $-t = .7 (\text{GeV}/c)^2$. The estimated error in determining the correction is 15 percent.

The large Compton corrections and the effective energy problem make low momentum transfer pion cross sections subject to possibly large systematic errors.

d) Rho. Determining the cross section of the broad rho resonance is very much more difficult than for the narrow particles. There are several interacting causes:

- i) The proper theoretical resonance shape is unknown.
- ii) The width and mass of the rho are not well known.
- iii) It is hard to distinguish omega from rho production.
- iv) The unknown background can vary greatly over the large rho width.

These interpretational difficulties contribute far more to uncertainty in the rho cross section than statistical fluctuations in the data. The attempts made to deal with each of them will now be described.

- i) Three representations of the rho shape are currently popular.

A relativistically correct generalization of the simple Breit-Wigner form is given by Jackson⁽²⁵⁾:

$$P(m) = \frac{2 m m_\rho}{\pi} \frac{\Gamma(m)}{(m^2 - m_\rho^2)^2 + m_\rho^2 \Gamma^2(m)} \quad (\text{B-5})$$

where

m is the invariant mass of the two pion system

$$\Gamma(m) = \Gamma_0 \left(\frac{q}{q_0} \right)^3 \frac{2}{1 + (q/q_0)^2} \quad \text{is the width}^{(50)}, \text{ which varies}$$

with m because of phase space,

$$\Gamma_0 = \Gamma(m_\rho) \quad \text{is the rho width, approximately 125 MeV,}$$

$q = \left(\frac{m}{2}\right)^2 - m_\pi^2$ is the momentum of each pion in the rho rest frame,

and q_0 is q evaluated at $m = m_\rho$.

Physical assumptions go into choosing the form of $\Gamma(m)$. Perturbation theory gives $\Gamma(m) = \frac{m_\rho}{m} \Gamma_0 \left(\frac{q}{q_0}\right)^3$ ⁽²⁵⁾. With this width

function, the integral over m of the function $P(m)$ is logarithmically divergent. This absurdity comes from the tacit assumption that the pion-pion final state interaction is independent of m . The form for $\Gamma(m)$ given in equation (B-5) is equivalent to an effective range approximation with range q_0^{-1} , approximately $(350 \text{ MeV})^{-1}$. Since this width function was originally proposed by Selleri ⁽⁵⁰⁾, equation (B-5) will be referred to as the "Jackson-Selleri" form. J. Pišút and M. Roos ⁽⁵¹⁾ discuss the width problem in detail and suggest several possible forms. A rho shape corresponding to their solution 24 gave results essentially the same as those from equation (B-5).

Ross and Stodolsky ⁽⁵²⁾, who consider photoproduction of rhos specifically, suggest multiplying the Jackson-Selleri form by

$\left(\frac{m}{m_\rho}\right)^4$. This additional factor is from the propagator for the virtual rho meson in the diffraction dissociation model, diagrammed in figure B-5a. There is some controversy over this factor, but at least one experiment ⁽⁵³⁾ indicates it may be necessary.

A third description of the rho shape is given by Söding ⁽⁵⁴⁾. He points out that the reaction $\gamma + p \rightarrow \pi^+ + \pi^- + p$ can proceed both by rho production (figure B-5b) and by a "Drell-type" mechanism

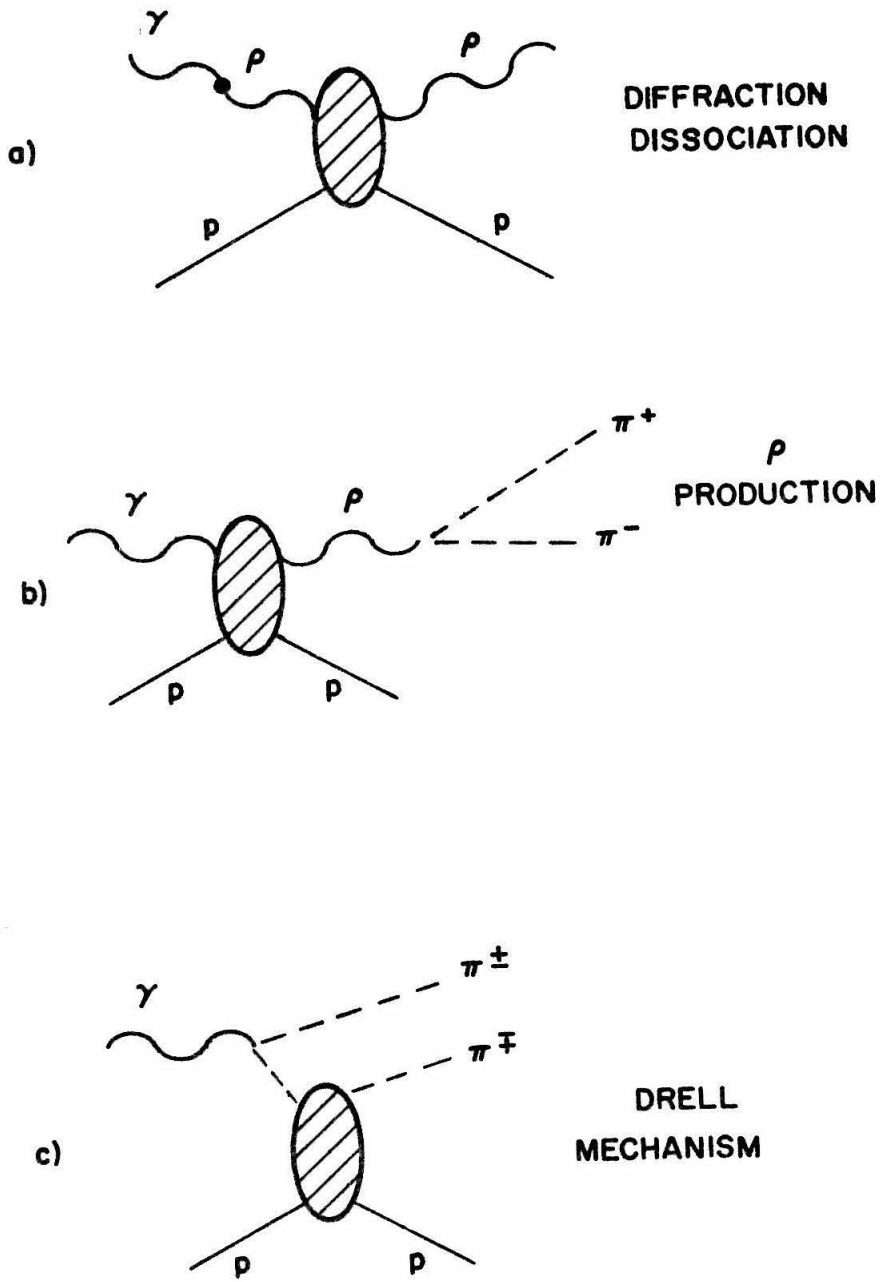


FIGURE B-5 Feynman Graphs

(figure B-5c), i. e., one pion exchange with the exchanged pion scattering elastically off the proton. These two amplitudes will interfere, affecting the observed rho meson shape.

Fits were made to the data assuming each of these shapes. To help further determine the sensitivity of the derived cross sections to the assumed shape, additional forms were used. These included a simple nonrelativistic Breit-Wigner and Ross-Stodolsky type factors with powers 1, 2 and 3 instead of 4. Each of the shapes was introduced into the fit as $P(m)$ in equation (III-3c). The rho cross section was assumed independent of photon energy in the fitting program. Cross sections obtained with different shapes could disagree if the fitting program chose differing divisions between rho signal and background. In general, cross sections obtained with different models disagreed by 5 to 10 percent. One source of this discrepancy was differing assumptions about what fraction of the rho cross section comes from masses above 1.3 GeV, the highest mass reached in most of the data. Cross sections obtained with the Jackson-Selleri form, which falls least rapidly at high masses, tended to be about 7 percent higher than the others'.

Because of poor angle resolution and unknown backgrounds, this experiment is not a sensitive test of rho meson shapes. Nevertheless, several general trends are observed and will be mentioned.

The Jackson-Selleri shape tended to underestimate the yield in the mass region 300 to 600 MeV at low momentum transfers and at low energies. This could mean either that the shape is wrong or that the background from multibody final state production rises too sharply for the assumed smooth background polynomial to reproduce it in this kinematic region. At high energies and high momentum transfers, the Jackson-Selleri form seemed to describe the data very well.

The Ross-Stodolsky form describes the rho shape better than the Jackson-Selleri form at low momentum transfers and low energies. However, at high momentum transfers and high energies the low mass region is over-enhanced, so that fits tend to be significantly poorer than with the Jackson-Selleri form. This discrepancy cannot easily be attributed to poor representation of the background, since the background would have to decrease to compensate the over-enhancement, which is not physically reasonable.

The Söding form is not significantly different from the Jackson-Selleri form at the momentum transfers of this experiment. A computer program calculated the rho shape, the Drell background and the interference term using the matrix elements given by Söding and doing the phase space integrals numerically. This program reproduced qualitatively the graphs of Söding's predictions at 4 GeV incident photon energy, when an additional numerical integration over t was performed. Calculations for the parameters of this experiment showed the Drell term was totally negligible and the interference term was at its largest less than 10 percent of the rho peak height. This smallness is presumably due to the rapid decrease of the propagator for the exchanged pion. Because of the size of the Söding correction terms, the only noticeable effect was a slight shift in mass. Therefore, no systematic attempt was made to fit the data with Söding's model.

The Jackson-Selleri shape was adopted as the standard for the quoted cross sections.

ii) Various experiments have found rho widths anywhere between 90 and 175 MeV, and masses between 730 and 780 MeV⁽⁵⁵⁾. Both these parameters were treated as unknowns to be determined, even though large backgrounds made the measurement unreliable.

Best values of the parameters were chosen by changing input values to the fitting program and observing the effect on fit quality.

The best fit mass value did not appear to vary regularly with s or t . It did depend on the shape chosen. The Jackson-Selleri form led to a mass of 765 ± 20 MeV; the Ross-Stodolsky form shifted this mass 10 to 20 MeV higher. The value 765 MeV agrees well with the world average^(51, 55). The rho mass shift reported in several earlier photoproduction experiments^(5, 6, 56) was not observed. Each yield curve was fit several times with differing assumed rho widths between 60 and 160 MeV. The best rho width value was determined by interpolating to a minimum of the fit χ^2 . The error in the determination was taken to correspond to where the probability for observing the χ^2 had fallen to half its best value. This criterion typically indicated errors of 30 MeV. Most determinations favored a width between 80 and 160 MeV. The 25 percent that did not give widths in this acceptable range were regarded as anomalies, either having an unusual collusion of statistical errors or a background whose freedom to imitate the rho was impossible to control. In general, the rho shape chosen had little effect on preferred width. There was also no apparent regular dependence of width on s or t . With this as justification, a width of 127 ± 25 MeV was obtained by averaging the well-determined widths. This value agrees well with the average of the world's data^(51, 55). All final cross section fitting used a 125 MeV wide Jackson-Selleri rho shape with mass 765 MeV.

The derived rho cross section varies strongly with assumed rho width, typically 5 percent per 10 MeV change in width. Since the width is determined only within 25 MeV, this is a major source of error. The problem arises because the background polynomial can

vary to accommodate changes in rho width. The dependence of derived cross section on assumed width is thus a manifestation and a measure of our ignorance about the background. For each yield curve, the sensitivity of cross section to width was used to help estimate the error in the cross section.

iii) The omega meson, of mass 783 MeV and width 12 MeV, cannot be separated cleanly from the rho with the mass resolution of this experiment. Attempts were made to separate the two with the fitting program, but the results are extremely sensitive to poorly known rho parameters. In a typical case the omega to rho ratio changed from 1:5 to 1:15 when the assumed rho width changed from 150 to 100 MeV.

Therefore, a fixed omega to rho ratio of 1:9 was assumed following the prediction of SU_3 symmetry⁽¹⁸⁾ for diffraction photoproduction of vector mesons. Other experiments have verified both that omega photoproduction is largely diffractive and that the omega to rho ratio is nearly 1:9^(5, 17). The assumption is also consistent with the general trend of results from the separations attempted on our data. The theoretical curve fitted to rho plus omega production is therefore 90 percent Jackson-Selleri rho and 10 percent omega. The stated rho cross section is 90 percent of the fitted combined cross section. This procedure can introduce errors on the order of 5 percent, both by distorting the theoretical fitting function and by attributing rho production to omega or vice versa.

iv) The background polynomial was kept to as few terms as was consistent with a reasonable fit. This procedure was necessary because if more terms were used the background polynomial usually interacted with the rho shape and took on an unrealistic form. For example, if the rho fitting function were centered at the wrong mass,

the background might acquire an s-shape to shift the effective rho position. The effect was also visible when fitting for the rho width: frequently the background was flexible enough that good fits were achieved over a large range of widths.

This criterion for the background function, which amounts to demanding smoothness, does not have a clear physical justification. It is completely possible, for example, that nonresonant two- or three-pion production rises rapidly at threshold. On the other hand, attempting to estimate each of the many individual sources of background would lead to more parameters in the fit, and again the freedom of the background would mask the interesting physics.

The error due to uncertainty in the background was estimated by comparing fits with different input parameters and by visually selecting reasonable upper and lower limits to the background. The variation of background with assumed rho width also proved useful. Background uncertainty was the dominant source of error in the rho cross section determination, frequently exceeding 10 percent of the cross section.

Each of the four problems in fitting the rho is made less tractable by the presence of uncertainties from the other three. Thus despite the high statistical precision obtained in this experiment, the rho cross section can only be determined within about 20 percent.

3. Corrections

The corrections applied to the cross sections will be calculated here. They have already been tabulated in table 2, chapter IV.

a) Pair production by beam photons. If a photon is converted to an electron-positron pair downstream of the last sweeping magnet, the pair will usually travel with the beam and stop in the SEQ. The SEQ, which measures total beam energy using secondary emission from the charged particles of a shower, responds to the pair the same way it would have to the original photon. However, the pair does not behave the same way as a photon in the target. The electron-proton scattering cross section is smaller; also, the original photon's energy is divided between the electron and the positron with a broad energy distribution, so smooth backgrounds but not steps are generated. Thus pairs count in the beam monitor as photons, but do not contribute to measured cross sections.

Photons can pair produce in material upstream of the target (.013 radiation lengths) and in the hydrogen of the target upstream of the average location for a visible event. If the spectrometer is properly aligned on the center of the target, an average of 6 inches of hydrogen is upstream of the event. Thus 3.2 percent of the beam is lost to pair production.

b) Energy loss from ionization both reduces the observed momentum of the recoil proton and, because ionization rate is a strong function of momentum, affects the spread of momenta observed. A bunch of particles with momenta between $p_0(1 - \delta)$ and $p_0(1 + \delta)$ at the target center will have a wider percentage spread of momenta after traversing the target hydrogen. This can be seen as follows.

The spectrometer is set to observe protons which originate at the center of the target with momentum p_0 . Momenta will be measured relative to p_0 : $p = p_0 + \delta p_0$. Both δp_0 and the momentum loss are assumed small compared to p_0 , so that a power

series expansion can be used. To first order, the momentum loss per unit distance travelled is

$$\frac{dp}{dx} = -\lambda(p) \approx -\lambda_0 + \lambda' \delta p_0 \quad (\text{B-6})$$

where $\lambda_0 = \lambda(p_0)$ and $\lambda' = -\frac{d\lambda}{dp}$ is greater than zero, i. e., increasing p decreases the rate of momentum loss. We take as ansatz

$$p(x) = p_0 + a\delta + bx + c\delta x,$$

where x is the thickness of material traversed. Inserting this into equation (B-6) and requiring that $p(0)$ be $p_0(1 + \delta)$, we find

$$p(x) = p_0(1 + \delta) - \lambda_0 x + \lambda' \delta x p_0 = p(0) - \lambda_0 x + \lambda' \delta x p_0.$$

Thus a particle with a momentum deviating from the central momentum by δp_0 at the center of the target will, after traversing material, have a momentum deviation

$$\begin{aligned} \delta' &= \frac{p(x) - (p_0 - \lambda_0 x)}{p_0 - \lambda_0 x} = \delta \left(\frac{p_0(1 + \lambda' x)}{p_0 - \lambda_0 x} \right) \\ &\approx \delta(1 + \lambda' x + \lambda_0 x/p_0) > \delta. \end{aligned} \quad (\text{B-7})$$

Since the momentum spread at the spectrometer δ' is greater than δ , the fixed fractional momentum aperture of the spectrometer projects back to a smaller effective momentum aperture at the target.

The magnitude of this effect varies with p_0 because λ_0 and λ' are strong functions of p_0 . Calculated corrections have been listed in table 2.

c) The loss of proton signal from nuclear interactions was estimated with a combination of calculation and experiment. It would be desirable to calculate an expected loss and verify it experimentally, but this is not possible because an unknown fraction of interacting protons still triggers the proton logic.

The following procedure was used. Knowing the amount and chemical composition of the material between the event and the last counter, the interaction rate was calculated using experimental pp and n-Carbon scattering cross sections.⁽⁵⁷⁾ To be able to count, a proton was required to survive unscattered to halfway through the last counter used in the proton logic. Interactions occurring in front of the first counter S9 were taken to be 100 percent effective in absorbing protons, but interactions in the counters had an absorption efficiency to be determined experimentally.

The experimental measurements were made with the spectrometer set to two different angles, one where protons outnumbered pions by about four to one, and the other where the fluxes were about equal. The full proton and pion logic was used to solve for the ratio of the fluxes at both angles. With this information the proton and pion triggering efficiencies for counters beyond S10 could be obtained. Protons counted by S9 and S10, but not by S11 were assumed to have been absorbed in the Cerenkov counter, or S11. At $t = -.3 (\text{GeV}/c)^2$, 75 percent of protons suffering nuclear interactions were actually lost. For $t = -.4 (\text{GeV}/c)^2$ the corresponding killing efficiency was 60 percent. On this basis it was assumed that for $-t$ less than or

equal to $.3 (\text{GeV}/c)^2$, 75 percent of proton interactions in the counters led to absorption, for $t = -.4 (\text{GeV}/c)^2$, 60 percent, and for $-t$ greater than or equal to $.5 (\text{GeV}/c)^2$, 50 percent.

The absorption loss estimates are listed in table 2. The estimated error in their determination is ± 25 percent.

d) Counter efficiencies of all large trigger counters (S9, S10, S11, S12, and S13) were assumed to be 100 percent. The absolute efficiency of the hodoscope was estimated by comparing the counting rate summed over the eight hodoscope counters to the rate expected from the ratio of the hodoscope area to trigger counter area. The efficiency was found to be 95 ± 2 percent for all momentum transfers but the smallest, where it was 97 ± 2 percent. The relative efficiencies of the hodoscope counters were determined with much greater accuracy using redundant data, as described in section 1 of this appendix.

e) As described in appendix A, the Lucite Cerenkov counter counted a few of the protons traversing it. The resulting loss of good events is compensated as indicated in table 2.

REFERENCES

1. M. Braunschweig et al., Phys. Lett. 26B, 405 (1968).
2. G. C. Bolon et al., Phys. Rev. Lett. 18, 926 (1967).
3. M. P. Locher and H. Rollnik, Phys. Lett. 22, 696 (1966).
4. J. P. Ader, H. Capdeville, and Ph. Salin, Nucl. Phys. B3, 407 (1967).
5. Aachen-Berlin-Bonn-Hamburg-Heidelberg-München Collaboration, Phys. Rev. 175, 1669 (1968), and DESY preprint 69/19, (June 1969) (to be submitted to Physical Review). These are summary articles. References to twelve previous publications of preliminary data are given.
6. The Cambridge Bubble Chamber Group has published several articles on photoproduction at incident energies up to 6 GeV. These include Phys. Rev. 146, 994 (1966) (ρ); Phys. Rev. 155, 1468 (1967) (ω); Phys. Rev. 155, 1477 (1967) (π , multipion, strange particles); Phys. Rev. 156, 1426 (1967) (strange particles, including ϕ); Phys. Rev. 163, 1510 (1967) (nucleon isobars); and Phys. Rev. 169, 1081 (1968) (multipion, including η).
7. D. Bellenger et al., Phys. Rev. Lett. 21, 1205 (1968).
8. A. Dar and F. Weisskopf, Phys. Rev. Lett. 20, 726 (1968).
9. P. DiVecchia and F. Drago Phys. Lett. 24B, 405 (1967).
10. F. M. Pipkin, 1967 SLAC Symposium (Proceedings of the 1967 International Symposium on Electron and Photon Interactions at High Energies, Stanford Linear Accelerator Center, 1967).

11. E. Lohrmann, 1967 SLAC Symposium (cf. reference 10).
12. S. C. C. Ting, Proceedings of the XIV International Conference on High Energy Physics, Vienna, 1968.
13. G. McClellan et al., Phys. Rev. Lett. 22, 374 (1969).
14. M. Davier et al., Phys. Rev. Lett. 21, 841 (1968).
15. Reference 10 summarizes the VDM and has an extensive bibliography.
16. B. Margolis, Nuclear Phys. B6, 687 (1968).
17. M. Davier et al., Phys. Lett. 28B, 619 (1969).
18. H. Harari, 1967 SLAC Symposium (cf. reference 10).
19. R. J. Oakes and J. J. Sakuri, Phys. Rev. Lett. 19, 1266 (1967).
20. A. V. Tollestrup et al., SLAC Experiment E-39.
21. R. L. Anderson et al., SLAC proposal E-21c, 1968.
22. R. E. Diebold, Ph.D. thesis, California Institute of Technology, 1963 (unpublished).
23. R. Gomez and D. Sterba, private communications.
24. J. Ballam et al., Phys. Rev. Lett. 21, 1541 (1968) and SLAC preprint SLAC-PUB-618 (July 1969); D. O. Caldwell et al., Bull. Am. Phys. Soc. 14, 518 (Washington APS meeting April 1969); E. D. Bloom et al., Bull. Am. Phys. Soc. 14, 518 (Washington APS meeting, April 1969).
25. J. D. Jackson, Nuovo Cimento 34, 1644 (1964).
26. H. Harari, Phys. Rev. Lett. 21, 835 (1968).

27. D. Bellenger et al., Phys. Rev. Letts. 23, 540 (1969).
28. J. Frøyland, Nucl. Phys. B11, 204 (1969).
29. A. Capella and J. Tran Thanh Van, Nuovo Cimento Letters 1, 321 (1969).
30. M. L. Blackman, G. Kramer, and K. Schilling, preprint from Argonne National Lab. and Caltech (1969).
31. A. Dar, V. F. Weisskopf, C. E. Levinson, and H. J. Lipkin, Phys. Rev. Letts. 20, 1261 (1968).
32. B. Gorczyca and M. Hayashi, preprint from Institute of Physics, Jagellonian University, Crakow, Poland (1969).
33. F. Henyey, et al., Phys. Rev. Letts. 21, 946 (1968).
34. F. Henyey, et al., Phys. Rev. Letts. 21, 1782 (1968).
35. K. J. Foley et al., Phys. Rev. Letts. 11, 425 (1963) ($\pi\pi$ elastic scattering); Phys. Rev. Letts. 11, 503 (1963) ($\bar{p}p$ and Kp); Phys. Rev. Letts. 15, 45 (1965) (pp , πp , $\bar{p}p$, and Kp). Total cross sections are taken from Galbraith et al., Phys. Rev. B138, 913 (1965).
36. W. Rarita et al., Phys. Rev. 165, 1615 (1968).
37. F. Bulos et al., Phys. Rev. Letts. 22, 490 (1969).
38. G. McClellan et al., Phys. Rev. Letts. 22, 377 (1969).
39. For example, see J. A. Shapiro Phys. Rev. 179, 1345 (1969).

40. R. B. Neal, ed., The Stanford Two-Mile Accelerator, W. A. Benjamin, Inc., N. Y., 1968; SLAC User's Handbook.
41. R. L. Anderson and D. Porat, Nucl. Instr. and Methods 70, 77 (1969).
42. F. Wolverton, "Manual for BPAKI, Thick Target Radiator Bremsstrahlung Computer Program," Caltech (unpublished).
43. R. A. Early, SLAC Technical Note SLAC-TN-66-15, (1966, unpublished), and addendum Aug. 1968.
44. R. L. Anderson, Nucl. Instr. and Methods 65, 195 (1968).
45. G. Fischer and Y. Murata, SLAC preprint SLAC-PUB-605 (May 1969) (to be submitted to Nucl. Instr. and Methods).
46. R. L. Anderson, Nucl. Instr. and Methods 70, 87 (1969).
47. R. L. Anderson et al., Nucl. Instr. and Methods 66, 328 (1968).
48. D. B. Gustavson, Ph.D. thesis, Stanford University, Dec. 1968.
49. H. Bethe, Phys. Rev. 89, 1256 (1953).
50. F. Selleri, Phys. Lets. 3, 76 (1962).
51. J. Pišút and M. Roos, Nucl. Phys. B6, 325 (1968).
52. M. Ross and L. Stodolsky, Phys. Rev. 149, 1172 (1966).
53. J. G. Asbury et al., Phys. Rev. Lets. 20, 227 (1968).
54. P. Söding, Phys. Lets. 19, 702 (1965).
55. Particle Data Group, Rev. Mod. Phys. 41, 109 (1969) and exhaustive bibliography therein.

56. Lanzerotti et al., Phys. Rev. Letts. 15, 210 (1965).
57. MacGregor et al., Ann. Rev. Nucl. Sci. 10, 317 (1960); H. deCarvalho, Phys. Rev. 96, 406 (1954); V. A. Nedzel, Phys. Rev. 94, 175 (1954).